university of groningen / faculty of science and engineering

Kapteyn Astronomical Institute
Master Thesis

The Obelisk dust model: Using Rascas to analyze dust during the Epoch of Reionization

Author:
Pelle van de Bor

Supervisors:
Prof. dr. Pratika Dayal
Dr. Valentin Mauerhofer

July 12th, 2023

Abstract

Recent high-redshift detections of dust with ALMA and JWST have provided questions on the amount of dust in the early Universe. Dust may influence reionization by absorbing ionizing photons, but this effect is difficult to measure. To study the effect of dust on spectral properties, mock spectra are generated from the Obelisk simulation, which introduced a unique system of tracing dust for cosmological simulations. This system follows dust creation and destruction on a subgrid level, decoupling dust from gas. This thesis focuses on comparing this new model to existing models of dust attenuation (SMC, LMC, and BARE-GR-S).

I generated mock spectra of a sample of 554 halos in the Obelisk simulation using the Rascas code at $z = 6$. This is done for an angle-averaged view and 12 viewing directions for each halo.

From the spectra, the UV continuum slopes are found to be in line with literature values. The 2175 Å absorption feature is present in the Obelisk dust model. Using a Drude profile to model this feature, it is found that this does not influence the continuum slope measurement. The equivalent width of this feature is found to be correlated with the dust attenuation at 1500 Å.

To study the influence of dust on reionization, ionizing escape fractions are calculated. Using the directional spectra, it is shown that most of the ionizing radiation leaks from single directions with high escape fractions. The predicted escape fraction using the Obelisk model is compared to dual-screen model. This model underpredicts the values found by Obelisk, and therefore may only be used as a lower bound.

Predictions of the IRX-β_{UV} for the considered dust models are found to be higher than those found in literature. The data predict a cutoff at steeper β_{UV} of this relation compared to literature and finds that the steepness of the relation matches literature more closely. However, it is possible that the simulation overpredicts the dust attenuation, while observations have systematic errors when measuring the IRX.

I also study the wavelength dependence of energy absorbed by dust in the UV and optical. It is found that absorption of optical photons with wavelengths between 4000-10000 Å can provide $\sim 10\%$ of the total absorbed energy by dust in Obelisk. This fraction is correlated with the UV continuum slope, metallicity, and age. The contribution of the optical range is stronger in more evolved galaxies. Contribution of ionizing radiation to the total absorbed energy is comparatively low.

Contents

Chapter 1

Introduction

In recent years, with the introduction of HST and JWST, it has become possible to look further back in time, to the earliest galaxies (e.g. Beckwith et al., 2006, Postman et al., 2012, Oesch et al., 2016, Lotz et al., 2017, Finkelstein et al., 2023, Bunker et al., 2023, Harikane et al., 2023). Especially JWST has allowed for deeper study into the galaxy population at $z = 6 - 18$ (e.g. Naidu et al., 2022b, Atek et al., 2023, Harikane et al., 2023, Bouwens et al., 2023), which caused a strong debate on whether these observations are reconcilable with the standard ΛCDM cosmological model (e.g. Haslbauer et al., 2022, Keller et al., 2023, McCaffrey et al., 2023, Boylan-Kolchin, 2023). Observations at redshifts above $z \sim 12$ are still often debated, with high-redshift samples turning out to be contaminated with low-redshift interlopers (e.g. Naidu et al., 2022a, Adams et al., 2023). These high-redshift observations have provided a new look into one of the phase transitions of the Universe, the Epoch of Reionization (EoR), which is believed to last between $\sim 15 < z < 6$ (e.g. Planck Collaboration et al., 2020a). There are still many open questions about this era. This thesis will, at $z = 6$ at the end of reionization, study an important parameter for this transition, the ionizing escape fraction. The UV continuum slope and infrared emission of these galaxies will also be studied. In this introduction, I will provide an overview of cosmic evolution from the Big Bang to the Epoch of Reionization, until arrival at $z = 6$.

Shortly after the Big Bang, the Universe was filled with fundamental particles such as quarks and electrons. As the Universe expanded, it cooled down and the first atomic nuclei of primarily hydrogen and helium were formed in primordial nucleosynthesis (Cyburt et al., 2016). The temperature was too extreme to allow for the capture of electrons around these nuclei, and because these particles are charged, matter and radiation were coupled. With further expansion, further cooling took place and a major transition in the Universe took place. Free electrons were able to be captured by primordial nuclei, creating the first atoms. This meant that matter and radiation were no longer coupled, which led to this primordial radiation streaming away to form the Cosmic Microwave Background (CMB) around 380.000 years after the Big Bang (Wise,

2019). The timeline of these events is shown in Figure 1.1. The baryonic content of the Universe at this time consists of neutral hydrogen and helium, with trace amounts of lithium, marking the beginning of the Cosmic Dark Ages (Cyburt et al., 2016, Wise, 2019). However, observations of the local Universe find that the hydrogen and helium are near fully ionized at current times ($\Omega_{\rm HI} \leq 10^{-3}$; Chen et al., 2021, Amiri et al., 2023, Xi et al., 2021). This implies that at some point in the evolution of the Universe, the intergalactic medium (IGM) went through a phase transition of reionization. With the dominance of matter after the decoupling of matter and radiation, gravity took hold and started forming structures through gravitational collapse (Wise, 2019). The neutral gas followed the dark matter halos beginning to form, and the first stars were created. These early stars emit new radiation that is capable of ionizing the neutral gas. This marks the end of the Cosmic Dark Ages and the beginning of the Epoch of Reionization (Dayal & Ferrara, 2018).

The standard cosmological model consists of dark energy (Λ), cold dark matter (CDM), and baryonic matter. This ΛCDM cosmology has been widely tested by observations by experiments such as COBE, WMAP, and Planck (e.g. Dwek et al., 1998, Hinshaw et al., 2013, Planck Collaboration et al., 2020a). The model has been successful at predicting the baryonic acoustic oscillations signatures (Planck Collaboration et al., 2020a) and temperature anisotropies of the cosmic microwave background (Planck Collaboration et al., 2020b). However, this model does face several challenges on the small scale, including the "missing satellite problem" where ΛCDM underpredicts the amount of satellite galaxies found around the Milky Way (e.g. Kauffmann and White, 1993, Bullock, 2010), and the "core-cusp problem" where the model predicts the cores of dark matter halos to be denser than those found through observations (Salucci, 2001, de Blok, 2010). See Perivolaropoulos and Skara, 2022 for a review of the challenges facing ΛCDM. These challenges have spawned many alternatives to ΛCDM. For a review of these alternatives, see Bull et al., 2016.

ΛCDM predicts the formation of dark matter halos through gravitational collapse from perturbations in the density field after the Big Bang (Taylor, 2011). Baryonic matter streams alongside the dark matter into the halos. When this matter, in the form of gas, has cooled down, it forms giant molecular clouds. These molecular clouds collapse and form the first stars. These stars are extremely metal-poor, in accordance with the primordial abundances of the gas that formed them. These Population III (Pop. III) stars, named so due to their low metallicity, are the first stars to be born. This process is thought to start in small halos ($M_h \simeq 10^6 M_\odot$) between $z \sim 20 - 30$ (Dayal & Ferrara, 2018). However, these stars may still form at later redshifts, since the inhomogeneous distribution of metals may allow for areas of pristine gas to exist at later times (Liu and Bromm, 2020, Katz et al., 2022b). The initial mass function (IMF) of Pop. III stars is still under debate (Chantavat et al., 2023, Prole et al., 2023,

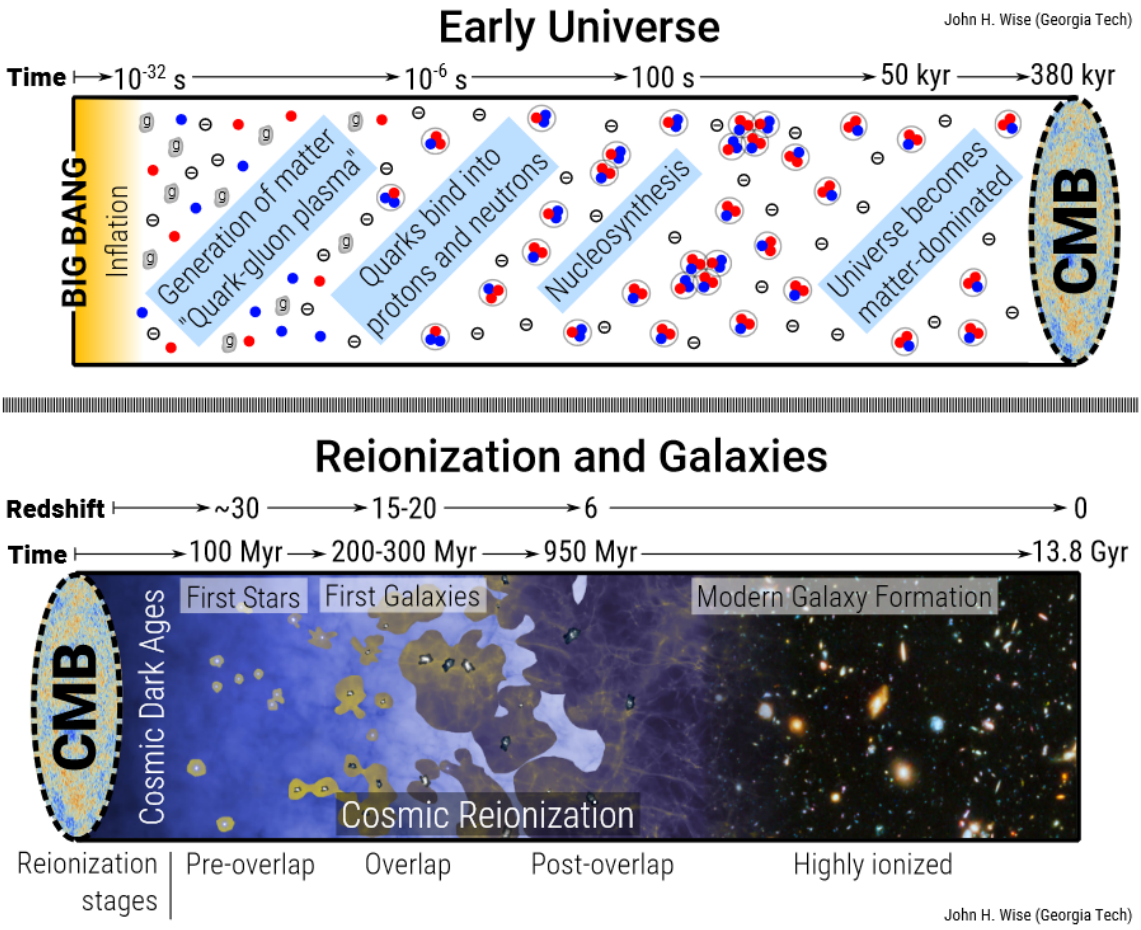

Figure 1.1: An overview of cosmic history from the Big Bang to the formation of the CMB (top) and from the CMB to the modern day (bottom). This shows the major phases that the Universe underwent, from an ionized state in the very early Universe, undergoing recoupling to form the CMB and becoming neutral, to becoming reionized by galaxies. Image reproduced from Wise, 2019.

Stacy et al., 2016), with their characteristic mass being uncertain. The IMF of Pop. III stars is predicted to skew to massive stars, which are short-lived, making observations of Pop. III stars hard to come by. However, recent observations with JWST have provided potential signatures for these stars at $z = 10.6$ (Maiolino et al., 2023), with JWST being able to provide more observations in the future (Trussler et al., 2022).

As Pop. III stars produce supernovas (SNs), they inhomogeneously enrich their environment with newly formed metals. This allows for more metal-rich Pop. II stars to form. Pop. II stars are believed to be the main metal producers in the early Universe (Dayal & Ferrara, 2018). These stars form faster than Pop. III stars, since the metals present in their molecular clouds allows for faster cooling mechanisms (Bromm & Loeb, 2003).

Both Pop. III and Pop. II stars produce hydrogen-ionizing radiation. Since the IGM during the cosmic dark ages consists mostly of neutral hydrogen, this radiation produces ionized regions around the sources of this radiation (Strömgren, 1939, Meiksin and Madau, 1993, Shapiro and Giroux, 1987). A different source of ionizing radiation is radiation originating from active galactic nuclei (AGNs). These are formed by supermassive black holes, whose accretion disks emit strong ionizing radiation. Which of the two sources for ionizing radiation is the dominant driver of reionization is under debate (Madau and Haardt, 2015, Trebitsch et al., 2021). The ionizing radiation produced by either source may get absorbed by the interstellar medium (ISM) of the galaxy, or escape into the circumgalactic medium (CGM) and IGM. As ionizing photons escape from galaxies, they form bubbles of heated ionized hydrogen (HII) around them, also called Strömgren regions or HII regions (Strömgren, 1939, Meiksin and Madau, 1993, Shapiro and Giroux, 1987). This higher temperature causes higher pressure, allowing these bubbles to expand. As they do so, the expanding bubbles collide with cold neutral hydrogen in the IGM. This gas gets heaped up in front of the expanding region, creating a shock in density, which drives gas out of the system. But as the region expands, its pressure drops. As long as the amount of ionizing photons remains constant, the Strömgren region will reach an equilibrium with the neutral hydrogen (Strömgren, 1939, Wise, 2019). The evolution of this region over time t in an expanding universe is given by (Meiksin and Madau, 1993, Shapiro and Giroux, 1987, Dayal and Ferrara, 2018)

$$4\pi r_I^2 n_H \left(\frac{\mathrm{d}r_I}{\mathrm{d}t} - H r_I \right) = \dot{N}_s - \frac{4}{3}\pi r_I^3 n_H^2 C(z) \alpha_B(T) \tag{1.1}$$

where $\dot{N}_s$ is the ionizing photon emission rate, r_I is the proper radius of the ionized region, n_H is the hydrogen number density, H is the Hubble constant, $C(z)$ is the clumping factor, and $\alpha_B(T)$ is the recombination rate. n_H is not uniformly distributed around a galaxy, changing the expansion rate in different directions, which makes the ionized region deviate from a sphere (Eilers et al., 2017, Chardin et al., 2017). Galaxies at this time therefore have complex ionized regions around them. As stars keep emitting

ionizing radiation, these regions expand outwards. When growing, they will encounter other ionized regions created by different galaxies, and the regions begin to overlap. This marks the transition from the pre-overlap to the overlap phase of reionization (Wise, 2019, see also Figure 1.1). During this phase, UV radiation from external sources can provide feedback. This UV background radiation heats the ISM, suppressing star formation, especially in small halos (Dayal & Ferrara, 2018). Multiple galaxies can then contribute to the growth of the ionized regions, creating complex geometries. But as these bubbles keep growing and overlapping more with others, they reach the post-overlap phase, in which the majority of the ionized regions will combine to fill the majority of the space with ionized hydrogen (Wise, 2019, see Figure 1.1). Small clumps of neutral hydrogen may still exist around this time or later, as can be seen in Lyman forest measurements (Bolton et al., 2022, Keating et al., 2020). The Epoch of Reionization ends when the last major clumps of neutral hydrogen get ionized, at which point the Universe has completed its phase transition.
One crucial factor in understanding the topology and speed of reionization is the escape fraction of ionizing photons $f_{\rm esc}$. This quantity determines the speed and topology of reionization (Dayal & Ferrara, 2018), while the absorbed energy by the ISM (which scales $\propto 1-f_{\rm esc}$) may be re-emitted as nebular lines (Dayal & Ferrara, 2018). Measuring the escape fraction observationally has proven difficult during the EoR. At low redshift, direct observations of $f_{\rm esc}$ do exist (e.g. Rutkowski et al., 2017, Choi et al., 2020, Flury et al., 2022a), but a direct measurement of the escape fraction for high redshift galaxies is nearly impossible. During the EoR a significant portion of the IGM consists of neutral hydrogen, making the IGM an excellent absorber of ionizing photons that have already escaped their galaxy of origin (Dijkstra, 2014). Lyman continuum (LyC) fluxes from galaxies at $z > 4$ are therefore extremely low, and nearly impossible to detect. This makes direct observation of the escape fraction difficult. Using simulation techniques to find the escape fraction is also subject to challenges. $f_{\rm esc}$ depends heavily on the small-scale environment of the ISM, which is hard to model accurately (Dayal & Ferrara, 2018). This method results in a large scatter in the measurements, ranging over several orders of magnitude (Ma et al., 2020, Rosdahl et al., 2022, Barrow et al., 2020, Yeh et al., 2023). The exact value of $f_{\rm esc}$ for a single galaxy is hard to predict both using observations and computational techniques, and is one of the major open questions remaining in the field.

A different open question is on the UV luminosity of early galaxies. From measurements of the UV luminosity of early galaxies, the UV luminosity function (LF) can be reconstructed. This function evolves over redshift. Assuming a Schechter fit (Schechter, 1976), the faint end slope and bright cutoff. There appears to be little evolution of the bright end between $z \sim 4-13$ (Harikane et al., 2022, Finkelstein et al., 2022), with no consensus being reached on the origin of this (e.g. Ono et al., 2018, Pacucci et al., 2022, Ferrara et al., 2023). The faint end is influenced by degenerate processes such as SN and UV background feedback, dust attenuation, and sampling biases due to these galaxies being more difficult to detect (Dayal & Ferrara, 2018). The cutoff mass below which star formation becomes inefficient and the slope of the UV LF at the faint end

are therefore still open questions.
Another primary concern is the dust content in these early galaxies. Dust masses as seen in the early Universe are higher than expected from current synthesis models (Dayal et al., 2022, Leśniewska and Michałowski, 2019, Michałowski, 2015, Reuter et al., 2020, Bouwens et al., 2022). This may indicate alternate pathways of dust growth, or an inherent difference between early galaxies and the models used so far. Particularly the ISM grain growth is uncertain, as this appears to be higher than expected (Ferrara et al., 2016). Dust growth in the ISM is coupled to metallicity, which in the early Universe is very low, so it is expected to be relatively slow (Triani et al., 2020). It is also dependent on temperature, which is also a topic of heavy debate in the early Universe, with measured values having a high scatter (Sommovigo et al., 2020, Sommovigo et al., 2022, Harikane et al., 2020, Bakx et al., 2020). This is due to the fact that with little data, there is a degeneracy present between the dust mass and temperature (Dayal et al., 2022). This makes it hard to determine the dust properties of the early Universe. Dust is often not at the forefront of large-scale hydrodynamical simulations, since its creation and destruction involve many factors, increasing simulation times. Large volume simulations such as MillenniumTNG (Kannan et al., 2022), IllustrisTNG (Marinacci et al., 2018, Shen et al., 2020), Horizon-AGN (Dubois et al., 2014), and EAGLE (Crain et al., 2015, Trayford et al., 2017) do not model the creation and destruction of dust, instead adding dust in post-processing based on the metallicity and gas density. This makes the study of the geometric distribution of dust relatively unexplored in these large simulation suites. In this thesis, I will look at the Obelisk (Trebitsch et al., 2021) simulation, which is a zoom-in simulation of Horizon-AGN, and includes a more detailed model for dust.

1.1 Observational evidence of the Epoch of Reionization

Observations on the Epoch of Reionization are done in several ways. The Lyman forest and Gunn-Peterson trough of high-redshift objects can tell us about properties along the line of sight. Cosmological measurements of the Thompson scattering can probe the density of free electrons, and thereby try to reconstruct the reionization history. Finally, 21 cm cosmology can observe the neutral hydrogen fraction through absorption measurements.

The distribution of neutral hydrogen regions along a single line of sight can be determined through the Lyman α (Lyα) forest present in a spectrum. This spectral feature requires a high-redshift source, typically from quasars (QSOs). Photons, after being emitted from a QSO, get redshifted as they travel through the Universe, and can encounter regions of neutral hydrogen. Every encounter creates an absorption line at the Lyα rest-frame frequency of 1216 Å. These lines get redshifted, such that higher

energy photons fall into the 1216 Å region, to be absorbed by the next neutral hydrogen region, creating another absorption line. This process repeats for every HI region in the line of sight, creating the Lyman α forest. The properties of each line can be used to probe the properties of the neutral hydrogen regions, as well as their redshift. At redshifts higher than $z \sim 6$, the Lyman α forest disappears, instead finding a Gunn-Peterson trough (Gunn and Peterson, 1965, first observed at high redshift by Becker et al., 2001 and further by e.g. Bañados et al., 2018). This spectral feature is related to the Lyman α forest, as the cause is the same. When HI regions have a high column density, this increases the optical depth and therefore broadens the line in the Lyα forest (Dijkstra, 2014). The Gunn-Peterson trough is the natural extension of this, being a near-total absorption of flux at wavelengths shorter than Lyα. At neutral hydrogen fractions higher than $\sim 10^{-3}$ a Gunn-Peterson trough is formed (Becker et al., 2001). The presence of the Gunn-Peterson trough, therefore, is an indication that the entire Universe has a neutral hydrogen fraction higher than this density. Since this feature is only present at redshifts higher than $z \sim 6$, this provides an observational constraint on the full reionization of the Universe.

Another technique using the Lyman α line depends on a class of galaxies in the early Universe that are Lyman α emitters (Stark et al., 2010). These galaxies emit more Lyman α radiation than most. By measuring the fraction of observed galaxies that belong to this class as a function of redshift, the missing amount of observed Lyman α emitters compared to a predicted model population is a measure of Lyman α absorption, and therefore of the ionization state of the IGM. Many forms exist for how this fraction evolves (Schenker et al., 2014), as the parameter space between the ionization state, escape fraction, and dust distribution is found to be degenerate (Hutter et al., 2014).

As reionization takes place, electrons are freed from their nuclei, which creates a population of free electrons (Wise, 2019). CMB photons can scatter off these electrons, since they introduce a Thompson scattering optical depth. This optical depth can be found through measurement of the damping of the anisotropy of the CMB at scales $10 < \ell < 30$ (Planck Collaboration et al., 2020a). This is done by mapping the polarization at these scales. This optical depth can be related to the column density of free electrons, meaning that it is a probe of reionization. The full history cannot be modelled using this probe only, but with constraints due to other observations, Planck Collaboration et al., 2020a find that the midpoint of reionization where half the Universe is ionized is given by $z_{re} = 7.68 \pm 0.79$. The full history can only be recovered by assuming a model for the reionization history. Overall, the Planck data suggest a late and fast reionization history, which is caused primarily by massive stars from small galaxies.

Finally, another way to observe reionization is through 21-cm observation. Neutral hydrogen emits a 21-cm line thanks to a transition between hyperfine levels of the ground state. During reionization, the IGM was still full of HI, and therefore provided a 21-cm background. The brightness temperature of this background compared to the CMB can provide information about the speed of absorption and emission of the 21-cm

line, and therefore on the fraction of neutral hydrogen. This has been investigated by Bowman et al., 2018 using EDGES, who found that the amplitude of the changes in the brightness temperature is bigger than initially expected, indicating additional coupling or other physics present in the very early Universe. However, their findings are strongly debated, with Singh et al., 2022 rejecting this at 95% confidence. Future experiments aiming to study this effect, such as SKA, are necessary for constraining this further.

In chapter §2 I will describe relevant theory of dust absorption, and describe the Obelisk simulation and the Rascas code used to generate mock spectra. Chapter §3 contains results found by this research, describing the galaxy sample and the properties derived from there.

Chapter 2

Theory

2.1 Hydrodynamical simulations

In this section I will provide a brief overview of the use of hydrodynamical simulations, as well as going into detail about the Obelisk simulation. Cosmological hydrodynamical simulations are one of many tools to study the Universe. These offer some of the most detailed views on large-scale structure in the Universe, as well as the evolution of the Universe over time. They track the evolution of baryonic and dark matter over time, by including gravity, hydrodynamics, star formation, and feedback. Using hydrodynamical codes, galaxy evolution can be studied in detail. They are used to supplement observational surveys, provide views of the Universe unconstrained by observational biases, and create estimations for future observations. The use of these simulations is therefore widespread. The number of codes capable of creating these simulations reflect this variety.

Roughly, these codes can in general be split up into two categories: Smoothed Particle Hydrodynamics (SPH), and Adaptive Mesh Refinement (AMR). SPH and AMR codes differ in that SPH codes set up tracer particles and have them interact as a fluid, while AMR codes act upon a gridlike mesh. SPH can use interpolation methods to generate a mesh. These differences in approach lead to differing implementations of gravity and hydrodynamics, but the general setup of the simulation process is the same. To start, a cosmology is chosen, and initial conditions at extremely high redshift (often $z > 100$) are created. From these initial descriptions, a gravity solver is used. These are typically particle-based, both for SPH and AMR codes. The dark matter and gas are propagated through time to create the seeds of cosmic structure. In AMR codes, the mesh on which these particles interact is refined locally, typically using a density-based criterion for the selection of refinement scales. The exact details of the physics, and the physical processes taken into account, are unique to each code, but generally, as the gas cools down and collapses, the process of star formation begins. This is represented by taking mass away from gas cells or particles and creating new stellar particles. Similarly, black hole formation also acts as a sink. As time evolution progresses, these star particles feed back into the gas through supernovae. As such,

the hydrodynamical and astrophysical properties are modelled, creating a completed simulation. What physics are highlighted is up to the users of these codes, as well as what solver is best. In the end, these are very computationally intensive methods of research. This requires running simulations on supercomputer clusters. But these simulations give a highly accurate view of the evolution of the Universe, depending on the resolution and physical models included in the simulation. These results may be directly compared to observations.

2.1.1 Obelisk

The Obelisk simulation was originally created to study the sources of reionization, that being AGN and star-forming galaxies, and to analyze which is more significant (Trebitsch et al., 2021). The Obelisk simulation is a zoom-in simulation of the larger Horizon-AGN (Dubois et al., 2014) simulation, centered around the most massive halo in this simulation. My visualization using the `yt` code (Turk et al., 2011) of four halos in the Obelisk simulation at $z = 6$ is shown in Figure 2.1. I will briefly go over the main relevant points of the Obelisk simulation, as laid out by Trebitsch et al., 2021.

The high-definition region created around the central halo is resimulated from the original initial conditions, with a much-decreased resolution outside of the high-definition region to stay consistent with Horizon-AGN. This allows the minimal cell size in the high-definition region to go down to $\Delta x \approx 35$ pc, compared to $\Delta x = 1$ kpc for Horizon-AGN. The Obelisk simulation was run using the AMR radiation-hydrodynamical code Ramses-RT (Rosdahl et al., 2013, Rosdahl and Teyssier, 2015). This improves over Horizon-AGN, which uses the RAMSES code (Teyssier, 2002), lacking radiation effects. But since one of the big aims of Obelisk is to study reionization, these effects need to be taken into account. The Ramses-RT code uses physical phenomena such as gravity, thermodynamics, hydrodynamics, and radiative transfer to simulate the baryonic content of the selected volume. The introduction of the radiative transfer physics is computationally intensive, since these processes require a small time interval to produce accurate results. No particle speeds near the speed of light. This makes the crossing time for light incredibly small compared to any other modelled quantity, which means that radiative transfer would require many time steps to produce accurate results. To combat this, Obelisk uses a variable speed of light approach, which decreases the number of time steps required significantly. Obelisk tracks ionization levels of hydrogen and helium, by following photon fields consisting of photons capable of ionizing these elements.

Other hydrodynamic processes taken into account in Obelisk are star formation, supernova shocks, and stellar feedback. The simulation also includes an advanced black hole model, featuring black hole formation, growth through accretion, AGN feedback, and radiation according to an AGN SED. Details of these processes are further explained by Trebitsch et al., 2021.

Dust in Obelisk is tracked using a unique model for cosmological simulations.

Most simulations present a constant value for the dust mass to gas mass ratio (e.g. Dubois et al., 2014, Trayford et al., 2017, Shen et al., 2020), typically ranging from $D/Z = 0.3 - 0.4$. Obelisk however creates a subgrid model for dust, separately from metals in gas. This means in practice that the dust mass to gas mass ratio is a scalar field over the whole simulation. It is assumed that dust is all of one single population, and does not drift relative to the gas, i.e. perfect coupling. The single population is modelled as having the same grain size and density. The amount of dust present in a cell does change over time. The creation and destruction of dust by supernovae are taken into account, as well as sputtering effects and growth by accretion of gas. Details of these processes as implemented in Obelisk are discussed in section 2.2. An important point is that dust is not coupled to the radiative hydrodynamics directly, as this would significantly increase computational cost. This means that dust is passive in Obelisk, which implies that metals collected into dust grains do not contribute to dust cooling, but metallic cooling instead. To add to this, the dust is only used for post-processing, to gather galaxy properties when the simulation has concluded.

In this thesis, only the snapshot at $z = 6$ will be taken into account. This is done to capture the state of the Universe directly after reionization took place. With galaxy candidates being confirmed at further and further redshifts (e.g. Schaerer et al., 2020, Dayal et al., 2022, Bunker et al., 2023, Harikane et al., 2023) the gaps in our knowledge about these galaxies have only become clearer.

2.2 Interstellar Dust

Dust in the early Universe is currently not fully understood. Recent observations of galaxies in the EoR find higher dust masses than expected with current models (e.g. Dayal et al., 2022, Michałowski, 2015, Reuter et al., 2020). This prompts research into the properties of dust, and reconsider the models currently used to study the dust contents of these high redshift galaxies. Therefore, I will briefly outline the main properties of dust, and then go into detail on the models used for dust absorption in this thesis and their implementation.

Dust grains come in many forms. One of the most important differences is the inherent composition of dust grains. There are many possible elements that can make up interstellar dust, however, the two most important kinds of dust grains are silicate and carbonaceous grains (Draine, 2003). Silicate grains predominantly consist of pyroxene and olivine minerals, which contain a characteristic silicate anion group of $[SiO_3]$ or $[SiO_4]$ respectively. These silicate groups are bonded to metal cations, most commonly magnesium or iron. This forms mineral structures, able to grow into amorphous or crystalline shapes, with amorphous shapes being the common variant ($\sim 95\%$) (Draine, 2003). Carbonaceous grains primarily consist of carbon. These grains come in many forms, since carbon can create bonds in several ways. Amorphous grains have little structure, but grains with more structure such as graphite are also present. Important is that carbon can capture hydrogen, so carbonaceous grains tend to be hydrogenized

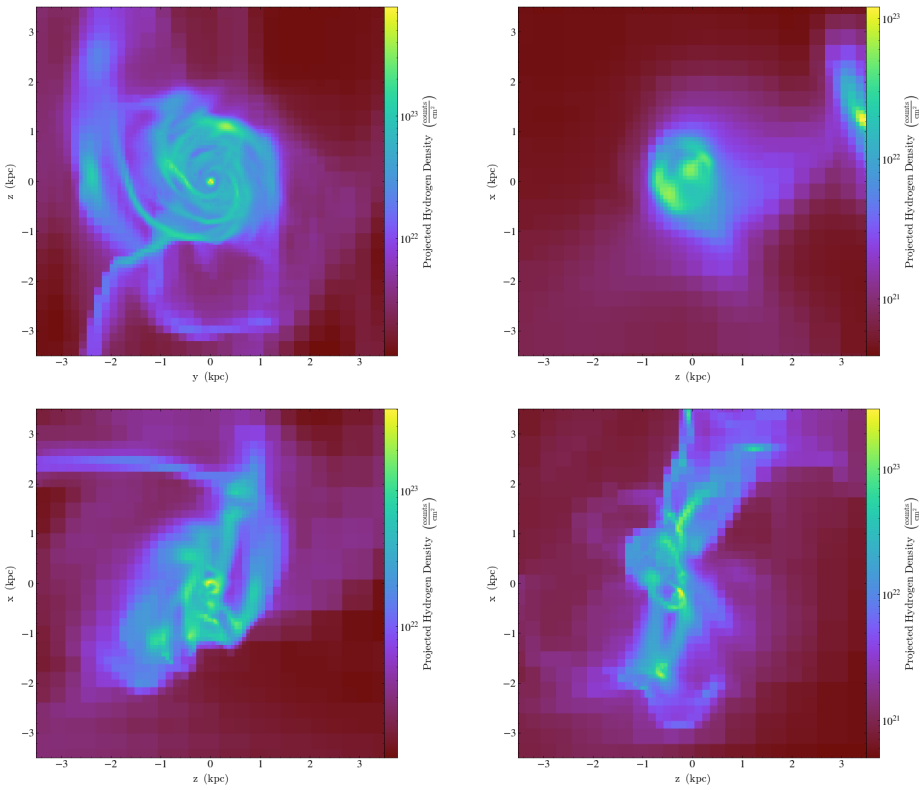

Figure 2.1: Projected hydrogen number density maps for 4 selected halos in OBELISK. These images correspond to the 4 test halos used in §2.3.2.

too. This allows for other stretching modes not present in pure carbon grains. Polyaromatic hydrocarbons (PAHs) are another important source of carbonaceous dust grains. These grains consist of graphite-like sheets of carbon creating many aromatic rings of carbon in their molecular structure. The sheets are hydrogenated, meaning hydrogen is present around their edges. When observing the dust attenuation curves in the local Universe, a bump in the spectrum around 2175 Å is visible for some sources such as the Large Magellanic Cloud and the Milky Way (Weingartner & Draine, 2001). The aromatic features of PAHs are the cause of the 2175 Å bump, due to excitation of the electrons that make up the bonds in these features. The presence of this feature, therefore, indicates the presence of PAHs in the interstellar dust.

The mixture between dust grains and interstellar gas varies in space due to effects that both create and destroy dust. This both changes the dust grain distribution as the amount of dust present. There are three avenues for dust creation in the early Universe (Dayal & Ferrara, 2018). Dust can be created in core-collapse supernovae. In these violent explosions the metallic contents of a stellar nucleus are ejected into the ISM. The expanding sphere cools down rapidly, and condensation of the first dust

grains can occur. The new dust grains act as nucleation sites for further dust growth, as more are created while the supernova remnant cools. The yields of this method of dust production are still uncertain, as observational evidence is hard to come by due to the transient nature of these events. Also, the shocks created by the supernova can destroy the freshly formed dust grains, decreasing the yield. Secondly, asymptotic giant branch (AGB) stars form dust too. These large stars lose their outer layers as they transition towards white dwarfs. This shedding spreads metals into the surrounding ISM, which then condense into dust grains as well. The composition of these dust grains highly depends on the specific metallicities of the parent star, with iron-rich dust being prevalent for all stars. Finally, there is dust growth through accretion in the cold gas phase. Here, already existing dust grains gain mass by accreting metals in the cold ISM. This is most efficient in cold but dense regions.

The destruction of dust can also be done in several ways. Star formation acts as a sink for dust particles. This is of course dependent on the star formation rate in the galaxy, as well as the quantity of dust present in the stellar clouds used to form new stars. Supernova shocks also destroy interstellar dust in addition to the dust it forms itself. Dust in the region around the supernova is impacted by shocks, which destroy the grains through sputtering and collisions. Thermal sputtering itself acts as an eroding force as well.

Lastly, the dust content of a galaxy can change due to inflows and outflows from and to the surrounding CGM and IGM. All these effects are summed up in Equation 2.1 (Dayal & Ferrara, 2018).

$$\frac{\mathrm{d}M_d}{\mathrm{d}t} = \dot{Y}_d + \dot{G}_{ac} + \dot{I}_d - \mathcal{D}_{ISM}\psi(t) - \dot{D}_{SN} - \dot{O}_d \tag{2.1}$$

Here, $\dot{Y}_d$ represents the dust yield both by supernovae and by AGB stars. $\dot{G}_{ac}$ is the dust growth by accretion. The dust capture by star formation is given by $\mathcal{D}_{ISM}\psi(t)$, with $\psi(t)$ being the star formation rate and $\mathcal{D}_{ISM}$ is the dust fraction of the ISM. $\dot{D}_{SN}$ models the destruction by supernovae, and finally, $\dot{I}_d$ and $\dot{O}_d$ represent the inflow and outflow of dust towards the galaxy.

2.2.1 Dust Attenuation Models

To estimate the amount of light scattered and absorbed by dust, a certain model of dust attenuation is assumed. There are several such models, being calibrated on different sources. It is common to look at the properties of a target to select the suitable model, such as the metallicity and age of the galaxy population that one wishes to study. For this thesis, a core component is to see the influence of dust on observational parameters, and to test the Obelisk dust model included in the simulation against commonly used models. Therefore, I will describe a few commonly used dust models and their implementation into the Rascas code (Michel-Dansac et al., 2020) for this thesis.

To calculate the optical depth due to dust, there are 2 possible methods. This depends on whether one measures dust number density, or dust mass density. Along a line of sight, the optical depth is given by (Michel-Dansac et al., 2020)

$$\tau = \int_0^\ell n\sigma(\nu)\mathrm{d}\ell = \int_0^\ell \rho\kappa(\nu)\mathrm{d}\ell \tag{2.2}$$

where ℓ is the length of the path along the line of sight, n is the (pseudo) number density of dust while ρ is the mass density of dust, and similarly $\sigma(\nu)$ and $\kappa(\nu)$ are absorption cross-sections either per dust grain or per dust mass respectively. The densities and cross-sections are determined by the choice of model. Pseudo-densities have different normalizations, but this is made up for by the $\sigma(\nu)$ curve also having a different normalization, which allows it to reproduce τ accurately.

Two commonly used dust models to model attenuation in the early Universe are calibrated on extinction curves in the Large Magellanic Cloud (LMC) and Small Magellanic Cloud (SMC) respectively. These models are commonly used due to the LMC and SMC having low metallicities. This makes them comparable to galaxies in the early Universe. The LMC and SMC are also smaller galaxies, once more creating a direct comparison with the early Universe.

To model the pseudo number density of dust in an Obelisk simulation cell, these models both assume the same formula (Laursen et al., 2009):

$$n = \frac{Z}{Z_{\mathrm{ref}}}(n_{\mathrm{HI}} + f_{\mathrm{ion}} n_{\mathrm{HII}}). \tag{2.3}$$

This implies that the number density of dust is dependent on metallicity, both in neutral hydrogen and ionized hydrogen regions. Laursen et al., 2009 and Michel-Dansac et al., 2020 choose the values $Z_{\mathrm{ref}} \sim 0.005(0.01)$ for the SMC (LMC) model and $f_{\mathrm{ion}} \sim 0.01$ for both. The parameter f_{ion} is meant to serve as a substitute for the destruction that dust undergoes while in shocked regions. Shocked regions are typically ionized due to their high temperatures. Other destruction methods, such as sputtering, are also more efficient with higher temperatures. This all implies there is less dust present in ionized hydrogen regions than in neutral hydrogen regions. The factor f_{ion} is meant to model this in a practical fashion.

The empirical fitting functions for the LMC and SMC dust extinction laws are given by

$$\sigma_\nu = \sigma_0 \sum_{i=1}^{7} f(\lambda/\lambda_i, a_i, b_i, p_i, q_i) \tag{2.4}$$

(Pei, 1992, Gnedin et al., 2008) where

$$f(x, a, b, p, q) = \frac{a}{x^p + x^{-q} + b}. \tag{2.5}$$

The extinction laws, therefore, are made up of seven individual profiles. The parameters λ_i, a_i, b_i, p_i, and q_i have unique values for each profile, and are different for both

extinction laws, while σ_0 is a normalization factor unique for both models. Values for these are taken from Gnedin et al., 2008, which are slightly changed from Pei, 1992 to better fit the extinction curves found by Weingartner and Draine, 2001. The curves for $\sigma(\nu)$ for the LMC and SMC models are shown in Figure 2.2. This collection of publications also includes a dust model based on the Milky Way extinction curve. The Milky Way model is typically only used in the late Universe, since the Milky Way is highly evolved whereas the LMC and SMC are less so. Due to this reason, the Milky Way model is not used in this thesis.

Another commonly used model for dust attenuation is the BARE-GR-S model, first proposed by Zubko et al., 2004. This model assumes bare silicate and graphite grains, as well as including PAHs. Zubko et al., 2004 propose several different models, with other grain populations taken into account, but find that the BARE class of models better reproduces observations. The GR subclass indicates that the primary component of carbon in these models is in the form of graphite, not amorphous carbon. The suffix S stands for solar abundances of metals being taken into account.

To calculate the number density of dust, the Rascas implementation of BARE-GR-S by Katz et al., 2022c follows the calculation of Rémy-Ruyer et al., 2014, using the broken power law model for the $X_{\mathrm{CO,Z}}$ conversion factor. Rémy-Ruyer et al., 2014 aim to measure the gas-to-dust ratio in nearby galaxies, and assume the BARE-GR-S model for dust attenuation. The X_{CO} is a conversion factor used in observations to convert between CO line intensity and H_2 mass. The $X_{\mathrm{CO,Z}}$ model assumes a $(\mathrm{O/H})^{-2}$ scaling relation. The broken power law model then calculates a gas-to-dust ratio. To convert this into a number density for dust, it is transformed according to (Katz et al., 2022c)

$$n = n_{\mathrm{H}} \left(\frac{(G/D)_{\odot}}{(G/D)_{\mathrm{model}}} \right) \tag{2.6}$$

where $(G/D)_{\odot}$ is the solar gas-to-dust ratio, which for BARE-GR-S is set to 1/0.00619 (Rémy-Ruyer et al., 2014). n_H is the hydrogen density in the cell, both ionized and unionized. This implicitly assumes that dust grain properties do not change as a function of metallicity. To correct for the fact that dust is destroyed at very high temperatures, as this is not taken into account in this model, n is set to 0 wherever the temperature exceeds 10^5 K.

The BARE-GR-S model data for $\sigma(\nu)$ as implemented into Rascas by Katz et al., 2022c are simply read from a table. However, this table does not hold for wavelengths above 10000 Å or below 500 Å. This is visible in Figure 2.2 as a flat line for σ_D below 500 Å. Also notable is the difference in normalization between the LMC, SMC, and BARE-GR-S models, which can be seen as the height of the σ_D curve.

The Obelisk dust model is the model used in the Obelisk simulation, and aims to give a more physical motivation to the dust content in the simulation. I will briefly

highlight its main properties as implemented by Trebitsch et al., 2021 in their simulation. The Obelisk model consists of a subgrid model, which aims to find a dust mass for each individual cell in the simulation. To do so, the model keeps track of the creation and destruction of dust in each cell. Adapting Equation 2.1, which also keeps track of dust mass, into Obelisk, several factors are changed significantly. Instead of tracking dust mass on a galaxy-wide level, dust should be tracked on a cell-wide level. However, the same physics still apply. I will briefly provide a short overview of the changes that are relevant to the Obelisk dust model. Since in the Obelisk simulation dust flow is coupled to gas flow, $\dot{I}_d$ and $\dot{O}_d$ are automatically tracked in the hydrodynamic step of the simulation. These factors can therefore be neglected in this discussion.

Estimating $\dot{Y}_d$ is done by assuming $f_{d,SN} = 50\%$ of metal mass ejected by supernovae is assumed to be in the form of dust, while AGB contribution is not tracked, based on values explored by Popping et al., 2017. These are some limiting factors on the physical accuracy of the model, but the yields of dust by supernovae is currently very unconstrained (Bianchi & Schneider, 2007) and highly dependent on the properties of the star (Marassi et al., 2019).

Since dust is passive in Obelisk, $\mathcal{D}_{ISM}\psi(t)$ is also automatically tracked by just following star formation in the simulation. The fraction of dust is only used for post-processing, and does not play a role in the hydrodynamics or the physics of star formation. Therefore, any region where metals in gas are assimilated into star particles will also act as sinks for dust mass in the ISM.

For the destruction of dust by supernova shocks $\dot{D}_{SN}$, each cell is updated individually. It is assumed that only gas shocked to velocities higher than $100\,\mathrm{km\,s^{-1}}$ destroys dust, shown in the formula (Trebitsch et al., 2021)

$$\dot{D}_{SN} = 0.3\frac{M_{\mathrm{s,SN}}}{M_{\mathrm{gas}}}M_d \tag{2.7}$$

where $M_{s,SN}$ is the shocked gas mass in a cell, and M_{gas} and M_d represent the local gas and dust mass respectively. The factor 0.3 assumes 30% destruction of gas in these regions. The total amount of shocked gas is given by

$$M_{\mathrm{s,SN}} \simeq \frac{E_{\mathrm{SN}}}{0.736(100\,\mathrm{km\,s^{-1}})^2} \simeq 6800 E_{\mathrm{SN},51} M_\odot \tag{2.8}$$

following the Sedov solution as presented by McKee, 1989.

This total shocked mass needs to be distributed over several cells, since supernovae affect the ISM at larger scales than Δx. To distribute this mass, the supernova subgrid model present in Obelisk is used, following the distribution of energy.

The net growth of dust grain particles by taking accretion and sputtering into account can be captured in a single equation (Trebitsch et al., 2021):

$$\dot{G}_{ac} = \left(1 - \frac{M_d}{M_Z}\right)\frac{M_d}{t_{\mathrm{growth}}} - \frac{M_d}{t_{\mathrm{sput}}} \tag{2.9}$$

M_Z is the metal mass in the cell, and $t_{\rm growth}$ and $t_{\rm sput}$ are timescales for growth via accretion and destruction via thermal sputtering respectively. These timescales are easily calculated due to the single population assumption in Obelisk. Trebitsch et al., 2021 find that, using this model for dust growth, for temperatures below $T \simeq 3 \times 10^4\,\mathrm{K}$ the growth channel dominates, allowing grains to grow in these environments. All these features allow the Obelisk simulation to recreate a cell-based dust mass density throughout the entire simulation, instead of the commonly used approach in simulations of using a single dust-to-gas fraction for the full volume, or in other attenuation curve models of providing a single formula for its dust number density. This model should therefore be more in line with the reality of observed galaxies, making this my fiducial model.

Differing from the other dust models introduced so far, the Obelisk model finds a dust mass density instead of a pseudo dust number density. This means that, instead of the model providing an attenuation cross-section $\sigma(\nu)$, it provides a dust absorption coefficient $\kappa(\nu)$. The cross-section is derived from fitting a function of the form of Equation 2.5 to a synthesized attenuation curve (Trebitsch, private communication). Details on this process will be featured in a future work (Dubois et al., in prep.). The fitting is done to decrease computational load, as the full attenuation curve is not analytical. These fitted parameters form a function for $\kappa(\nu)$, which is included in the Obelisk model. The resulting curve for $\kappa(\nu)$ is shown in Figure 2.2. The implementation of the Obelisk model into Rascas was done by Maxime Trebitsch (Mauerhofer, private communication).

The Obelisk dust model aims to capture the complexity of the properties of dust in a galaxy by tracking its creation, growth, and destruction over time. Combined with the spatial distribution, this model is more complex than an attenuation law based on the metallicity of a cell. However, these simpler models such as SMC, LMC, and BARE-GR-S are able to be used in a wider number of applications, since they are not bound to a simulation like Obelisk is. By comparing the Obelisk model to these other models, it is possible to find the closest match of Obelisk to these models for several observables. This can be used to inform the choice of dust model when only the attenuation models (SMC, LMC, and BARE-GR-S) are available.

Lastly, to test the overall influence that dust has on a spectrum, a model with dust fully absent, coined `nodust`, is included in the analysis. This gives a baseline value to compare against for each different dust model. To remove the interaction between dust and light, the dust attenuation cross-section and number density of dust are simply artificially set to 0.

The variety on display in dust models reflects the variety of dust properties between galaxies. The Obelisk model aims to generalize a dust model in the context of simulations. To compare these models, spectral properties of galaxies can be compared in these simulations. This is done by generating mock observations using the Rascas code.

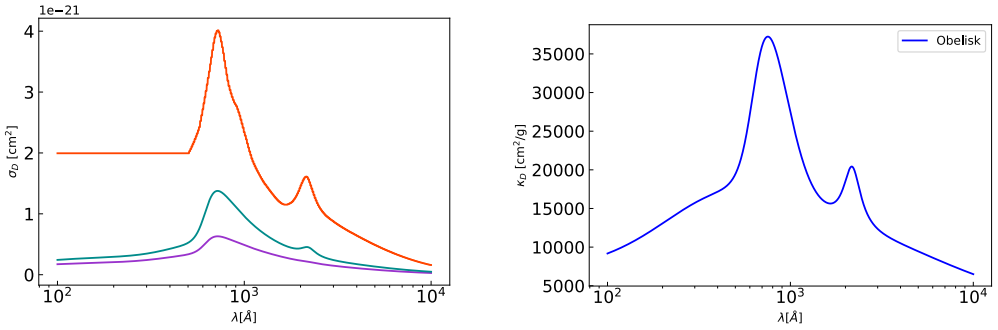

Figure 2.2: Dust models compared. Left plot: $\sigma(\nu)$ as a function of wavelength for the BARE-GR-S, LMC, and SMC models. Right plot: $\kappa(\nu)$ for the Obelisk model. Note the presence of the 2175 Å feature for most of these models, but the absence of this feature for the SMC model.

2.3 RASCAS

The Rascas[1] (RAdiative SCattering in Astrophysical Simulations) (Michel-Dansac et al., 2020) code is a software package designed to simulate the emission of stars and gas from a hydrodynamical simulation. It is designed to capture the interaction between dust, gas, and light to a highly accurate level, on an arbitrary geometrical distribution. It acts as a post-processing code, building on an already existing simulation. The results can be used to generate mock observations, such as spectra or images, from these initial simulated galaxies. Primarily, the code is designed to recreate resonant absorption and emission lines, but the code is designed to be flexible enough to also capture the stellar continuum, fluorescent lines, and the ionizing part of the UV spectrum.

The main code of Rascas acts in three steps: gathering the data from the simulation to create a domain decomposition, creating initial conditions for emission, then solving the radiative transfer equations in a highly parallel fashion. This domain decomposition is done using the builtin code `CreateDomDump`, which reads the simulation data and decomposes it into several smaller domains. The data being read includes the composition of gas, including hydrogen species, gas velocities, and density of dust. The reading is a unique process for each different simulation code. Rascas was originally developed to support Ramses-RT-based simulations. Obelisk is created using Ramses-RT, which means that no additional code was required to read the simulation. After reading the data, they are put in a data domain according to a specific geometry. Important in the creation of this decomposition is that the data domain of acquired simulation data is larger than the computational domain, at which photons are assumed to be escaped from the halo and are no longer propagated. This domain can be put

[1] http://rascas.univ-lyon1.fr/

around any halo, allowing for this code to target individual halos. For this thesis, I always set the data domain to be a sphere with radius $1.2r_{vir}$, with the computational domain being set to a sphere with radius r_{vir}, where r_{vir} is the virial radius of the halo. The data domain is then assigned to a mesh based on an octree structure (which could have to be adapted from the structure that the simulation uses, depending on the original simulation code used) and stored on disk. This procedure needs to be applied individually per halo and for each dust model used, since the dust content of a halo is dependent on the model used.

The second part of the code deals with generating the initial conditions, before radiative transfer can occur. This is done using the code `PhotonsFromStars`. This code takes in the stellar particles of the simulation, each of which is a single population with the same age and metallicity, and from there creates an initial spectrum. This can be done in several ways, through a power law for the continuum, as a Gaussian shape for individual absorption and emission lines, as a monochromatic line, or, as used in this thesis, from an existing SED table for the continuum. To be specific, I use the BPASS model, version 2.2.1 (Stanway & Eldridge, 2018), following Trebitsch et al., 2021. The code then estimates the luminosity of each stellar particle based on its properties, and spreads out N_{phot} photon packets over the set according to this distribution. The selection of N_{phot} is discussed in §2.3.2. At emission, the wavelength is also sampled using these stellar population models. Wavelengths are derived in the frame of the particle, but then converted using its velocity and direction to a wavelength in the frame of the halo. Together, this creates a set of initial conditions for emissions from the stellar particles in the simulation, to be processed later. These can be generated once for each halo, since they are not dependent on dust.

The third section of RASCAS, `rascas`, solves the radiative transfer equations for the initial conditions provided by `PhotonsFromStars` through the medium provided by `CreateDomDump`. This is done using a Monte Carlo method, where every photon gets allotted an optical depth τ_{event} drawn from $-\ln(r)$, where r is a draw from a uniform distribution on the range $[0; 1]$. The photon packets are then transferred along rays, where they will encounter the dust and gas mediums. In every cell, the optical depth τ_{cell} of the cell along the propagating line is subtracted from τ_{event}. The general optical depth (Equation 2.2) can be simplified in each cell, since in each cell the dust properties are homogeneous. Equation 2.2 then becomes (Michel-Dansac et al., 2020)

$$\tau_{\text{cell}} = n\sigma(\nu)\ell \tag{2.10}$$

where ℓ is the length of the path the photon packet travels through the cell.

In this thesis, two different versions of RASCAS are used, the `new_ions` branch, and the `mock-lyc`. These differ in what types of interactions take place between photons and the medium. Both branches take dust absorption and scattering into account, but

differ in that the `new_ions` branch takes scattering due to absorption and emission lines into account, while the `mock-lyc` takes in absorption of LyC photons due to gas into account. Because the `mock-lyc` branch is specifically focused on the LyC, this branch is exclusively used on the range $200 - 1000$ Å, while the `new_ions` branch takes over on the range $1000 - 10000$ Å. In this thesis, I am interested in the LyC continuum and the UV continuum, not the absorption and emission lines. This means that I will ignore the absorption lines completely, and omit them from my analysis. This heavily increases computational speed, at the cost of losing these features in the generated spectra.

For the `mock-lyc` branch, therefore, the optical depth for the transfer through a single cell can be calculated as such (Michel-Dansac et al., 2020):

$$\tau_{\text{cell}} = \tau_{\text{dust}}(\nu) + \sum_{X}^{\text{species}} \tau_X(\nu), \tag{2.11}$$

with τ_{dust} being the optical depth belonging to dust, with X being an individual species of gas taken into account, and τ_{X} being the optical depth due to this species. In this analysis, $X \in \{$ HI, HeI, HeII $\}$. When τ_{event} is equal or lower than 0, an event occurs. This event can occur on dust, or on gas. What type of event occurs is randomly determined, heightening the Monte Carlo nature of Rascas further. A random draw r is performed on the range $[0; 1]$, and is compared to $\tau_{\text{dust}}/\tau_{\text{cell}}$. If $r < \tau_{\text{dust}}/\tau_{\text{cell}}$, an event due to dust takes place, otherwise an event due to gas takes place (Michel-Dansac et al., 2020). For the `new_ions` branch, $\tau_{\text{gas}}(\nu) = 0$, so only dust events take place.

Combining equations 2.10 and 2.11 gives (Michel-Dansac et al., 2020)

$$\tau_{\text{cell}} = \left(n_{\text{dust}}\sigma_{\text{dust}}(\nu) + \sum_{X}^{\text{species}} n_X \sigma_X(\nu) \right) \ell. \tag{2.12}$$

n_X are all read from the domain decomposition created in the `CreateDomDump` phase. Similarly, n_{dust} is constructed here as well. The method for doing this is unique per dust model, and described in §2.2.1.

To calculate the photoionization cross-section of the gas species, two approaches can be used. The hydrogenic species HI and HeII have analytic solutions, given by

$$\sigma(\nu) = \frac{A_0}{Z^2} \left(\frac{\nu_1}{\nu} \right)^4 \frac{e^{4 - 4\tan^{-1}(\epsilon)/\epsilon}}{1 - e^{-\frac{2\pi}{\epsilon}}}, \tag{2.13}$$

(Osterbrock & Ferland, 2006) where Z is the nuclear charge,

$$A_0 = \frac{2^9 \pi^2 \alpha a_0^2}{3e^4} = 6.30 \times 10^{-18}\,\text{m}^{-2}, \tag{2.14}$$

$$\epsilon = \sqrt{\frac{\nu_1}{\nu} - 1}, \tag{2.15}$$

and

$$h\nu_1 = Z^2 h\nu_0 = 13.6 Z^2 \text{eV}. \tag{2.16}$$

However, this equation does not hold for HeI, since it is not hydrogenic. There is no analytic solution found. However, following the model by Verner et al., 1996, the photoionization cross-section for any species can be given by the empirical function (Verner et al., 1996)

$$\sigma(E) = \sigma_0\left[(x-1)^2 + y_W^2\right] y^{0.5P-5.5}\left(1+\sqrt{\frac{y}{y_a}}\right)^{-P} \tag{2.17}$$

Here, $x = E/E_0 - y_0$, and $y = \sqrt{x^2+y_1^2}$. The fitting parameters σ_0, E_0, y_W, y_a, y_0, y_1, and P are taken from Verner et al., 1996 for HeI. The values for HI and HeII are also included, since these equations are less computationally expensive than the analytic solution. Due to this, the empirical equations are preferred and used in this thesis. The analytic functions may be used if accuracy is of the highest priority.

Events can either be absorption events or scattering events. In the case of gas, absorption always takes place. Here, a photon will hit an atom with at least one electron, and has enough energy to ionize the atom. This process absorbs the photon. The photon packet is then removed from the radiative transfer, and flagged appropriately. Similarly, photon packets absorbed by dust are also removed from propagation, but with a different flag to signify the source of absorption taking place.

When interacting with dust, there is a likelihood that the radiation gets scattered. This is determined by the albedo of the dust particle, which is a function of wavelength. In this thesis, the albedo curves as tabulated by Li and Draine, 2001 are used, with interpolations for intermediate wavelengths. The probability that a photon is scattered is given by P_{abs} = albedo (Michel-Dansac et al., 2020). If scattering takes place, the direction at which the photon is scattered is given by the Henyey-Greenstein (Henyey & Greenstein, 1941) function

$$P_{HG} = \frac{1}{2}\frac{1-g^2}{(1+g^2-2g\mu)^{(3/2)}}, \tag{2.18}$$

where $\mu = \cos(\theta)$, and $g = \langle\mu\rangle$ is the asymmetry parameter, also as determined by Li and Draine, 2001. To introduce stochastic behaviour into this scattering, the value for μ is sampled using

$$\mu = \frac{1}{2g}\left(1+g^2+\frac{1-g^2}{1-g+2gr}\right), \tag{2.19}$$

(Michel-Dansac et al., 2020) where r is once more a sample from the uniform distribution in $[0;1]$. The wavelength of the photon also changes, due to the velocity of the dust. The velocity of the dust is assumed to be the same as the velocity of the gas. The updated frequency is given by (Mauerhofer, 2021)

$$\nu_{\text{ext,new}} = \frac{\nu_{\text{cell}}}{1-(\mathbf{k}_{\text{new}}\cdot\mathbf{v}_{\text{dust}}/c)}, \tag{2.20}$$

where ν_{ext} is the updated frequency in an external reference frame, ν_{cell} is the frequency in the reference frame of the cell, $\mathbf{k}_{\text{new}}$ is the unit vector along the new direction, and $\mathbf{v}_{\text{gas}}$ is the velocity of the gas. ν_{cell} is constant before and after the scattering, and can be calculated by (Michel-Dansac et al., 2020)

$$\nu_{\text{cell}} = \left(1 - \frac{\mathbf{k}_{\text{old}} \cdot \mathbf{v}_{\text{dust}}}{c}\right)\nu_{\text{ext,old}}. \tag{2.21}$$

This updated frequency is then taken into account for the next scattering event, and kept track of until the photon packet terminates propagation, be that due to absorption or escape.

Once all photon packets that were originally emitted from the stars have been propagated either until they are absorbed or until they have reached the end of the computational domain, the results are saved. Escaped photons too have a unique flag. These flags will later be used to identify the final result of each photon packet. In the end, each photon packet will obtain information about whether it was absorbed or escaped, its wavelength, its final direction and scatter position, and the number of scattering events. These properties are all stored on disk, so that a spectrum can be reconstructed after this.

2.3.1 Reconstructing the spectrum

Once the three main programs of Rascas have terminated, it is immediately possible to generate observations that are angle-averaged over the whole halo. Since I am using a spherical domain, this would be across the full 4π steradians. This is done by extracting the information directly from the photon packets. Each photon packet can be transformed into a flux corresponding to that packet by using $F_\lambda = N_{\text{phot}}\nu h$, where N_{phot} is the physical number of photons represented by the photon packet, ν is the frequency information of the photon packet, and h is the Planck constant (Michel-Dansac et al., 2020). The fluxes from each packet are then binned in a histogram to form a spectrum. This process is useful to generate global properties of a halo, such as the escape fraction. However, this is an idealized situation. The luxury of simulations gives the opportunity to study these global properties, but for observations this is impossible, since they are limited to a single viewing direction. It is also often fruitful to study the properties of a galaxy along a certain direction, since many observed properties change significantly with viewing angle, such as the escape fraction. Simulations allow one to view the same halo from many directions, and to compare global properties with properties along one viewing angle. For these reasons, Rascas has implemented a method for generating mock observations from the photon packets. This is done using the peeling-off algorithm (Dijkstra, 2017). The main idea here is to create an aperture at a certain position at the edge of the computational domain through which escaping photons can be captured and turned into a spectrum using a similar procedure as for

the whole halo. However, simply counting the number of photons passing through such an aperture will quickly lead to problems. Since the size of these apertures is typically fairly small compared to the sphere, many photon packets will simply escape without ever being accounted for in an aperture, since $\Omega_{\text{aperture}} \ll 4\pi$, even when applying many apertures. This means that the full spectrum will not be sampled correctly, since due to the Monte Carlo nature of RASCAS a large number of photon packets are required to properly reconstruct a spectrum. To combat this, the aperture size could be increased. However, the reason apertures are used is to view a galaxy along a single direction similar to observations, which necessitates a small angular size for any aperture. Increasing the aperture size would therefore counteract the benefits gained by using apertures. The number of photon packets may also be increased significantly to provide enough photon packets per aperture to properly reconstruct the spectrum. However, the angular size of the apertures is negligible compared to the sphere, and therefore the quantity of photon packets needed would have to increase drastically, increasing computational loads with them.

Due to these problems, the peeling-off algorithm (Dijkstra, 2017) uses a different approach (Dijkstra, 2017). Every interaction between a photon packet and dust is treated as a point source with luminosity L/N, with L being the total luminosity of the source and N being the total number of photon packets. At each interaction, a small amount of flux is "peeled off" and sent toward each aperture. An illustration of this concept can be seen in Figure 2.3.

From these sources, the flux going into each aperture can be calculated using

$$S = \frac{L}{N} a(\nu_{\text{cell}}) P_{HG}(\mu) e^{-\tau_{\text{path}}(\nu_{\text{ext}})} \tag{2.22}$$

(Dijkstra, 2017). In this formula, L/N denotes the total luminosity of each individual interaction. $a(\nu_{\text{cell}})$ is the albedo of the dust particle, which means that even if absorption of a photon packet takes place, there is still a probability of some light scattering away from an interaction. This mimics the behaviour of actual photons. Since a photon packet is made up of a large quantity of modelled photons, a fraction of which would end up scattering in a realistic situation. The inclusion of the probability of scattering even if the main packet is absorbed simulates this behaviour. P_{HG} is the Henyey-Greenstein phase function (Equation 2.18), since in this implementation, only dust scattering is taken into account. μ here is $\mathbf{k}_{\text{in}} \cdot \mathbf{k}_{\text{out}}$, where $\mathbf{k}_{\text{in}}$ is the incoming direction of the photon packet, and $\mathbf{k}_{\text{out}}$ is the direction between the point of scattering and the aperture. $\tau_{\text{path}}(\nu_{\text{ext}})$ is the optical depth at frequency ν_{ext} along the path from the point of scattering to the aperture. This is calculated along a direct line, where the implicit assumption is that any light from this scattering does not scatter again. If $\tau_{\text{path}}(\nu_{\text{ext}}) < \tau_{\text{max}}$, S is set to 0 automatically. RASCAS has set τ_{max} equal to 60. This is done to speed up calculations, since at high $\tau_{\text{path}}(\nu_{\text{ext}})$, the value of $e^{-\tau_{\text{path}}(\nu_{\text{ext}})}$ becomes negligible. Each interaction between dust and photon packets is therefore captured in some form for each aperture. The strong dependence of τ_{path} and $P_{HG}(\mu)$ on the propagating direction ensure that the spectra obtained from each aperture are not angle

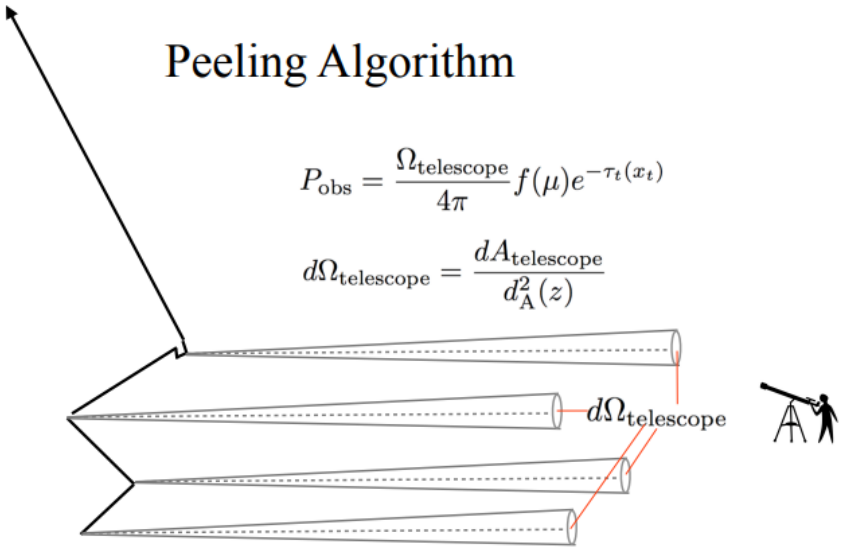

Figure 2.3: Illustration of the nature of the peeling-off algorithm. The probability that a photon packet directly intersects with an aperture is near zero, making an approach like this necessary. Note that at every scattering event, a point source of light is created. Flux from this point source is then emitted towards an observer. This allows photon packets to propagate in any direction and contribute to the flux of any aperture, without having to interact with that aperture directly. This allows Monte Carlo methods to create mock observations from different viewing directions. Image reproduced from Dijkstra, 2017.

averaged, but are unique for each viewing direction.

As many apertures can be placed as one wishes around a given halo. It is wise here to equally distribute the apertures around the sphere. In this thesis, the HEALPix[2] scheme (Górski et al., 2005) is used to determine the distribution. This scheme aims to create a pixelization mapping of the sphere, which keeps the points well spaced from each other. The total number of apertures used in this thesis is 12 per halo, the distribution of which according to the HEALPix scheme is shown in Figure 2.4. The sphere can be subdivided into more pixels, meaning more apertures, but this would also increase computational load.

Rascas is also able to use the same peeling-off algorithm to create images, and create data cubes combining spectra and images. The intrinsic behaviour of gathering fluxes from interactions between dust and photons remains the same, only the processing at the aperture changes.

[2] https://healpix.sourceforge.io/

2.3.2 Selecting the number of photon packets

The Monte Carlo approach of RASCAS requires many photon packets to be propagated to properly sample the spectrum. When using too little, one risks undersampling the distribution and introducing errors in the extracted observables. But when propagating too many photons, the computational load increases. As pointed out in the previous section, the computational load of RASCAS is not negligible, with approximations such as faster empirical functions for gas absorption optimizing the speed. The number of photon packets is one of the most important parameters in tweaking both the computational speed as well as the data volume created by RASCAS, so overestimating this number is also to be avoided. To pinpoint a number of photon packets $N_{\rm phot}$ that balances these two issues, I provide a short analysis.

RASCAS initializes photon distributions over all the stellar particles available in the halo. This creates a hypothesis that halos with more stellar particles require more photon packets to properly sample their spectra. To check the verity of this hypothesis, I will perform this analysis on 4 different halos, each with different stellar masses and number of stellar particles. The details of these halos can be found in Table 2.1.

Halo ID Number	Stellar particles	Stellar Mass [log $M_\odot$]	Central Halo
14215	6063937	10.6	Yes
71356	435508	9.40	Yes
5969	2772	7.15	Yes
87918	27273	5.89	No

Table 2.1: Selected properties of the halos used for the determination of $N_{\rm phot}$. These halos have been selected on their wide distribution of mass ranges. The "Stellar Particles" column denotes the number of stellar particles inside of the computational domain of the halo, set to $r_{\rm vir}$ in this work. The last column states whether this halo is a central halo or if it is a subhalo of a larger halo, as found by the ADAPTAHOP halo finder (Aubert et al., 2004) in OBELISK. For halo 87918, the stellar particle count is contaminated by its host halo, halo 44228. The number of stellar particles in the structure of halo 87918 itself is 131.

To start off with this analysis, several spectra in the UV continuum are created, each with a unique number of photon packets. These are 100k, 250k, 500k, 1M, and 10M photon packets. Three observables are then taken into account here, the noise level on the 9000-10000 Å range, the UV continuum slope between 1500-3000 Å, and the UV escape fraction between 1500-3000 Å. The UV continuum slope should not change significantly unless severe undersampling takes place, while the noise should decrease with photon number due to the better sampling. The noise is here defined as $\sigma_{\rm spec}/\mu_{\rm spec}$, i.e. the standard deviation of the spectrum divided by the mean. The wavelength range was chosen due to the flatness of the spectrum along that range, making $\mu_{\rm spec}$ less dependent on wavelength. Escape fractions are typically highly dependent on galaxy properties, so it is highly important to select a value for $N_{\rm phot}$ that does not introduce

sampling errors. As a rule, the 10M photon packet run is seen as closest to the "true" value due to it having by far the highest number of photon packets. Therefore, it will be the standard against which other amounts are measured. These preliminary tests were done using the BARE-GR-S dust model. These observables are shown in Figure 2.5. From this figure, it is clear that the UV continuum slope and escape fraction stay relatively constant, until values around $N_{\rm phot}$ ∼500k. Noise decreases with increasing $N_{\rm phot}$. The computational time is also shown in Figure 2.5, which clearly increases with $N_{\rm phot}$. To balance the computational load with the accuracy of the results, $N_{\rm phot}$ = 500k photon packets is used in the rest of this thesis. During the analysis process, it was found that it is hard to distinguish the properties of halo 89718. Since this halo is a subhalo, contamination from its host halo 44228 was present. The computational domain included 27273 stellar particles, while halo 89718 only consists of 131 stellar particles (see Table 2.1). This contamination made it not possible to separate the intrinsic properties of halo 89718 from that of halo 44228. For the purpose of determining $N_{\rm phot}$ the contamination does not influence the results since only the consistency of observables over various values of $N_{\rm phot}$ is analyzed, but for further analysis of the properties of halos, this issue becomes important. This may not be true for all subhalos, but they are excluded from any further analysis due to the possibility of introducing large errors.

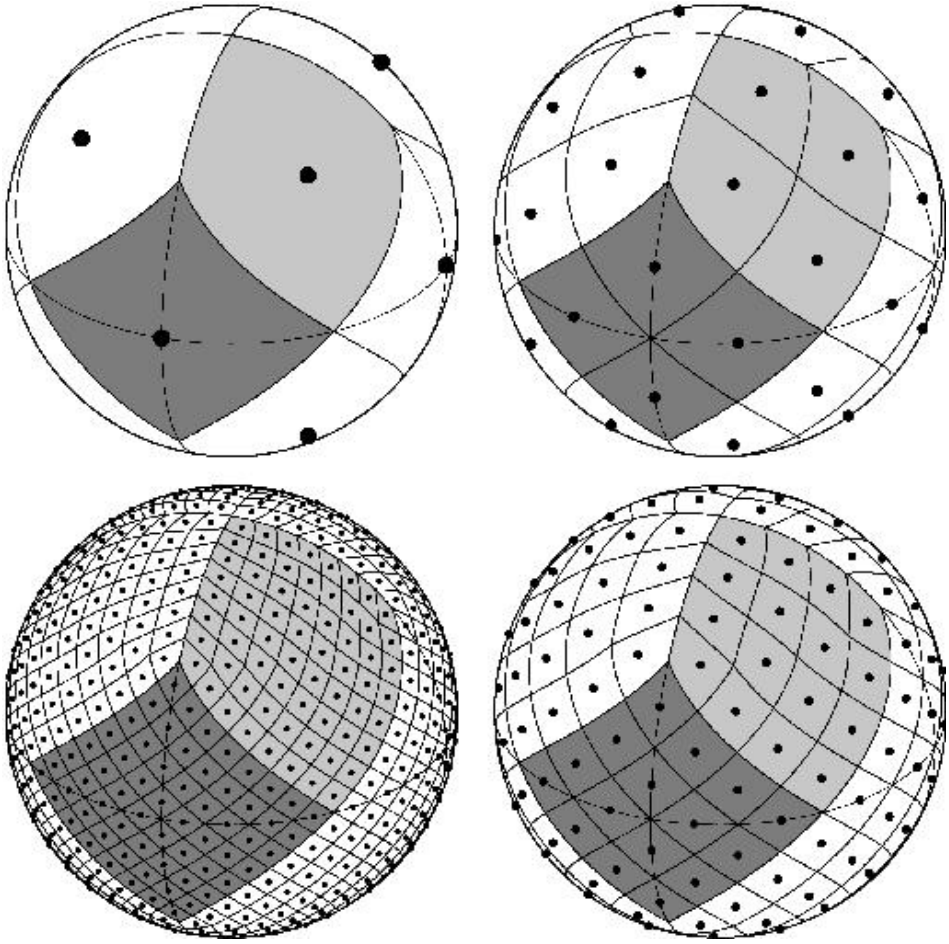

Figure 2.4: The distribution of apertures around the sphere according to the HEALPix scheme. Moving clockwise with resolution $N_{\rm side} = 1,\ 2,\ 4,\ 8$, resulting in $N_{\rm dir} = 12N_{\rm side}^2 = 12,\ 48,\ 192,\ 768$ pixels. The centers of these pixels correspond to aperture locations used to create mock observations. In this thesis, $N_{\rm side}$ is set to 1. Image reproduced from Górski et al., 2005.

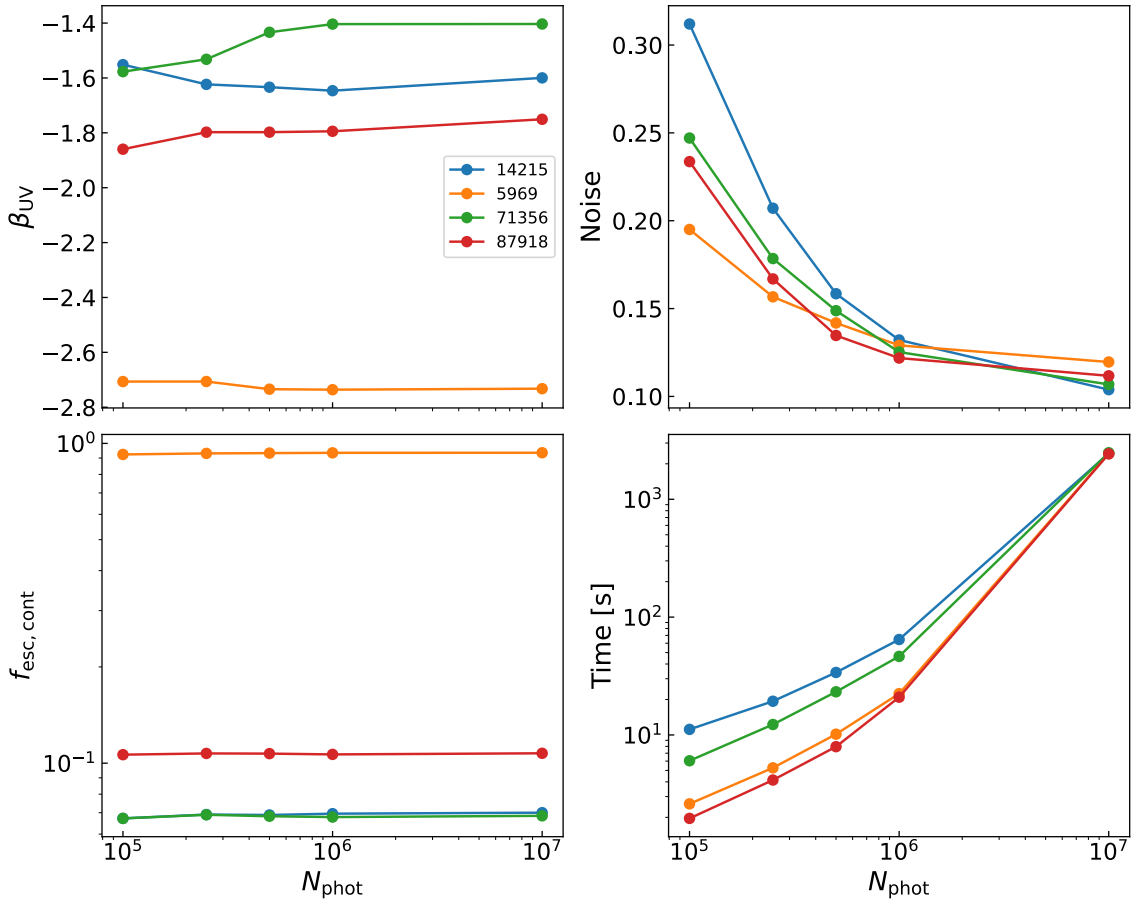

Figure 2.5: UV continuum slope, noise level, UV continuum escape fraction, and RASCAS computational time as a function of $N_{\rm phot}$. This illustrates the balancing act between accuracy and computational time, most notably the noise level between 9000-10000 Å. The 10^7 runs are seen as the "true" value. The four halos are chosen to span a range of different stellar masses (see Table 2.1).

Chapter 3

Results

In this chapter, I will highlight the main results and analyses done on the generated spectra from RASCAS. First, I will describe the main galaxy sample and its properties. Discussions about the UV continuum slope and the influence of the 2175 Å feature are stated in §3.2 and §3.3. In section §3.4, a discussion on the ionizing escape fraction is included. Finally, I will highlight the spectral distribution of dust absorption in section §3.5.

3.1 Galaxy Sample

My sample of halos from Obelisk consists of 554 halos, which are randomly selected with uniform probability from the general population in Obelisk of top-level halos. Subhalos are avoided due to possible contamination issues, as highlighted in section 2.3.2. The uniform selection ensures that the galaxy sample is a good match to the full galaxy population present in Obelisk. This can be seen in Figure 3.1, where the two populations show good agreement in their stellar mass distribution. Of the 554 halos, 5 have to be rejected (Halos 47370, 57352, 57355, 62944, and 69324). Rascas has difficulty dealing with very small halos, since it fails when the data domain and computational domain are equal. This is usually prevented by setting the radius of the data domain to $1.2r_{vir}$ while that of the computational domain is set to r_{vir}. In practice, however, this value is rounded down to the third digit, which for very small haloes may lead to setting the radii equal. If this occurs, Rascas fails to function properly. This only occurs for the 5 highlighted halos, which are excluded from further analysis.

For these halos, spectra are created using Rascas. A few sample spectra are shown in Figure 3.2. All these spectra are taken in the rest frame of the halo. Also note that this analysis does not include metallic absorption and emission lines. While this is possible to do with Rascas, these lines are computationally intensive to model, and are therefore better suited to be treated as individual lines instead of being part of the

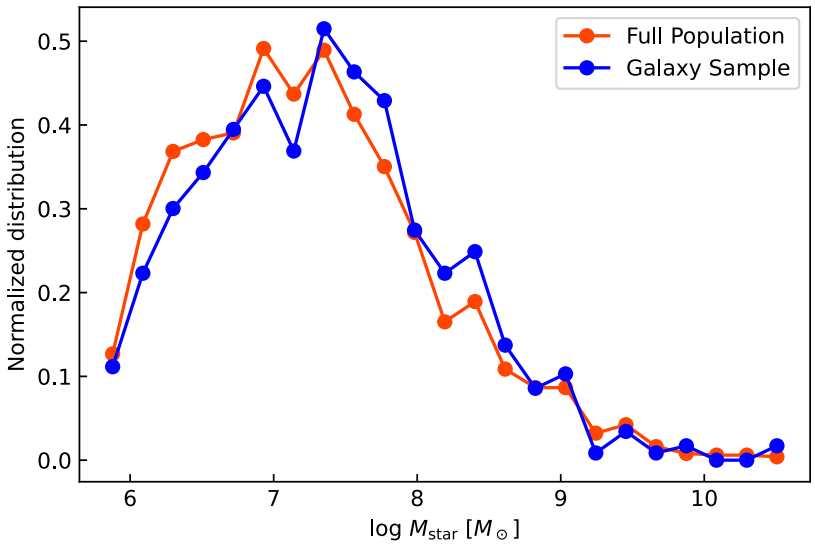

Figure 3.1: Normalized distribution of stellar masses for the whole OBELISK population compared to my sample population. This distribution samples overall slightly more massive halos than are present in the full population, due to the exclusion of subhalos in my sample.

continuum.

3.2 UV continuum slopes

A commonly used tool in studying galaxies is the UV continuum slope. Taking a spectrum of a galaxy reveals the UV continuum to have a power law shape, with absorption and emission features superimposed onto this continuum. This slope depends on the stellar population of the halo, as well as the dust attenuation within a galaxy. Flatter (redder) slopes imply an older population with more dust absorption, while steeper (bluer) slopes imply young stars with little absorption.

The method of calculating $\beta_{\rm UV}$, as well as the wavelength range on which it is calculated, does not have an agreed-upon standard (e.g. Bunker et al., 2023 uses $1500 < \lambda_{\rm rest} < 2600$ Å, while Curtis-Lake et al., 2023 uses $1250 < \lambda_{\rm rest} < 2600$ Å and Cullen et al., 2023 uses $\lambda_{\rm rest} < 3000$ Å). This is partially due to observational constraints, since photometry leads to having fewer data for a spectrum, and redshift corrections introduce an offset for any wavelength range. However, the slope of a single galaxy does not vary significantly along the wavelength region between Lyα at 1216 Å and the Balmer break at 3645 Å, so as long as the measurement takes place in that range it should be accurate. In my analysis, the wavelength range taken into account is 1500-3000 Å. To calculate the UV continuum slope, I assume a power-law model for

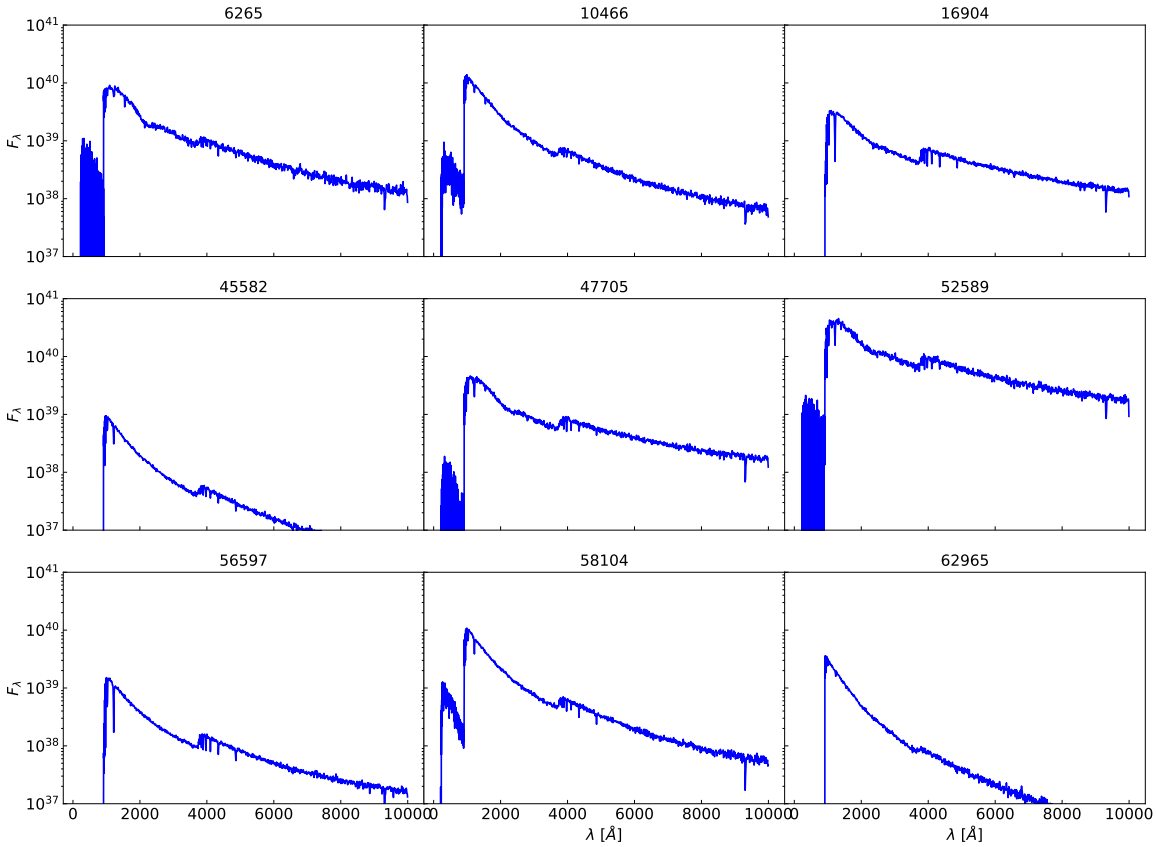

Figure 3.2: Spectra of nine sample halos created using RASCAS. Every spectrum is angle-averaged and created using the Obelisk dust model. These spectra show that the spectra are as intrinsically varied as the halos they come from.

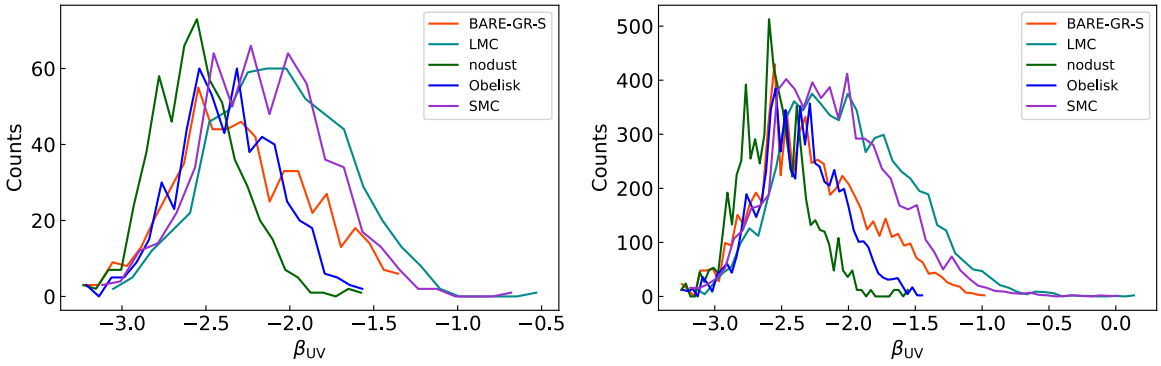

Figure 3.3: *Left:* Counts of UV continuum slopes of each individual halo, using the angle-averaged spectra. *Right:* Same as left, but for each individual viewing direction. The distribution for the angle-averaged slope and single-direction are very similar for each model, indicating no major directionality of the UV continuum slope.

Dust model	Obelisk	BARE-GR-S	LMC	SMC	`nodust`
$\langle\beta_{\rm UV}\rangle$	-2.37	-2.28	-2.06	-2.15	-2.55
$\Delta\beta$	0.30	0.40	0.39	0.38	0.25

Table 3.1: Mean and standard deviation of UV continuum slope distribution, assuming $\beta_{\rm UV}$ is normally distributed for the entire population. This population consists of 549 halos, with stellar masses ranging from $10^6 M_\odot$ to $10^{10.5} M_\odot$, at $z = 6$.

the UV continuum $F_\lambda = \alpha\lambda^\beta$ (after Calzetti et al., 1994), which in logarithmic space becomes

$$\log(F_\lambda) = \alpha + \beta \log(\lambda). \tag{3.1}$$

This model is fitted to the data on the provided wavelength range. This yields the UV continuum slope. The distribution of these slopes as derived from the spectra can be seen in Figure 3.3. This figure shows that the `nodust` model predicts the steepest continuum curves overall, as is to be expected, since this model does not feature any dust that may flatten the slope through absorption. The LMC and SMC models both predict relatively flat continuum slopes, with BARE-GR-S and Obelisk falling in between. The average continuum slope, as well as the standard deviation, are shown in Table 3.1. These values are in agreement with those found by Bouwens et al., 2014, who find $\beta_{\rm UV} = -2.24 \pm 0.11 \pm 0.08$ at $z = 6$ using fitting on photometric data from the CANDELS fields, and Bhatawdekar and Conselice, 2021, who find $\beta_{\rm UV} = -2.22^{+0.08}_{-0.12}$ at $z = 6$ based on Hubble Frontier Field data, with only the `nodust` model predicting steeper slopes than predicted by these observations.

3.3 2175 Å bump

A common feature seen in extinction curves is the 2175 Å bump, caused by PAHs. Recent observations have provided the first glimpses of this feature in EoR galaxies (Witstok et al., 2023b, Markov et al., 2023), leading to an increased interest in this type of dust in the early Universe. These carbonaceous grains are mostly assumed to appear as the galaxy evolves (Witstok et al., 2023b) since they are thought to be created through AGB stars (Ferrarotti & Gail, 2006), which are main sequence stars that have evolved to the end of their long lifespans. Since the presence of AGB stars takes time to develop on the order of Gyrs, carbonaceous dust is expected to be less common at high redshift (Dwek, 1998). The presence of this type of dust at these redshifts therefore may influence galaxy formation models. A different explanation for the presence of carbonaceous dust in these early galaxies is supernovae yields, so these discoveries may also influence supernova yield models.

Three of the dust models used in this analysis include a feature at 2175 Å, the LMC, BARE-GR-S, and Obelisk models. The effects that this feature has can be seen in some of the spectra created using these models, presenting itself as a pronounced dip in the UV continuum around the central 2175 Å region (see e.g. halo 6265 and 52589 in Figure 3.2). The introduction of this feature makes the UV continuum slope harder to measure, since it varies from the assumed power law distribution for the continuum. However, the properties of this absorption feature, such as the width or the amplitude, can provide insight into the dust contents of the host galaxy. To check for contamination and to find the properties of this feature, a new model for the UV continuum must be used, introducing the 2175 Å feature. The PAH absorption is typically modelled using a Drude profile (Draine & Li, 2007), which is similar to the function present in eq. 2.5, with p and q set equal to 2. After including the Drude profile in the UV continuum slope, I find the following function for the UV continuum:

$$\log(F_\lambda) = \alpha + \beta \log(\lambda) + \frac{A}{(\log \lambda/\lambda_i - \lambda_i/\log \lambda)^2 + (\Gamma_i/\lambda_i)^2}. \tag{3.2}$$

Here, α and β are still representative of the power law spectrum, while the third term is the added Drude profile. For this profile, A, λ_i, and Γ_i are fitted values, which are analogous to the amplitude, central wavelength, and width of the profile respectively. Equation 3.2 is fitted on the same 1500-3000 Å range as used in §3.2, in logarithmic space. This procedure did introduce some difficulties. The PAH feature is not present in every spectrum, nor every dust model. The fit also has to be constrained to avoid picking up noise. The parameter $\log \lambda_i$ was allowed to only vary between 3.3 and 3.4 to ensure the fit captures the 2175 Å feature. Similarly, A and Γ_i had to be constrained to warrant physically relevant results. This avoided misfits, but the absence of the feature in many spectra had to be accounted for too. To select what model is most accurate, two checks were made. First, a parameter boundary was included. The extreme value of the Drude profile was determined by $EV_{\text{Drude}} = A/(\Gamma_i/\lambda_i)^2$, which determines the depth of the profile in the center. If this extreme value is low ($EV_{\text{Drude}} < 2$) while the

Dust model	Obelisk	LMC	SMC	BARE-GR-S	`nodust`
N_{Drude}	271	310	40	293	5
N_{Flat}	278	239	509	256	544

Table 3.2: Distribution of detected PAH features between dust models. The three models which include a 2175 Å feature, Obelisk, LMC, and BARE-GR-S, have a similar number of detections. Notable is that SMC and `nodust` should not feature any detections, but are still present.

amplitude is large ($|A| > 0.04$) a fit is rejected, since this would indicate a very wide but shallow Drude profile, which would extend the profile far past the 1500-3000 Å range that was used to determine it. This indicates a misfit and is therefore rejected. Rejected Drude fits in this manner would automatically have the power law model be set as the more accurate model. If this test is passed, the second test is a reduced chi-square test for both the Drude profile and the power law model. The model with the lower value on this test was set to be the more accurate model.

The total number of 2175 Å detections per dust model is given in Table 3.2. As can be seen, not every spectrum has a 2175 Å feature, which is to be expected. However, some improvements can still be made to the filter. The SMC and `nodust` models both do not include PAH absorption, yet there are still some detections present. This implies that there is also overdetection taking place for the other models. These extra samples seem to have fairly high values for λ_i (see Figure 3.4), meaning they might be fitting part of the noise instead. This implies a better need to constrain λ_i in the future.

Treating the 2175 Å feature like an absorption line with a Drude profile for the line shape makes it possible to calculate equivalent widths (EWs) for each detection. The distribution of equivalent widths is shown in Figure 3.5. It is clearly visible here that the BARE-GR-S model predicts high equivalent widths, while the LMC model predicts lower values. This is unsurprising, since in Figure 2.2, it is shown that $\sigma_{\text{D,BARE-GR-S}} \gg \sigma_{\text{D,LMC}}$. The normalization of these models is different, however, so this comparison is not fully apt. The relative strength of the 2175 Å peak however is stronger for BARE-GR-S than for LMC, which may be the primary cause of the difference in distribution of the equivalent widths. The different approaches for the number density of dust by these two models make comparing the optical depths from these models less clear, but the difference in resulting equivalent widths show that the optical depth for BARE-GR-S is typically higher than that of LMC in the 2175 Å region. The EW values found by Obelisk are a closer match to LMC than to BARE-GR-S. which interestingly is not the case for the UV extinction curve (Figure 3.3), where BARE-GR-S is a closer match. This could be due to the shape of κ_D in Obelisk, with Obelisk having a steep curve in the UV continuum region, similar to that in σ_D in BARE-GR-S. The more complex dust distribution in Obelisk may also play a role

The `nodust` and SMC observations that mistakenly find a Drude profile only re-

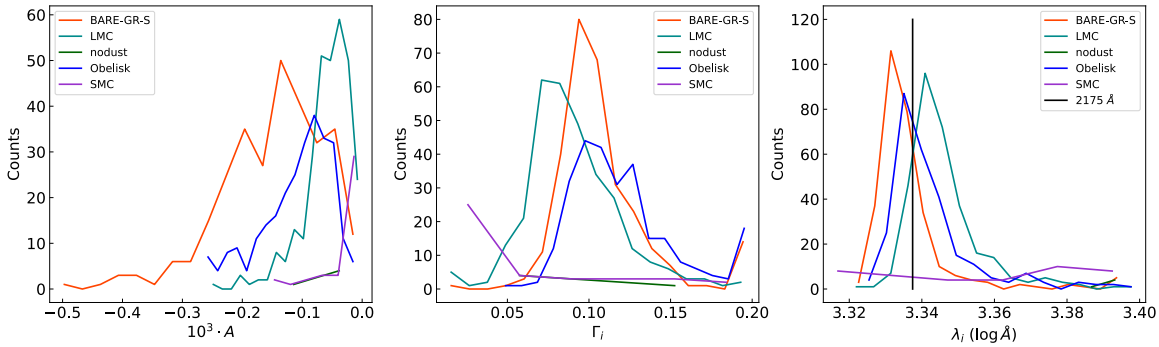

Figure 3.4: Distribution of fitted parameters for the PAH detected halos. Most fitted values of λ_i (which can be interpreted as the central wavelength of the profile) are well around $\log 2175$ Å (whose value is highlighted in the third plot), indeed predicting the 2175 Å feature correctly. The few `nodust` predictions all feature high λ_i (> 3.38), which could be seen as a need to constrain λ_i to lower values to avoid overdetections. What can also be seen is that the SMC features more detections with small Γ_i, which means this may be used to forecast false detections.

produce very low equivalent widths. This implies that some observations made by the other models with low equivalent widths may also be false positives. This is something that has to be taken into account for future discussions.

One motivation to add the Drude profile was to avoid possible contamination of the 2175 Å feature when measuring the UV continuum slope. The new model finds a new value for β_{UV}, that should be less influenced by the PAH absorption features. A comparison of $\beta_{\mathrm{UV,pl}}$ and $\beta_{\mathrm{UV,Drude}}$ can be seen in Figure 3.6 for the Obelisk, LMC, and BARE-GR-S models, which have the most detections. Overall, the UV continuum slope does not alter much when using either model. The Drude profile model measurement has a higher uncertainty, due to the higher number of parameters needed to be fit. This can be used as an explanation for the slight scatter in this relation. But overall, using the simpler power law model in this area does not heavily influence the slope of the UV continuum when compared to the Drude model on this wavelength range.

The Obelisk simulation combined with the spectra can be used to check to see if the equivalent width of the PAH absorption feature can be used as a tracer for any galaxy properties. This comparison for selected properties is shown in Figure 3.7. Visible here is that, roughly speaking, the Obelisk and LMC models match more closely than the BARE-GR-S model, both in distribution and possible correlation. One possibility is that the Obelisk model has similar values for the equivalent widths, and therefore does not sample the space as much as BARE-GR-S. What correlations are present in BARE-GR-S though, such as for the gas metallicity, are mostly absent from both Obelisk and

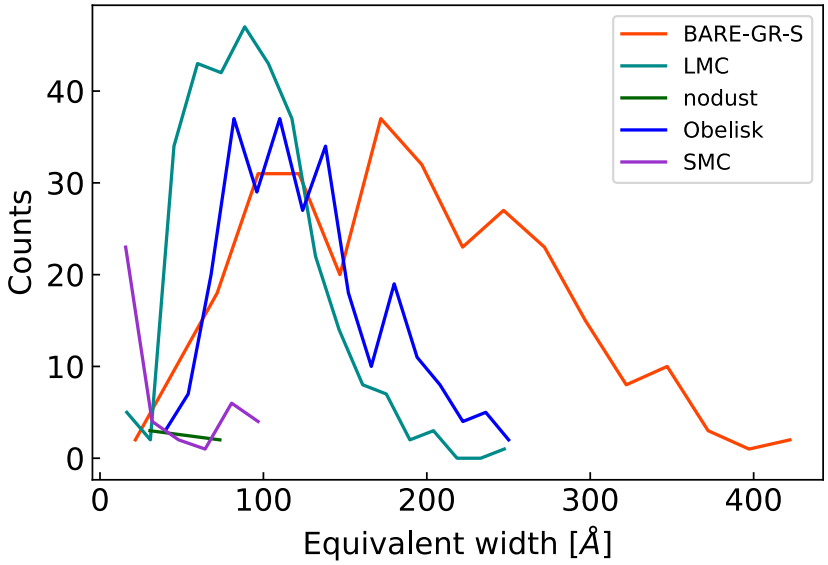

Figure 3.5: Equivalent width distribution per dust model for PAH absorption detected halos. Notable is that BARE-GR-S predicts higher equivalent widths than other models. SMC and `nodust` both predict low equivalent widths, which can be used as an indicator for a false detection. Obelisk predicts slightly higher equivalent widths than LMC, but does not have the broad lines as predicted by BARE-GR-S.

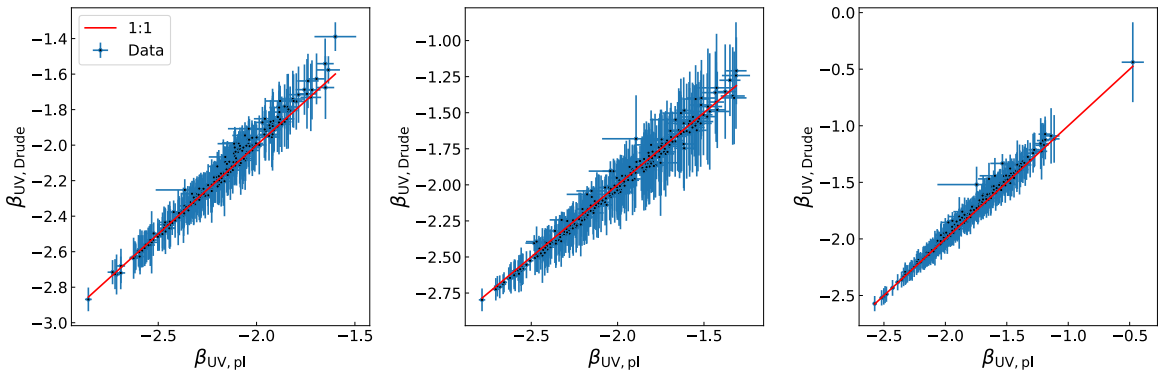

Figure 3.6: Comparison of $\beta_{\mathrm{UV,pl}}$ and $\beta_{\mathrm{UV,Drude}}$. Left: Obelisk dust model. Middle: LMC dust model. Right: BARE-GR-S dust model. The two methods of measuring β_{UV} do not show any statistically systematic difference. The Drude model finds slightly shallower values, but remains within 1σ of the power law model in almost all cases.

LMC. For the attenuation at 1500 Å, A_{1500} as shown in Figure 3.7, there seems to be a relation with the equivalent widths for all 3 models, however with very different shapes. This could be due to the difference in equivalent widths. There is significant overlap between the Obelisk model and the LMC model, with a relatively high scatter on a seemingly linear relationship between equivalent width and A_{1500}. BARE-GR-S has less scatter, and due to this model producing wider EWs, the relation is explored at higher EWs, where the scatter increases. BARE-GR-S also shows hints of evidence of correlation between EW and $M_{\rm dust}$ and $Z_{\rm gas}$. These relations have a significant amount of scatter, but a trend is visible that is not visible in Obelisk or LMC. The different distribution of equivalent widths may contribute to the lack of trend in Obelisk and LMC, where the scatter could overwhelm any possible trend. The magnitude at 1500 Å, M_{1500}, shows no significant trend with equivalent widths for any model, and neither is there a trend between EW and $t_{\rm star}$ or M_h. The trend of A_{1500} with equivalent width may be explained by very wide absorption lines reaching the 1500 Å region. Both EW and A_{1500} are measurements of dust attenuation, so they also may inherently be correlated. As for the trends visible in BARE-GR-S, the small trends can be explained by dust absorption being stronger with high metallicity or high dust mass.

3.4 Escape fractions

The escape fraction of ionizing photons is the fraction of ionizing photons that escape a galaxy into the CGM or IGM. This fraction is crucial to understanding the speed of reionization, with the source of the ionizing photons that drive reionization still being debated. However, this parameter is very unconstrained and difficult to measure. The ionizing escape fraction is determined by the spatial distribution of gas and dust around the sources of ionizing photons. Neutral hydrogen is the dominant absorber, with helium and dust playing a minor role. Since this parameter is hard to measure directly, more research on this topic is needed. Rascas can recreate this effect by propagating photons from their sources and tracking which photons are absorbed by gas and dust. During a Rascas run, all photon packets are flagged with their end state, either being absorbed or escaped. This allows us to easily calculate the escape fraction for the whole halo:

$$f_{\rm esc} = \frac{N_{\rm esc}}{N_{\rm tot}} = \frac{\int_{\lambda_1}^{\lambda_2} F_{\lambda,\rm esc} \lambda {\rm d}\lambda}{\int_{\lambda_1}^{\lambda_2} F_{\lambda,\rm tot} \lambda {\rm d}\lambda}. \tag{3.3}$$

For any individual viewing directions, $F_{\lambda,\rm esc}$ is the spectrum as found by Rascas, while $F_{\lambda,\rm tot}$ is found from the intrinsic spectrum of the whole halo before absorption. In this thesis, I make a distinction between $f_{\rm esc}$ and $f_{\rm esc,900}$, which are the escape fraction on the ionizing spectrum (200-911.5 Å, explicitly avoiding the Lyman break at 911.6 Å) and the escape fraction around rest-frame 900 Å using a 10 Å window. This is to align results with those found from observations, which typically calculate the ionizing escape fraction around this wavelength (e.g. Deharveng et al., 2001, Chisholm et al., 2018,

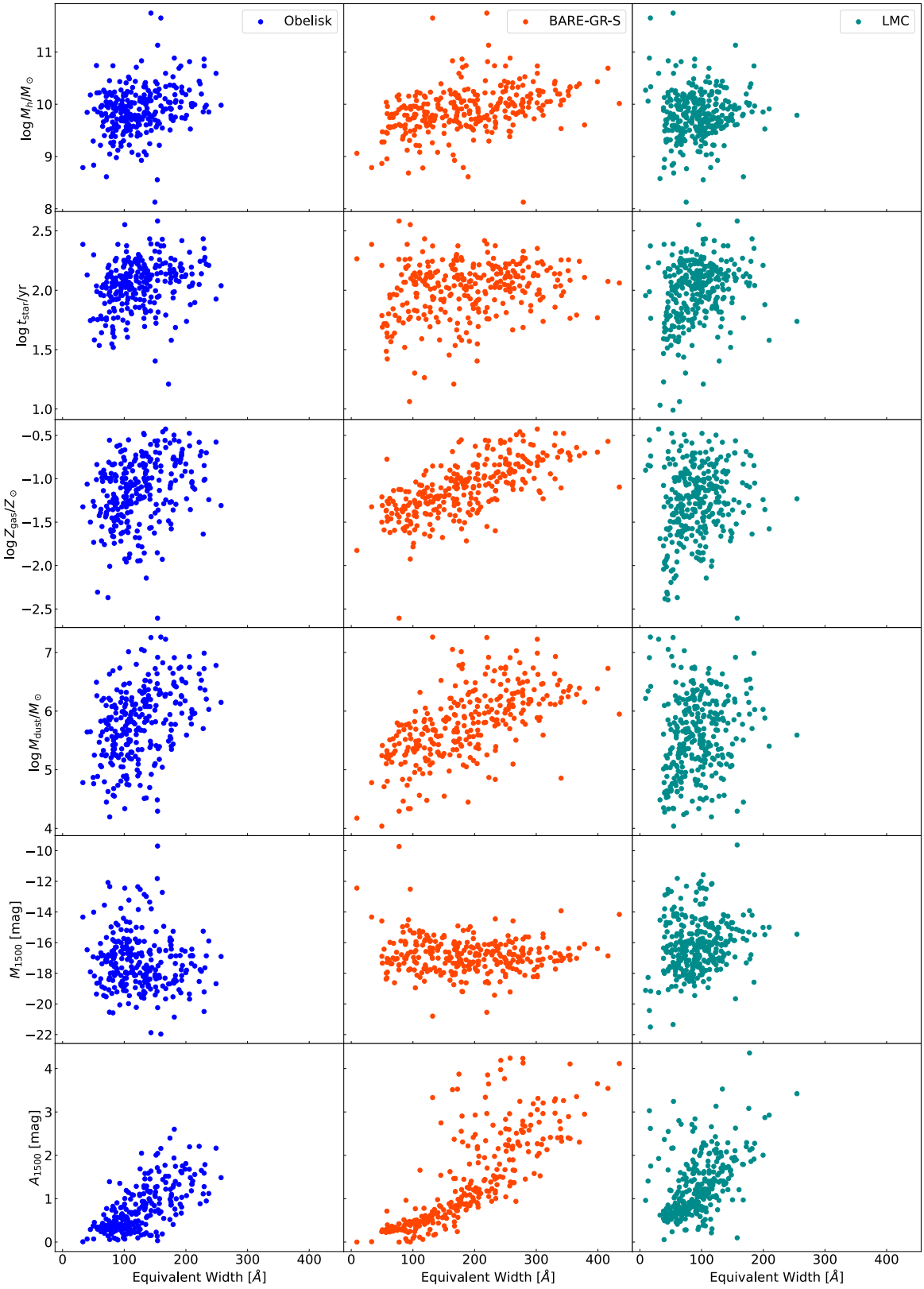

Figure 3.7: Comparison of 2175 Å feature equivalent widths to galaxy properties: *Left:* Obelisk. *Middle:* BARE-GR-S. *Right:* LMC. From top to bottom: Halo mass, mass-weighted mean stellar age, halo gas metallicity, halo dust mass, M_{1500}, and A_{1500}. BARE-GR-S shows correlation between equivalent width and A_{1500}, while other weaker relations are also visible for the dust models.

Izotov et al., 2021). This is also done for relative escape fraction methods, which use the ratio of fluxes at 900 Å and 1500 Å to find the relative escape fraction (e.g. Steidel et al., 2001, Boutsia et al., 2011, Grazian et al., 2017). The distribution of escape fractions is shown in Figure 3.8 for the angle-averaged escape fraction, and Figure 3.9 for the single-direction escape fraction. One thing to note is that any $\log f_{\rm esc} < -5$ should be regarded as being biased. This is due to using a total number of photon packets of $N_{\rm phot} = 500000$, which introduces a sampling bias in low-$f_{\rm esc}$ values. These escape fractions are therefore set equal to zero. The total number of escape fractions detected using this method per dust model is shown in Table 3.3. Notable is that the number of detections using $f_{\rm esc,900}$ is lower than that of $f_{\rm esc}$. This may indicate that UV continuum photons with shorter wavelengths also leak from the halo, increasing the escape fraction and creating more detections.

Figures 3.8 & 3.9 show that overall, the `nodust` model has the highest escape fractions. This is to be expected, as the dust absorption is zero by construction. What is also visible is that the BARE-GR-S model has lower values both for $f_{\rm esc}$ and $f_{\rm esc,900}$. The low $f_{\rm esc}$ can be explained by the BARE-GR-S absorption curve only being defined from wavelengths longer than 500 Å. The use of the flat curve for σ_D is most likely overestimating dust absorption at shorter wavelengths, decreasing $f_{\rm esc}$. This is not certain, since for $f_{\rm esc,900}$ this reasoning does not hold, since the calculation does not include the wavelength range below 500 Å, but BARE-GR-S still produces lower escape fractions than other models. This means that the BARE-GR-S model systematically predicts lower escape fractions than other models. LMC, SMC, and Obelisk all predict similar escape fractions. LMC and SMC both have the same dust density, so their difference is up to their different σ_D. Both of these models have low absorption in the ionizing part of the spectrum, which explains why they are not very different from `nodust`. Obelisk is mostly in line with LMC and SMC when comparing escape fractions, having slightly lower escape fractions than either of those models, but not as much as BARE-GR-S. This could be due to the similar construction of κ_D as for σ_D of LMC and SMC. In §3.3, it is shown that Obelisk predicts similar values as LMC for the continuum dust properties, pointing to similarities in the dust content between these models. The similarities in the escape fractions support that result. The `nodust` model predicts the highest escape fractions by construction, since there is no dust to absorb photons in this model. Since Obelisk and `nodust`, as well as LMC and SMC, are all similarly distributed, the dust content only moderately alters the escape fraction.

Notable is the large discrepancy in distributions between single-direction escape fractions and whole-halo escape fractions. The full halo escape fractions are much higher than those for single directions. This highlights the directionality that is inherent in the escape fraction. A single halo may have many directions with a low escape fraction, but the small number of directions with a high escape fraction leak a lot of photons, bringing the overall escape fraction of the full halo up. This is similar to the covering fraction (or 'picket-fence') approach (e.g. Reddy et al., 2016, Reddy et al., 2022, Gazagnes et al., 2020), which assumes that a galaxy is partially covered in an opaque HI cover. More evidence for this directionality can be seen from the similarities between

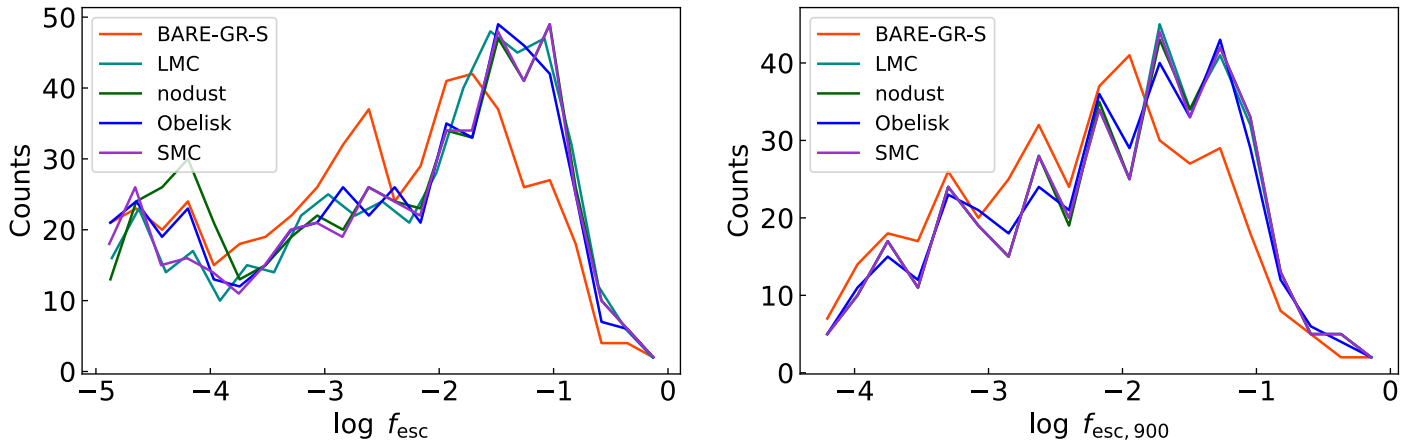

Figure 3.8: Angle-averaged escape fraction distribution for each dust model. *Left:* Ionizing escape fraction. *Right:* Escape fraction around 900 Å. The LMC, SMC, Obelisk, and `nodust` values overlap for $f_{esc,900}$, while BARE-GR-S predicts lower escape fractions than any of the other models.

Dust model	Obelisk	LMC	SMC	BARE-GR-S	`nodust`	Total
$N_{f_{esc},full}$	508	483	496	511	524	549
$N_{f_{esc,900},full}$	384	385	385	382	385	549
$N_{f_{esc},directional}$	5297	5022	5166	5290	5338	6648
$N_{f_{esc,900},directional}$	3138	3038	3004	3308	2973	6648

Table 3.3: Number of detected escape fractions ($\log f_{esc} > -5$) per dust model. "Full" denotes measurements across the whole halo, and "directional" along a single line of sight. The escape fraction around 900 Å features fewer detections than the entire ionizing spectrum. Since UV absorption is wavelength-dependent, there may be photons leaking at shorter wavelengths than 900 Å.

Figures 3.8 and 3.10, where the distribution of the maximum escape fraction along the 12 viewing directions for a single halo is shown. This distribution replicates the shape of the full halo distribution much better than the single-direction distribution. This suggests that the escape fraction of the full halo is dominated by a small number of directions with high escape fractions.

One of the main issues with capturing the LyC escape fraction is that it is hard to measure directly in the EoR due to the absorption of LyC photons by the neutral continuum. Many studies (e.g. Izotov et al., 2018, Mauerhofer et al., 2021, Katz et al., 2022a, Choustikov et al., 2023, Flury et al., 2022b) have tried to find a correlation between the escape fraction and other observables of a galaxy, but no definitive method has been found so far. This includes looking at correlations between emission lines and

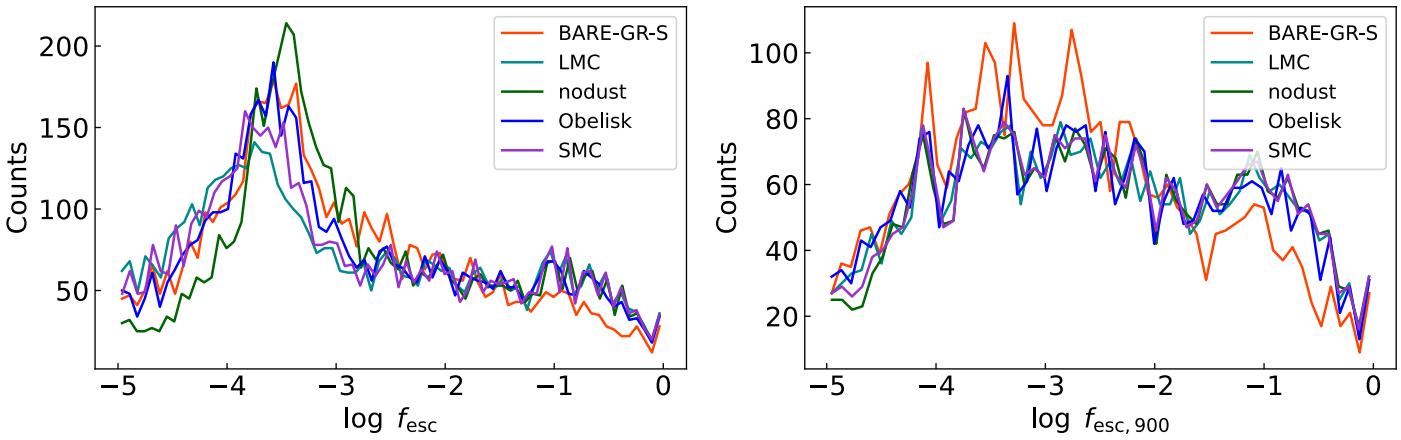

Figure 3.9: Single-direction escape fraction distribution for each dust model, using 12 directions per halo. *Left:* Ionizing escape fraction. *Right:* Escape fraction around 900 Å. This distribution is very different from the angle-averaged distribution, with a notable peak between $-4 < \log f_{esc} < -3$. BARE-GR-S predicts lower escape fractions than the other models. At the lower end, the `nodust` model predicts the highest escape fractions, with Obelisk, SMC, and LMC lagging behind.

LyC absorption, or for properties of a halo. In Figure 3.11, a few galaxy properties are selected to observe whether they are correlated with either f_{esc} or $f_{esc,900}$. As shown, no clear correlation between any suggested property is found for all dust models. The distributions also show no clear difference between dust models. Only a slight positive trend with very large scatter between the escape fraction and the metallicity is visible, but this is too broad of a scatter to be of any practical use. This evidence only furthers the trend of the escape fraction being a hard quantity to model from indirect measurements.

3.4.1 Dual-screen model

For radiation with wavelengths shorter than 911.6 Å, absorption can take place using hydrogen gas, using helium gas, and using dust. Hydrogen is the dominant absorption mechanism on these ionizing wavelengths with dust and helium being of less importance. One model of capturing this behaviour is by splitting the escape fraction into individual escape fractions for both absorbers:

$$f_{esc} = f_{esc,dust} f_{esc,gas}. \tag{3.4}$$

This model uses a dual screen, one of dust, and one of gas. This is a simplification compared to more realistic models, which have different column densities of gas and dust, intertwined with each other. A model containing two sources of attenuation has implicitly been used by e.g. Grazian et al., 2017 and Steidel et al., 2018. To quantify $f_{esc,gas}$, the escape fraction using the `nodust` model is used. This model is absent of

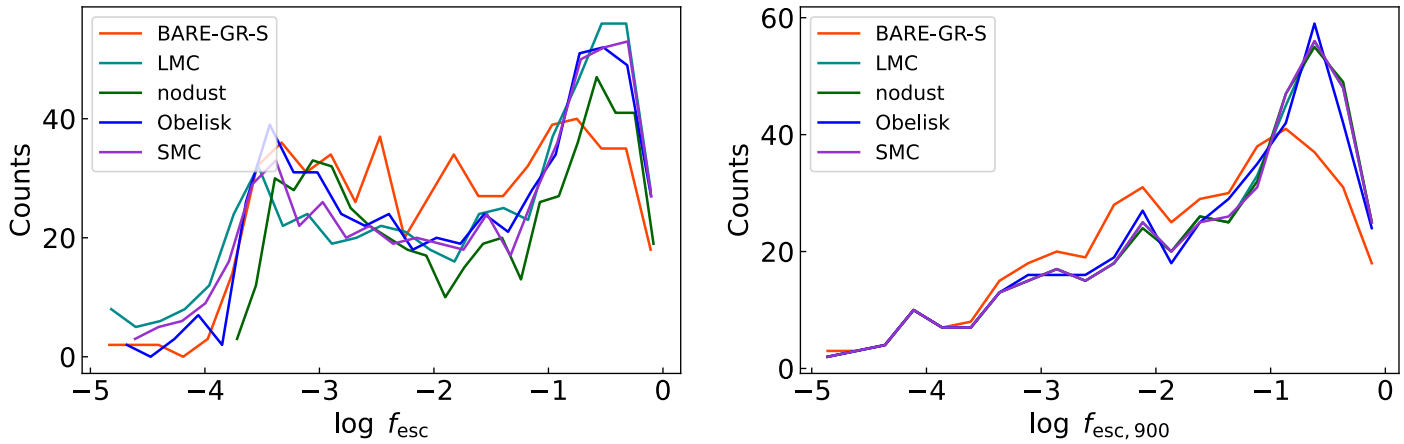

Figure 3.10: Distribution of the highest single-direction escape fraction of a single halo. *Left:* Ionizing escape fraction. *Right:* Escape fraction around 900 Å. BARE-GR-S predicts the lowest escape fractions. Notable is the more similar distribution to the angle-averaged distribution shown in Figure 3.8.

dust, so any absorption should take place via gas. Quantifying $f_{\mathrm{esc,dust}}$ is harder. To do this, a new run of RASCAS is done, which has gas removed. This run, coined `nogas`, uses the Obelisk dust model. These runs are only done on the ionizing spectrum, as the absorption by gas is not relevant for the UV continuum. From these new runs, the value $f_{\mathrm{esc,dust}}$ can be quantified using Equation 3.3 using the new spectrum. The f_{esc} found by multiplying $f_{\mathrm{esc,gas}}$ and $f_{\mathrm{esc,dust}}$ is compared to that of Obelisk in Figure 3.12. The new model does not overestimate any escape fraction as provided by Obelisk, but often the predicted escape fraction is lower than the escape fraction as found by Obelisk. Regions dense in both dust and gas absorb radiation efficiently for both screens, implying a low escape fraction for both screens. This is offset by low-density areas with high escape fractions for both gas and dust. Since a halo is made up of several sources, the escape fraction through one screen is calculated over all regions of the galaxy, both low density and high density. For a single halo using Obelisk, the escape fraction of dust and gas combined for these two regions looks like

$$f_{\mathrm{esc,Obelisk}} = \frac{f_{\mathrm{low,dust}} f_{\mathrm{low,gas}} + f_{\mathrm{high,dust}} f_{\mathrm{high,gas}}}{2}, \tag{3.5}$$

while for the dual-screen model this becomes

$$\begin{aligned} f_{\mathrm{esc,model}} &= \frac{f_{\mathrm{low,gas}} + f_{\mathrm{high,gas}}}{2} \frac{f_{\mathrm{low,dust}} + f_{\mathrm{high,dust}}}{2} \\ &= \frac{f_{\mathrm{low,dust}} f_{\mathrm{low,gas}} + f_{\mathrm{high,dust}} f_{\mathrm{high,gas}} + f_{\mathrm{low,dust}} f_{\mathrm{high,dust}} + f_{\mathrm{low,gas}} f_{\mathrm{high,gas}}}{4}. \end{aligned} \tag{3.6}$$

When $f_{\mathrm{low,dust}} f_{\mathrm{high,dust}} + f_{\mathrm{low,gas}} f_{\mathrm{high,gas}} < f_{\mathrm{low,dust}} f_{\mathrm{low,gas}} + f_{\mathrm{high,dust}} f_{\mathrm{high,gas}}$, the predicted escape fraction $f_{\mathrm{esc,model}} < f_{\mathrm{esc,Obelisk}}$. Obelisk predicts that the gas and dust densities

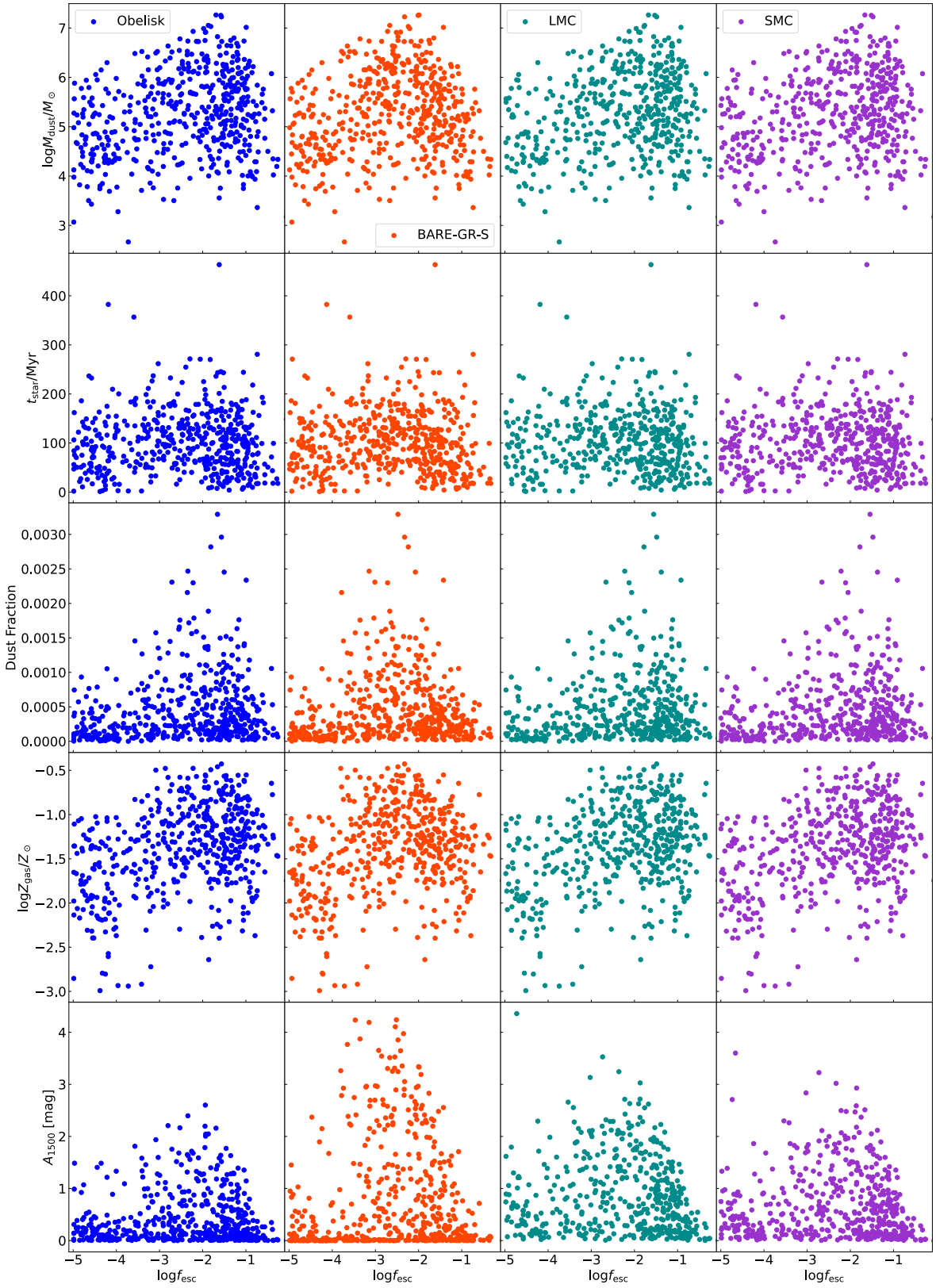

Figure 3.11: Comparison between escape fractions of multiple models with galaxy properties. Top to bottom: total dust mass, mass-weighted mean stellar age, dust mass fraction, metallicity, and attenuation. There seem to be no strong correlations with any parameter for any model.

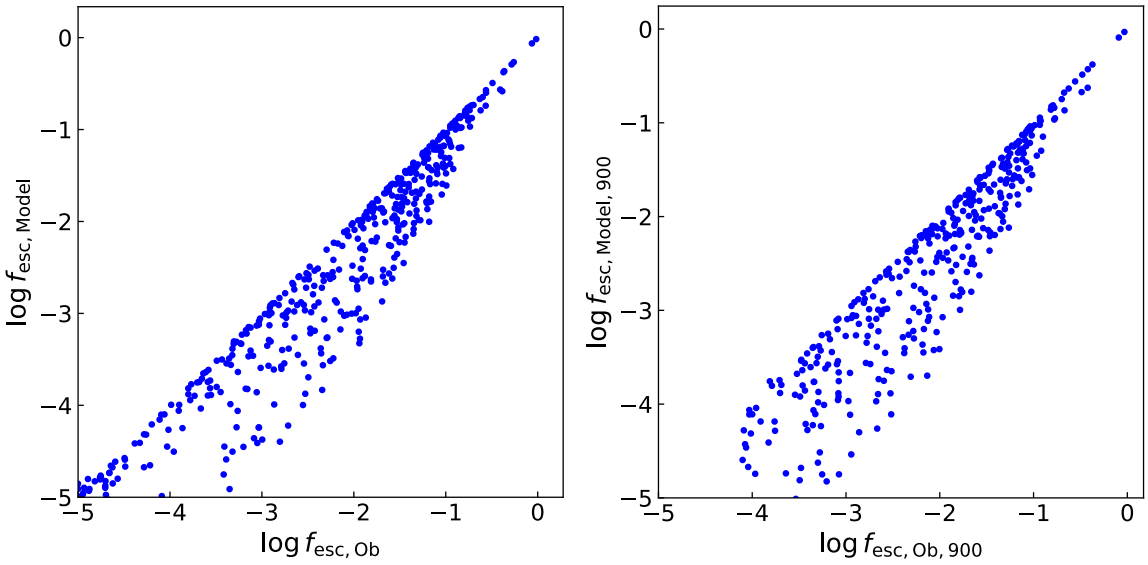

Figure 3.12: *Left:* Comparison of escape fractions from Obelisk as compared to dual-screen model predictions. *Right:* The same as left, but for $f_{\mathrm{esc},900}$. The dual-screen model predicts some values accurately, but typically produces underpredictions.

are correlated, so this effect is not uncommon. The more uniform the escape fractions are over a halo, the closer the dual-screen model will match the Obelisk value.

The dual-screen value does not overpredict values for Obelisk, as can be seen in Figure 3.12. Due to the lack of overpredictions, this dual-screen model may be used to give a lower limit for the real escape fraction as measured from Obelisk.

3.5 Infrared Emission

Dust is a primary driver of UV absorption in the Universe. This absorbed radiation heats up the dust, and is re-emitted in the infrared. Dust emission is one of the primary mechanisms in the infrared. Recent studies using ALMA (e.g. Dayal et al., 2022, Fudamoto et al., 2020, Shapley et al., 2023, Witstok et al., 2023a) targeting infrared emission at high z have provided observational constraints on dust properties in early galaxies. In this thesis, the infrared emission of a galaxy is modelled by assuming thermal equilibrium for dust, that is $L_{\mathrm{IR}} = L_{\mathrm{abs}}$, where L_{abs} is the energy absorbed by dust in the UV per second. This assumes that all IR luminosity is due to dust emission. Also, since Obelisk (or any other model in this analysis) does not include dust temperature estimates, no wavelength dependence for infrared emission is taken into account. L_{IR} is calculated as

$$L_{\mathrm{IR}} = L_{\mathrm{abs}} = \int F_{\lambda,\mathrm{abs}} \mathrm{d}\lambda. \tag{3.7}$$

$F_{\lambda,\mathrm{abs}}$ is calculated from the photon packets labelled as absorbed by dust. This selection can be used to quantify the dust absorption per wavelength, to form a "pseudo-spectrum" of dust absorption. From this pseudo-spectrum, the total amount of dust absorption can be calculated. This is done for the full wavelength range on which dust absorption exists for each halo.

The infrared excess-β_{UV} relation is a commonly used tool to estimate the dust attenuation. The infrared excess (IRX) is defined as $L_{\mathrm{IR}}/L_{\mathrm{UV}}$, commonly implemented as $L_{\mathrm{IR}}/(1600\text{Å}F_{\lambda}(1600\text{Å}))$ (e.g. Meurer et al., 1999, Fudamoto et al., 2020). This relation shows little evolution from redshifts 0-4 (e.g. Meurer et al., 1999, Overzier et al., 2011, Bouwens et al., 2016), but is less well studied at higher redshifts.

The general formula for the IRX-β_{UV} relation is given by (Fudamoto et al., 2020)

$$\mathrm{IRX} = BC_{\mathrm{UV}}\left(10^{0.4\frac{\mathrm{d}A_{\mathrm{FUV}}}{\mathrm{d}\beta_{\mathrm{UV}}}(\beta_{\mathrm{UV}}-\beta_0)} - 1\right). \tag{3.8}$$

The values for BC_{UV}, $\frac{\mathrm{d}A_{\mathrm{FUV}}}{\mathrm{d}\beta_{\mathrm{UV}}}$, and β_0 are calibrated on measured galaxies. β_0 stands for the unattenuated UV continuum slope for the entire population. The value BC_{UV} is a bolometric UV correction factor, and $\frac{\mathrm{d}A_{\mathrm{FUV}}}{\mathrm{d}\beta_{\mathrm{UV}}}$ is the change of FUV attenuation as a function of the UV continuum slope.

The IRX-β_{UV} relation for the different models of dust attenuation is shown in Figure 3.13, along with relations found by Meurer et al., 1999, Overzier et al., 2011 (both using $0 < z < 4$), and Fudamoto et al., 2020 (using $5 < z < 6$). The `nodust` model is excluded due to not having any dust absorption, and therefore no IR emission.

To compare the IRX-β_{UV} relation with those found in literature, I perform my own fit of Equation 3.8 on the measurements. This assumes $BC_{\mathrm{UV}} = 1.75$, like Fudamoto et al., 2020 and Bouwens et al., 2016. Resulting values for $\frac{\mathrm{d}A_{\mathrm{FUV}}}{\mathrm{d}\beta_{\mathrm{UV}}}$ and β_0 are shown in Table 3.4.

The steepness of the IRX-β_{UV} relation, or UV reddening slope, is denoted by $\frac{\mathrm{d}A_{\mathrm{FUV}}}{\mathrm{d}\beta_{\mathrm{UV}}}$. Meurer et al., 1999 find a value of 1.99 at low redshift, while Fudamoto et al., 2020 use a value of 1.1 for SMC-like curves, based on an approach by Reddy et al., 2018. The values found from the fits show a closer match to the Meurer et al., 1999 value, with the BARE-GR-S and LMC model laying above this relation. Ironically, the SMC dust model finds values closer to that of Meurer et al., 1999 than to the SMC-like curves of Fudamoto et al., 2020. The Obelisk value is more in agreement with that of the SMC models used by Fudamoto et al., 2020. This may indicate a difference in galaxy properties of early galaxies. However, values as low as those found by Fudamoto et al., 2020 of 0.48 ± 0.13 are not reached. This could be due to a lack of data present in Fudamoto et al., 2020, creating poorly constrained values for the IRX-β_{UV} relation. Another possibility is the difference in galaxy sample. The sample used in this thesis includes many low-mass galaxies, which cannot be detected at redshift 6. This may also introduce a bias in the shape of the IRX-β_{UV} relation. It is also possible that the simulations may simply systematically overpredict the amount of dust attenuation as compared to observations. Overall, the shape of the Obelisk curve much more closely

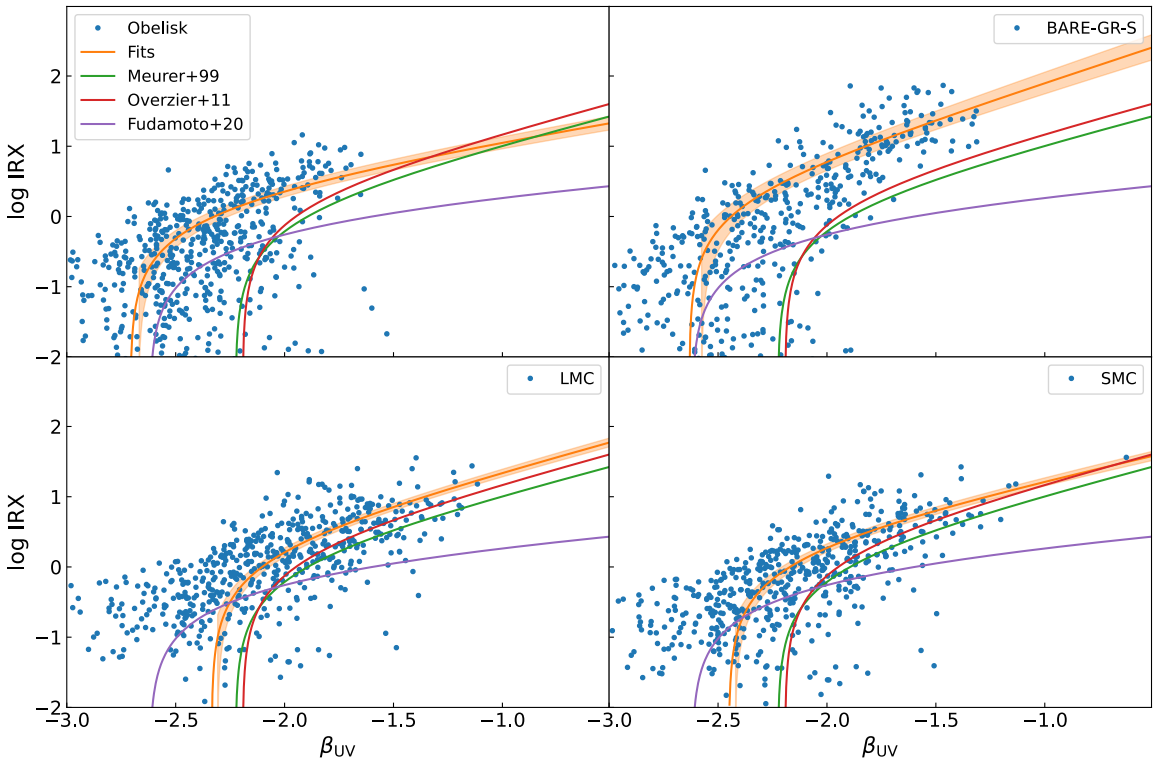

Figure 3.13: IRX-β_{UV} relation for several dust models. Shown are the measurements for each dust model, and the relations found by Meurer et al., 1999, Overzier et al., 2011, and Fudamoto et al., 2020. A curve based on parameters fitted to Equation 3.8 is shown too, along with its 1σ region.

Dust model	Obelisk	BARE-GR-S	LMC	SMC
$\frac{dA_{FUV}}{d\beta_{UV}}$	1.27 ± 0.08	2.55 ± 0.14	2.11 ± 0.05	1.75 ± 0.05
β_0	-2.71 ± 0.04	-2.63 ± 0.06	-2.33 ± 0.03	-2.45 ± 0.03

Table 3.4: Parameter values from fitting the IRX-β_{UV} relation to measurements in Obelisk.

matches that of Fudamoto et al., 2020 than the models at $0 < z < 4$, creating evidence of an evolution in the IRX-β_{UV} relation at higher redshifts.

Fudamoto et al., 2020 find no strong constraints on β_0, since their data are not complete enough. Their stacked approach leads to unconstrained fits. Meurer et al., 1999 find a value of $\beta_0 = -2.23$ for local galaxies, but this may not represent early galaxies. Reddy et al., 2018 find a bluer value of $\beta_0 = -2.62$ at $z \approx 2$ from the BPASS library, which is also used in Obelisk. This bluer value matches values found here better. Furthermore, the β_0 parameter specifies the UV continuum slope without attenuation. This is calculated in this thesis, in the form of the `nodust` model. Table 3.1 finds that $\langle \beta_{UV} \rangle = -2.55 \pm 0.25$, and all the fitted values for β_0 fall within 1σ of this. The bluer UV continuum slopes lead to a bluer cutoff of the IRX-β_{UV} relation, which is also recovered in the data. This could be due to differences between young galaxies and old galaxies.

One thing to note is that, where Fudamoto et al., 2020 find that their values lie below the Meurer et al., 1999 relation, here I find that many values lie above the Meurer et al., 1999 relation. The calculation of L_{IR} presented here neglects any absorption of IR radiation. Other sources besides dust emission of infrared emission are also neglected. So these systematics can be a reason for the overall higher IRX than expected, which then leads to mismatches with observed properties. Another issue is the difference in samples between this research and those observed by Fudamoto et al., 2020, with this sample containing many more low-mass galaxies.

3.5.1 Wavelength dependence

Modelling of the infrared emission by using thermal equilibrium is commonly done by assuming all absorption takes place in the UV continuum between the Lyman break at 911.6 Å and 4000 Å (e.g. Buat and Xu, 1996, Mauerhofer and Dayal, 2023). In my approach, a wider wavelength range is used that includes the rest-frame FUV and optical (200-10000 Å). This makes it possible to challenge this assumption of dust absorption in the continuum.

By integrating the dust absorption pseudo-spectrum on specific wavelength ranges, it is possible to deduct the wavelength-dependent absorption of UV radiation. This is done in 3 wavelength bins: [200-911.6 Å) for the ionizing spectrum in the FUV, [911.6-4000 Å) for the classic approach, and [4000-10000 Å] for the optical. This gives a fraction of radiation absorbed in each galaxy in each of these wavelength bins. This analysis does not include the `nodust` model due to the lack of dust absorption, and

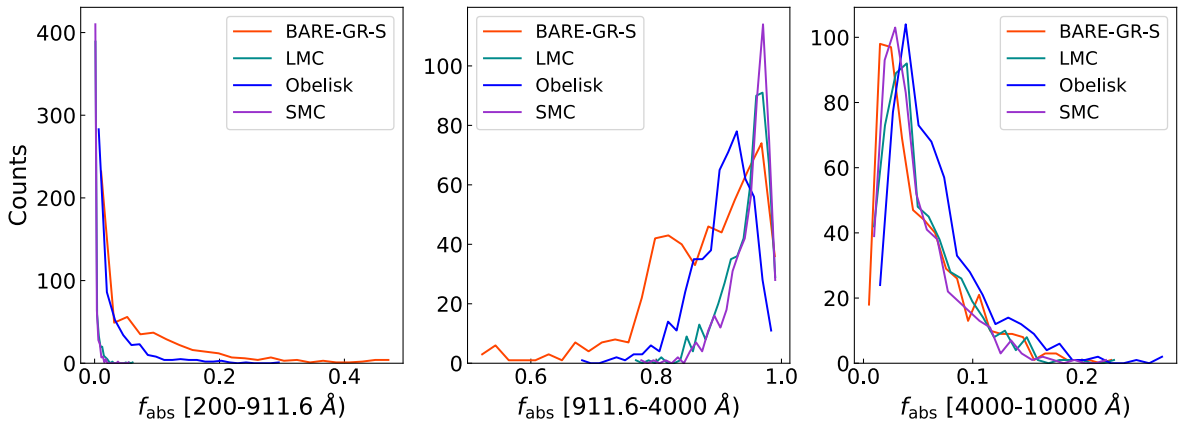

Figure 3.14: Distributions of absorption fractions of the 3 wavelength bins, for each dust model. Visible is that Obelisk and BARE-GR-S each have relatively low absorption in the 4000-10000 Å region, with LMC and SMC predicting nearly full absorption in this region. BARE-GR-S and Obelisk have higher absorption in the 911.6-4000 Å region than LMC and SMC, which are similar. Obelisk produces the highest amount of absorption in the 4000-10000 Å region.

therefore infrared emission, in this model. The distribution between these fractions is shown in Figure 3.14. As seen, the classic hypothesis is often true, with the [911.6-4000 Å) bin featuring by far the most absorbed energy. However, significant absorption may also take place in the further continuum, while the absorption in the ionizing region is also not negligible for the BARE-GR-S and Obelisk dust models. Obelisk shows the highest fraction of UV absorption in the long-wavelength bin, while overall BARE-GR-S has the lowest absorption in the classic [911.6-4000 Å) range. The high absorption of BARE-GR-S in the ionizing bin could be caused by this model having a flat σ_D curve at wavelengths shorter than 500 Å, artificially increasing absorption in this region. For the Obelisk and BARE-GR-S model, the median fraction of absorption in the [911.6-4000 Å) range is 0.89 and 0.91 respectively, while the other absorption is predominantly made up by the [4000-10000 Å] bin.

The distribution of absorption may change with galaxy properties, which is illustrated in Figure 3.15 for the Obelisk dust model. This shows that older, more evolved galaxies may have a higher fraction of radiation absorbed in the long wavelength continuum. Particularly the UV continuum slope seems to be strongly associated with these fractions, with redder slopes having a bigger fraction of absorption taking place in the 4000-10000 Å bin. One possible explanation for this is that for a redder UV continuum slope, this region has relatively more emission due to the flatter spectrum compared to the 911.6-4000 Å region. This higher intrinsic emission will also lead to more absorption in this wavelength region. It can therefore be beneficiary to include the optical region when modelling the total absorption of such a galaxy. For the ionizing absorption frac-

tion, there seems to be no clear correlation with these selected galaxy properties. The escape fraction fails to accurately capture any correlation, since only dust absorption is taken into account here. Including the gas absorption may give a correlation here, but the fickle nature of the escape fraction may complicate this analysis.

The wavelength dependence of UV absorption may be broken down even further. The pseudo-spectra of dust absorption can be directly integrated and normalized to create a cumulative distribution function (CDF) for each spectrum of dust absorption. These can be combined to form an overall CDF of the dust absorption per dust model. These are shown in Figure 3.16 for each dust model. Notable is the spike in absorption around the Lyman break at 911.6 Å, since at shorter wavelengths gas absorption is the dominant absorption mechanism. The higher values of BARE-GR-S and Obelisk in the ionizing sections indicate that there is more absorption in this region for both models.

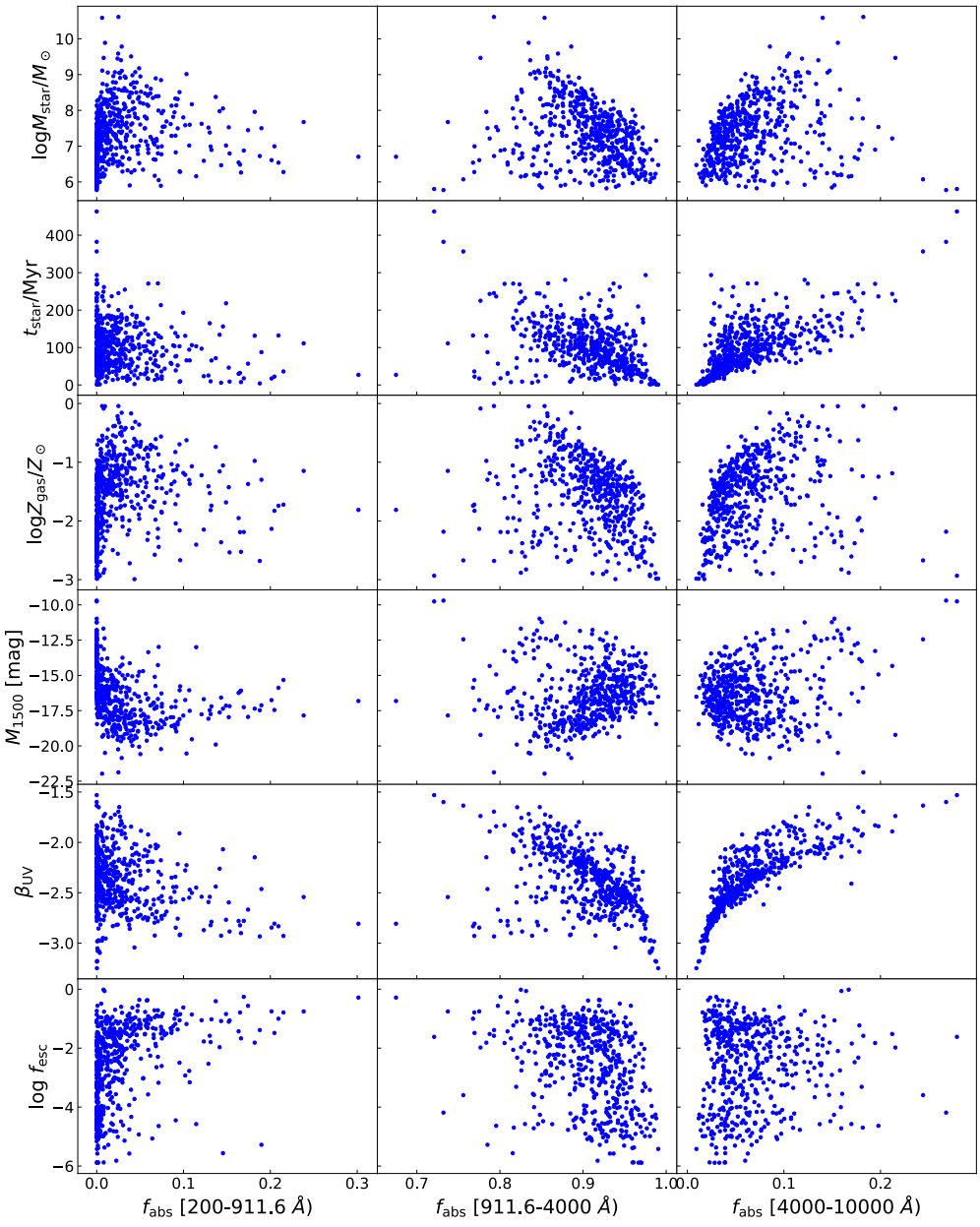

Figure 3.15: Comparison between energy absorption fraction and several galaxy properties for the Obelisk dust model (total stellar mass, mass-weighted mean stellar age, metallicity, magnitude at 1500 Å, UV continuum slope as calculated using the power-law model, and ionizing escape fraction). There seems to be little correlation between the ionizing section fraction and any of the highlighted properties here, while for wavelengths above 4000 Å there are some trends visible with metallicity, stellar mass, stellar age, and UV continuum slope.

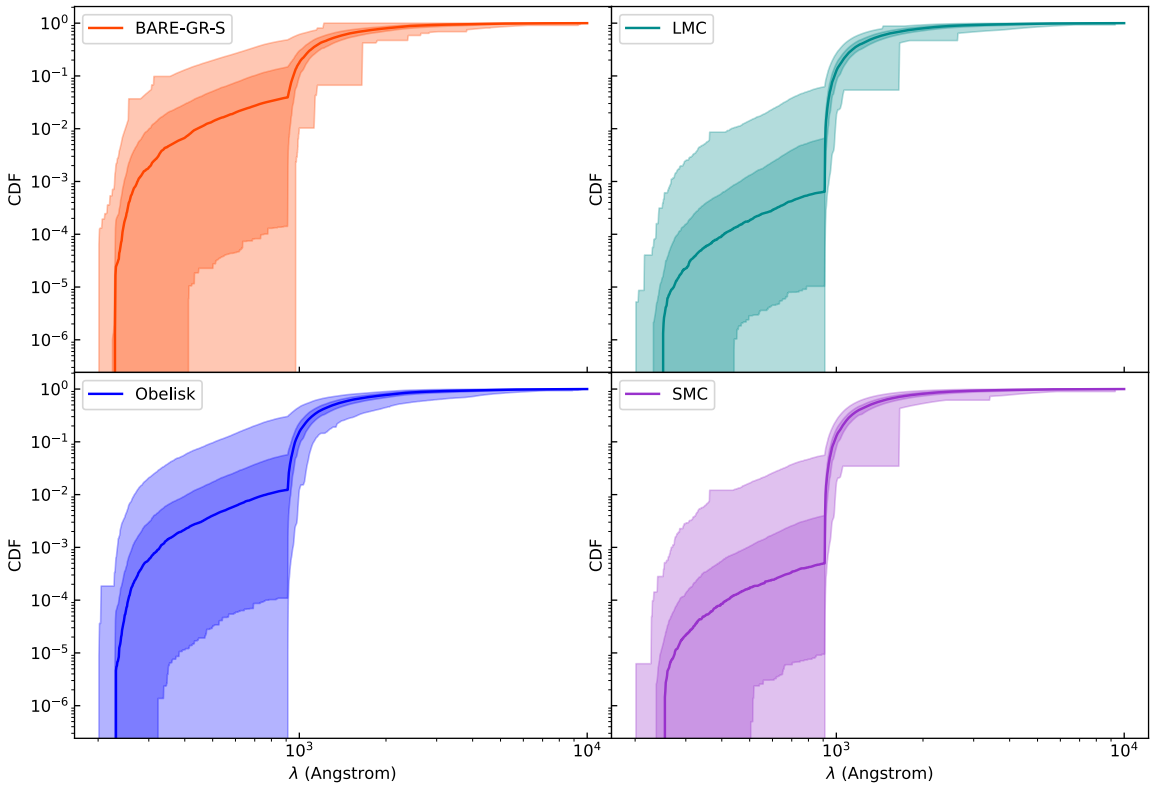

Figure 3.16: Cumulative distribution function of UV absorption by dust for several dust models, with 1σ and 3σ boundaries. Note that the 3σ boundary may have sampling bias effects. BARE-GR-S and Obelisk both feature high dust absorption below 911.6 Å, but all models show a steep increase in absorption at this wavelength due to gas absorption not taking place at higher wavelengths.

Chapter 4

Conclusion

In this thesis, I have laid out a method of generating mock spectra from the Obelisk hydrodynamical simulation using the Rascas code, at $z = 6$. This is done for 554 haloes in this simulation. Spectra are generated for 5 different models of dust attenuation, those being the BARE-GR-S, LMC, SMC, `nodust`, and the fiducial Obelisk model. The fiducial model is compared to these models on several observables that are extracted from the mock spectra.

Key results are:

- The UV continuum slopes are measured for each dust model. These serve as tracers of dust absorption, with flatter slopes featuring more absorption. Measured UV continuum slopes match up with literature values, besides the `nodust` model, which predicts steeper slopes due to the lack of dust present in this model.

- The UV continuum has a major absorption feature in the 2175 Å bump, created by PAHs. This feature is seen in the mock spectra too for the Obelisk, BARE-GR-S and LMC dust models. This might influence the measurement of the UV continuum slope. Assuming a Drude profile for this feature, it is found that the continuum slope with and without this feature are not statistically significantly different. The equivalent width of this feature is only weakly correlated with metallicity, but the correlation is stronger for A_{1500}. Equivalent widths for this feature of Obelisk most closely match the LMC model.

- The ionizing escape fraction is highly directional. By looking at spectra at different positions around a galaxy, it is found that the escape fraction of a full galaxy is often dominated by single directions with much higher escape fractions, while for most other directions, the escape fractions are much lower. This corroborates a model of photons streaming out of a galaxy through specific channels instead of from the whole halo. There seems to be no clear correlation between the whole halo escape fraction and any halo property included in this analysis. BARE-GR-S predicts the lowest escape fractions, possibly due to a flat absorption curve below 500 Å. The Obelisk escape fractions match those found by LMC more.

- A dual-screen model of calculating the escape fraction is compared to the direct value found from the Obelisk dust model. This model consists of a screen of gas and a separate screen of dust. This simplifies the geometry. Photons travel through each individually, in 2 separate runs, and their escape fractions are combined. The model has good correspondence with the Obelisk values, but sometimes may underpredict the escape fractions due to the possibility of an absorption of a photon packet in both runs. This approach therefore can be used to set a lower boundary on the escape fraction found using Obelisk. If this can be extended to simpler geometries, it may be a good tool for quick calculations of the escape fraction.

- UV radiation is absorbed by dust, and re-emitted in the infrared. This creates 2 measures of dust attenuation: IRX and the UV continuum slope. These are related using the IRX-β_{UV} relation. This relation does not change within redshift $0 < z < 4$, but at higher redshifts it may differ. For this galaxy sample, it is found that the measurements lie higher than the IRX-β_{UV} relation as proposed in literature. This may be due to imperfect IRX measurements. The found IRX-β_{UV} fitted to the observed data has a late cutoff due to the many steep UV continuum slopes, while the steepness of the relation is not consistent per dust model. More observations in this area are needed.

- UV photon absorption by dust is wavelength-dependent. Most of this absorption takes place between 911.6-4000 Å. Results show that, while absorption does indeed primarily take place in this wavelength region, absorption in the optical 4000-10000 Å range may contribute 10% or more to the overall UV absorption. At shorter wavelengths, this effect is much smaller due to neutral hydrogen being a more dominant absorber at these wavelengths. Galaxies with a more evolved, metal-rich population tend to have more absorption in the 4000-10000 Å range, with flat UV continuum slopes being the most important indicator for this. To study the IR properties of these galaxies, this wavelength range is worth including.

In the future, this research can be extended to include a better model of IR emission, since the current model only gives the total IR luminosity, with no wavelength dependence. From this, more advanced studies into the dust temperature and dust distribution can be done. The Drude profile model for studying the UV continuum slope as shown overpredicts the number of detections, which can be improved. Another possibility is to repeat this process for different redshifts, to track the evolution of dust over the history of the universe. Finally, with better observational constraints, new dust models can be created that may capture new processes such as the redshift evolution of dust properties. Furthermore, observations with experiments such as ALMA, JWST, SKA, and HERA will shed more light on the nature of galaxies in the EoR and the EoR as a whole.

Acknowledgements

This Master's Thesis could not have been made possible without the help of several people supporting my efforts.

First of all, I would like to thank Pratika Dayal, who as my first supervisor has helped guide this project to completion. Her comments and expertise have provided helpful feedback. I'm very thankful for her patience with me, and her encouragement and guidance along the way.

I will also thank Valentin Mauerhofer, my second supervisor. Our weekly discussions have helped me to keep going and helped break down this effort into manageable pieces, as well as setting goals for me to achieve every week. He has provided tremendous support related to Rascas, as well as any other questions I had.

Maxime Trebitsch has been a huge help to me as well, allowing me access to the Obelisk simulation, and being able to answer any question regarding it.

The other members of Pratika's research group, Chris, Paula, Fernanda, and Giorgos I thank for being there in the weekly meetings, providing good discussions of my results, as well as keeping me up to date with current events in the community.

Thanks to Lingyu Wang for taking the time to read this thesis as second examiner.

I thank everyone at the Kapteyn Institute for providing a healthy and comfortable environment to do this research, as well as the people with Sirius A and FMF for providing distractions from some of the hardship along the way.

Finally, I will thank my parents, Huib en Bente, and my sister, Dorte. They have been the best personal support I could ask for.

Bibliography

Adams, N. J., Conselice, C. J., Ferreira, L., Austin, D., Trussler, J. A. A., Juodžbalis, I., Wilkins, S. M., Caruana, J., Dayal, P., Verma, A., & Vijayan, A. P. (2023). Discovery and properties of ultra-high redshift galaxies ($9 < z < 12$) in the JWST ERO SMACS 0723 Field. MNRAS, *518*(3), 4755–4766. https://doi.org/10.1093/mnras/stac3347

Amiri, M., Bandura, K., Chen, T., Deng, M., Dobbs, M., Fandino, M., Foreman, S., Halpern, M., Hill, A. S., Hinshaw, G., Höfer, C., Kania, J., Landecker, T. L., MacEachern, J., Masui, K., Mena-Parra, J., Milutinovic, N., Mirhosseini, A., Newburgh, L., ... CHIME Collaboration. (2023). Detection of Cosmological 21 cm Emission with the Canadian Hydrogen Intensity Mapping Experiment. ApJ, *947*(1), Article 16, 16. https://doi.org/10.3847/1538-4357/acb13f

Atek, H., Shuntov, M., Furtak, L. J., Richard, J., Kneib, J.-P., Mahler, G., Zitrin, A., McCracken, H. J., Charlot, S., Chevallard, J., & Chemerynska, I. (2023). Revealing galaxy candidates out to $z \sim 16$ with JWST observations of the lensing cluster SMACS0723. MNRAS, *519*(1), 1201–1220. https://doi.org/10.1093/mnras/stac3144

Aubert, D., Pichon, C., & Colombi, S. (2004). The origin and implications of dark matter anisotropic cosmic infall on ~L_* haloes. MNRAS, *352*(2), 376–398. https://doi.org/10.1111/j.1365-2966.2004.07883.x

Bakx, T. J. L. C., Tamura, Y., Hashimoto, T., Inoue, A. K., Lee, M. M., Mawatari, K., Ota, K., Umehata, H., Zackrisson, E., Hatsukade, B., Kohno, K., Matsuda, Y., Matsuo, H., Okamoto, T., Shibuya, T., Shimizu, I., Taniguchi, Y., & Yoshida, N. (2020). ALMA uncovers the [C II] emission and warm dust continuum in a $z = 8.31$ Lyman break galaxy. MNRAS, *493*(3), 4294–4307. https://doi.org/10.1093/mnras/staa509

Bañados, E., Venemans, B. P., Mazzucchelli, C., Farina, E. P., Walter, F., Wang, F., Decarli, R., Stern, D., Fan, X., Davies, F. B., Hennawi, J. F., Simcoe, R. A., Turner, M. L., Rix, H.-W., Yang, J., Kelson, D. D., Rudie, G. C., & Winters, J. M. (2018). An 800-million-solar-mass black hole in a significantly neutral Universe at a redshift of 7.5. Nature, *553*(7689), 473–476. https://doi.org/10.1038/nature25180

Barrow, K. S. S., Robertson, B. E., Ellis, R. S., Nakajima, K., Saxena, A., Stark, D. P., & Tang, M. (2020). The Lyman Continuum Escape Survey: Connecting Time-

dependent [O III] and [O II] Line Emission with Lyman Continuum Escape Fraction in Simulations of Galaxy Formation. ApJ, *902*(2), Article L39, L39. https://doi.org/10.3847/2041-8213/abbd8e

Becker, R. H., Fan, X., White, R. L., Strauss, M. A., Narayanan, V. K., Lupton, R. H., Gunn, J. E., Annis, J., Bahcall, N. A., Brinkmann, J., Connolly, A. J., Csabai, I., Czarapata, P. C., Doi, M., Heckman, T. M., Hennessy, G. S., Ivezić, Ž., Knapp, G. R., Lamb, D. Q., ... York, D. G. (2001). Evidence for Reionization at z~6: Detection of a Gunn-Peterson Trough in a z=6.28 Quasar. AJ, *122*(6), 2850–2857. https://doi.org/10.1086/324231

Beckwith, S. V. W., Stiavelli, M., Koekemoer, A. M., Caldwell, J. A. R., Ferguson, H. C., Hook, R., Lucas, R. A., Bergeron, L. E., Corbin, M., Jogee, S., Panagia, N., Robberto, M., Royle, P., Somerville, R. S., & Sosey, M. (2006). The Hubble Ultra Deep Field. AJ, *132*(5), 1729–1755. https://doi.org/10.1086/507302

Bhatawdekar, R., & Conselice, C. J. (2021). UV Spectral Slopes at z = 6-9 in the Hubble Frontier Fields: Lack of Evidence for Unusual or Population III Stellar Populations. ApJ, *909*(2), Article 144, 144. https://doi.org/10.3847/1538-4357/abdd3f

Bianchi, S., & Schneider, R. (2007). Dust formation and survival in supernova ejecta. MNRAS, *378*(3), 973–982. https://doi.org/10.1111/j.1365-2966.2007.11829.x

Bolton, J. S., Caputo, A., Liu, H., & Viel, M. (2022). Comparison of Low-Redshift Lyman-α Forest Observations to Hydrodynamical Simulations with Dark Photon Dark Matter. Phys. Rev. Lett., *129*(21), Article 211102, 211102. https://doi.org/10.1103/PhysRevLett.129.211102

Boutsia, K., Grazian, A., Giallongo, E., Fontana, A., Pentericci, L., Castellano, M., Zamorani, G., Mignoli, M., Vanzella, E., Fiore, F., Lilly, S. J., Gallozzi, S., Testa, V., Paris, D., & Santini, P. (2011). A Low Escape Fraction of Ionizing Photons of L > L* Lyman Break Galaxies at z = 3.3. ApJ, *736*(1), Article 41, 41. https://doi.org/10.1088/0004-637X/736/1/41

Bouwens, R. J., Bradley, L., Zitrin, A., Coe, D., Franx, M., Zheng, W., Smit, R., Host, O., Postman, M., Moustakas, L., Labbé, I., Carrasco, M., Molino, A., Donahue, M., Kelson, D. D., Meneghetti, M., Benítez, N., Lemze, D., Umetsu, K., ... Seitz, S. (2014). A Census of Star-forming Galaxies in the Z ~9-10 Universe based on HST+Spitzer Observations over 19 Clash Clusters: Three Candidate Z ~9-10 Galaxies and Improved Constraints on the Star Formation Rate Density at Z ~9.2. ApJ, *795*(2), Article 126, 126. https://doi.org/10.1088/0004-637X/795/2/126

Bouwens, R. J., Smit, R., Schouws, S., Stefanon, M., Bowler, R., Endsley, R., Gonzalez, V., Inami, H., Stark, D., Oesch, P., Hodge, J., Aravena, M., da Cunha, E., Dayal, P., de Looze, I., Ferrara, A., Fudamoto, Y., Graziani, L., Li, C., ... Witstok, J. (2022). Reionization Era Bright Emission Line Survey: Selection and Characterization of Luminous Interstellar Medium Reservoirs in the z > 6.5 Universe. ApJ, *931*(2), Article 160, 160. https://doi.org/10.3847/1538-4357/ac5a4a

Bouwens, R. J., Aravena, M., Decarli, R., Walter, F., da Cunha, E., Labbé, I., Bauer, F. E., Bertoldi, F., Carilli, C., Chapman, S., Daddi, E., Hodge, J., Ivison, R. J., Karim, A., Le Fevre, O., Magnelli, B., Ota, K., Riechers, D., Smail, I. R., ... Wilkins, S. (2016). ALMA Spectroscopic Survey in the Hubble Ultra Deep Field: The Infrared Excess of UV-Selected z = 2-10 Galaxies as a Function of UV-Continuum Slope and Stellar Mass. ApJ, *833*(1), Article 72, 72. https://doi.org/10.3847/1538-4357/833/1/72

Bouwens, R. J., Stefanon, M., Brammer, G., Oesch, P. A., Herard-Demanche, T., Illingworth, G. D., Matthee, J., Naidu, R. P., van Dokkum, P. G., & van Leeuwen, I. F. (2023). Evolution of the UV LF from z $\sim$ 15 to z $\sim$ 8 using new JWST NIRCam medium-band observations over the HUDF/XDF. MNRAS, *523*(1), 1036–1055. https://doi.org/10.1093/mnras/stad1145

Bowman, J. D., Rogers, A. E. E., Monsalve, R. A., Mozdzen, T. J., & Mahesh, N. (2018). An absorption profile centred at 78 megahertz in the sky-averaged spectrum. Nature, *555*(7694), 67–70. https://doi.org/10.1038/nature25792

Boylan-Kolchin, M. (2023). Stress testing ΛCDM with high-redshift galaxy candidates. *Nature Astronomy*. https://doi.org/10.1038/s41550-023-01937-7

Bromm, V., & Loeb, A. (2003). The formation of the first low-mass stars from gas with low carbon and oxygen abundances. Nature, *425*(6960), 812–814. https://doi.org/10.1038/nature02071

Buat, V., & Xu, C. (1996). Star formation and dust extinction in disk galaxies. Comparison between the UV non-ionizing and the FIR emissions. A&A, *306*, 61.

Bull, P., Akrami, Y., Adamek, J., Baker, T., Bellini, E., Beltrán Jiménez, J., Bentivegna, E., Camera, S., Clesse, S., Davis, J. H., Di Dio, E., Enander, J., Heavens, A., Heisenberg, L., Hu, B., Llinares, C., Maartens, R., Mörtsell, E., Nadathur, S., ... Winther, H. A. (2016). Beyond Λ CDM: Problems, solutions, and the road ahead. *Physics of the Dark Universe*, *12*, 56–99. https://doi.org/10.1016/j.dark.2016.02.001

Bullock, J. S. (2010). Notes on the Missing Satellites Problem. *arXiv e-prints*, Article arXiv:1009.4505, arXiv:1009.4505. https://doi.org/10.48550/arXiv.1009.4505

Bunker, A. J., Saxena, A., Cameron, A. J., Willott, C. J., Curtis-Lake, E., Jakobsen, P., Carniani, S., Smit, R., Maiolino, R., Witstok, J., Curti, M., D'Eugenio, F., Jones, G. C., Ferruit, P., Arribas, S., Charlot, S., Chevallard, J., Giardino, G., de Graaff, A., ... Whitler, L. (2023). JADES NIRSpec Spectroscopy of GN-z11: Lyman-α emission and possible enhanced nitrogen abundance in a $z = 10.60$ luminous galaxy. *arXiv e-prints*, Article arXiv:2302.07256, arXiv:2302.07256. https://doi.org/10.48550/arXiv.2302.07256

Calzetti, D., Kinney, A. L., & Storchi-Bergmann, T. (1994). Dust Extinction of the Stellar Continua in Starburst Galaxies: The Ultraviolet and Optical Extinction Law. ApJ, *429*, 582. https://doi.org/10.1086/174346

Chantavat, T., Chongchitnan, S., & Silk, J. (2023). The most massive Population III stars. MNRAS, *522*(3), 3256–3262. https://doi.org/10.1093/mnras/stad1196

Chardin, J., Puchwein, E., & Haehnelt, M. G. (2017). Large-scale opacity fluctuations in the Lyα forest: evidence for QSOs dominating the ionizing UV background at z $\sim$ 5.5-6? MNRAS, *465*(3), 3429–3445. https://doi.org/10.1093/mnras/stw2943

Chen, Q., Meyer, M., Popping, A., Staveley-Smith, L., Bryant, J., Delhaize, J., Holwerda, B. W., Cluver, M. E., Loveday, J., Lopez-Sanchez, A. R., Zwaan, M., Taylor, E. N., Hopkins, A. M., Wright, A., Driver, S., & Brough, S. (2021). Measuring cosmic density of neutral hydrogen via stacking the DINGO-VLA data. MNRAS, *508*(2), 2758–2770. https://doi.org/10.1093/mnras/stab2810

Chisholm, J., Gazagnes, S., Schaerer, D., Verhamme, A., Rigby, J. R., Bayliss, M., Sharon, K., Gladders, M., & Dahle, H. (2018). Accurately predicting the escape fraction of ionizing photons using rest-frame ultraviolet absorption lines. A&A, *616*, Article A30, A30. https://doi.org/10.1051/0004-6361/201832758

Choi, Y., Dalcanton, J. J., Williams, B. F., Skillman, E. D., Fouesneau, M., Gordon, K. D., Sandstrom, K. M., Weisz, D. R., & Gilbert, K. M. (2020). Mapping the Escape Fraction of Ionizing Photons Using Resolved Stars: A Much Higher Escape Fraction for NGC 4214. ApJ, *902*(1), Article 54, 54. https://doi.org/10.3847/1538-4357/abb467

Choustikov, N., Katz, H., Saxena, A., Cameron, A. J., Devriendt, J., Slyz, A., Rosdahl, J., Blaizot, J., & Michel-Dansac, L. (2023). The Physics of Indirect Estimators of Lyman Continuum Escape and their Application to High-Redshift JWST Galaxies. *arXiv e-prints*, Article arXiv:2304.08526, arXiv:2304.08526. https://doi.org/10.48550/arXiv.2304.08526

Crain, R. A., Schaye, J., Bower, R. G., Furlong, M., Schaller, M., Theuns, T., Dalla Vecchia, C., Frenk, C. S., McCarthy, I. G., Helly, J. C., Jenkins, A., Rosas-Guevara, Y. M., White, S. D. M., & Trayford, J. W. (2015). The EAGLE simulations of galaxy formation: calibration of subgrid physics and model variations. MNRAS, *450*(2), 1937–1961. https://doi.org/10.1093/mnras/stv725

Cullen, F., McLure, R. J., McLeod, D. J., Dunlop, J. S., Donnan, C. T., Carnall, A. C., Bowler, R. A. A., Begley, R., Hamadouche, M. L., & Stanton, T. M. (2023). The ultraviolet continuum slopes (β) of galaxies at z $\simeq$ 8-16 from JWST and ground-based near-infrared imaging. MNRAS, *520*(1), 14–23. https://doi.org/10.1093/mnras/stad073

Curtis-Lake, E., Carniani, S., Cameron, A., Charlot, S., Jakobsen, P., Maiolino, R., Bunker, A., Witstok, J., Smit, R., Chevallard, J., Willott, C., Ferruit, P., Arribas, S., Bonaventura, N., Curti, M., D'Eugenio, F., Franx, M., Giardino, G., Looser, T. J., ... Whitler, L. (2023). Spectroscopic confirmation of four metal-poor galaxies at z = 10.3-13.2. *Nature Astronomy*, *7*, 622–632. https://doi.org/10.1038/s41550-023-01918-w

Cyburt, R. H., Fields, B. D., Olive, K. A., & Yeh, T.-H. (2016). Big bang nucleosynthesis: Present status. *Reviews of Modern Physics*, *88*(1), Article 015004, 015004. https://doi.org/10.1103/RevModPhys.88.015004

Dayal, P., Ferrara, A., Sommovigo, L., Bouwens, R., Oesch, P. A., Smit, R., Gonzalez, V., Schouws, S., Stefanon, M., Kobayashi, C., Bremer, J., Algera, H. S. B.,

Aravena, M., Bowler, R. A. A., da Cunha, E., Fudamoto, Y., Graziani, L., Hodge, J., Inami, H., ... Endsley, R. (2022). The ALMA REBELS survey: the dust content of z ∼ 7 Lyman break galaxies. MNRAS, *512*(1), 989–1002. https://doi.org/10.1093/mnras/stac537

Dayal, P., & Ferrara, A. (2018). Early galaxy formation and its large-scale effects. Phys. Rep., *780*, 1–64. https://doi.org/10.1016/j.physrep.2018.10.002

de Blok, W. J. G. (2010). The Core-Cusp Problem. *Advances in Astronomy*, *2010*, Article 789293, 789293. https://doi.org/10.1155/2010/789293

Deharveng, J. .-., Buat, V., Le Brun, V., Milliard, B., Kunth, D., Shull, J. M., & Gry, C. (2001). Constraints on the Lyman continuum radiation from galaxies: First results with FUSE on Mrk 54. A&A, *375*, 805–813. https://doi.org/10.1051/0004-6361:20010920

Dijkstra, M. (2014). Lyα Emitting Galaxies as a Probe of Reionisation. PASA, *31*, Article e040, e040. https://doi.org/10.1017/pasa.2014.33

Dijkstra, M. (2017). Saas-Fee Lecture Notes: Physics of Lyman Alpha Radiative Transfer. *arXiv e-prints*, Article arXiv:1704.03416, arXiv:1704.03416. https://doi.org/10.48550/arXiv.1704.03416

Draine, B. T. (2003). Interstellar Dust Grains. ARA&A, *41*, 241–289. https://doi.org/10.1146/annurev.astro.41.011802.094840

Draine, B. T., & Li, A. (2007). Infrared Emission from Interstellar Dust. IV. The Silicate-Graphite-PAH Model in the Post-Spitzer Era. ApJ, *657*(2), 810–837. https://doi.org/10.1086/511055

Dubois, Y., Pichon, C., Welker, C., Le Borgne, D., Devriendt, J., Laigle, C., Codis, S., Pogosyan, D., Arnouts, S., Benabed, K., Bertin, E., Blaizot, J., Bouchet, F., Cardoso, J. .-., Colombi, S., de Lapparent, V., Desjacques, V., Gavazzi, R., Kassin, S., ... Volonteri, M. (2014). Dancing in the dark: galactic properties trace spin swings along the cosmic web. MNRAS, *444*(2), 1453–1468. https://doi.org/10.1093/mnras/stu1227

Dwek, E., Arendt, R. G., Hauser, M. G., Fixsen, D., Kelsall, T., Leisawitz, D., Pei, Y. C., Wright, E. L., Mather, J. C., Moseley, S. H., Odegard, N., Shafer, R., Silverberg, R. F., & Weiland, J. L. (1998). The COBE Diffuse Infrared Background Experiment Search for the Cosmic Infrared Background. IV. Cosmological Implications. ApJ, *508*(1), 106–122. https://doi.org/10.1086/306382

Dwek, E. (1998). The Evolution of the Elemental Abundances in the Gas and Dust Phases of the Galaxy. ApJ, *501*, 643. https://doi.org/10.1086/305829

Eilers, A.-C., Davies, F. B., Hennawi, J. F., Prochaska, J. X., Lukić, Z., & Mazzucchelli, C. (2017). Implications of z ∼ 6 Quasar Proximity Zones for the Epoch of Reionization and Quasar Lifetimes. ApJ, *840*(1), Article 24, 24. https://doi.org/10.3847/1538-4357/aa6c60

Ferrara, A., Viti, S., & Ceccarelli, C. (2016). The problematic growth of dust in high-redshift galaxies. MNRAS, *463*(1), L112–L116. https://doi.org/10.1093/mnrasl/slw165

Ferrara, A., Pallottini, A., & Dayal, P. (2023). On the stunning abundance of super-early, luminous galaxies revealed by JWST. MNRAS, *522*(3), 3986–3991. https://doi.org/10.1093/mnras/stad1095

Ferrarotti, A. S., & Gail, H. .-. (2006). Composition and quantities of dust produced by AGB-stars and returned to the interstellar medium. A&A, *447*(2), 553–576. https://doi.org/10.1051/0004-6361:20041198

Finkelstein, S. L., Bagley, M., Song, M., Larson, R., Papovich, C., Dickinson, M., Finkelstein, K. D., Koekemoer, A. M., Pirzkal, N., Somerville, R. S., Yung, L. Y. A., Behroozi, P., Ferguson, H., Giavalisco, M., Grogin, N., Hathi, N., Hutchison, T. A., Jung, I., Kocevski, D., ... Tacchella, S. (2022). A Census of the Bright z = 8.5-11 Universe with the Hubble and Spitzer Space Telescopes in the CANDELS Fields. ApJ, *928*(1), Article 52, 52. https://doi.org/10.3847/1538-4357/ac3aed

Finkelstein, S. L., Bagley, M. B., Ferguson, H. C., Wilkins, S. M., Kartaltepe, J. S., Papovich, C., Yung, L. Y. A., Haro, P. A., Behroozi, P., Dickinson, M., Kocevski, D. D., Koekemoer, A. M., Larson, R. L., Le Bail, A., Morales, A. M., Pérez-González, P. G., Burgarella, D., Davé, R., Hirschmann, M., ... Zavala, J. A. (2023). CEERS Key Paper. I. An Early Look into the First 500 Myr of Galaxy Formation with JWST. ApJ, *946*(1), Article L13, L13. https://doi.org/10.3847/2041-8213/acade4

Flury, S. R., Jaskot, A. E., Ferguson, H. C., Worseck, G., Makan, K., Chisholm, J., Saldana-Lopez, A., Schaerer, D., McCandliss, S., Wang, B., Ford, N. M., Heckman, T., Ji, Z., Giavalisco, M., Amorin, R., Atek, H., Blaizot, J., Borthakur, S., Carr, C., ... Xu, X. (2022a). The Low-redshift Lyman Continuum Survey. I. New, Diverse Local Lyman Continuum Emitters. ApJS, *260*(1), Article 1, 1. https://doi.org/10.3847/1538-4365/ac5331

Flury, S. R., Jaskot, A. E., Ferguson, H. C., Worseck, G., Makan, K., Chisholm, J., Saldana-Lopez, A., Schaerer, D., McCandliss, S. R., Xu, X., Wang, B., Oey, M. S., Ford, N. M., Heckman, T., Ji, Z., Giavalisco, M., Amorín, R., Atek, H., Blaizot, J., ... Verhamme, A. (2022b). The Low-redshift Lyman Continuum Survey. II. New Insights into LyC Diagnostics. ApJ, *930*(2), Article 126, 126. https://doi.org/10.3847/1538-4357/ac61e4

Fudamoto, Y., Oesch, P. A., Faisst, A., Béthermin, M., Ginolfi, M., Khusanova, Y., Loiacono, F., Le Fèvre, O., Capak, P., Schaerer, D., Silverman, J. D., Cassata, P., Yan, L., Amorin, R., Bardelli, S., Boquien, M., Cimatti, A., Dessauges-Zavadsky, M., Fujimoto, S., ... Zucca, E. (2020). The ALPINE-ALMA [CII] survey. Dust attenuation properties and obscured star formation at z ∼ 4.4-5.8. A&A, *643*, Article A4, A4. https://doi.org/10.1051/0004-6361/202038163

Gazagnes, S., Chisholm, J., Schaerer, D., Verhamme, A., & Izotov, Y. (2020). The origin of the escape of Lyman α and ionizing photons in Lyman continuum emitters. A&A, *639*, Article A85, A85. https://doi.org/10.1051/0004-6361/202038096

Gnedin, N. Y., Kravtsov, A. V., & Chen, H.-W. (2008). Escape of Ionizing Radiation from High-Redshift Galaxies. ApJ, *672*(2), 765–775. https://doi.org/10.1086/524007

Górski, K. M., Hivon, E., Banday, A. J., Wandelt, B. D., Hansen, F. K., Reinecke, M., & Bartelmann, M. (2005). HEALPix: A Framework for High-Resolution Discretization and Fast Analysis of Data Distributed on the Sphere. ApJ, *622*(2), 759–771. https://doi.org/10.1086/427976

Grazian, A., Giallongo, E., Paris, D., Boutsia, K., Dickinson, M., Santini, P., Windhorst, R. A., Jansen, R. A., Cohen, S. H., Ashcraft, T. A., Scarlata, C., Rutkowski, M. J., Vanzella, E., Cusano, F., Cristiani, S., Giavalisco, M., Ferguson, H. C., Koekemoer, A., Grogin, N. A., ... Yan, H. (2017). Lyman continuum escape fraction of faint galaxies at z $\sim$ 3.3 in the CANDELS/GOODS-North, EGS, and COSMOS fields with LBC. A&A, *602*, Article A18, A18. https://doi.org/10.1051/0004-6361/201730447

Gunn, J. E., & Peterson, B. A. (1965). On the Density of Neutral Hydrogen in Intergalactic Space. ApJ, *142*, 1633–1636. https://doi.org/10.1086/148444

Harikane, Y., Inoue, A. K., Mawatari, K., Hashimoto, T., Yamanaka, S., Fudamoto, Y., Matsuo, H., Tamura, Y., Dayal, P., Yung, L. Y. A., Hutter, A., Pacucci, F., Sugahara, Y., & Koekemoer, A. M. (2022). A Search for H-Dropout Lyman Break Galaxies at z $\sim$ 12-16. ApJ, *929*(1), Article 1, 1. https://doi.org/10.3847/1538-4357/ac53a9

Harikane, Y., Ouchi, M., Inoue, A. K., Matsuoka, Y., Tamura, Y., Bakx, T., Fujimoto, S., Moriwaki, K., Ono, Y., Nagao, T., Tadaki, K.-i., Kojima, T., Shibuya, T., Egami, E., Ferrara, A., Gallerani, S., Hashimoto, T., Kohno, K., Matsuda, Y., ... Vallini, L. (2020). Large Population of ALMA Galaxies at z $>$ 6 with Very High [O III] 88 μm to [C II] 158 μm Flux Ratios: Evidence of Extremely High Ionization Parameter or PDR Deficit? ApJ, *896*(2), Article 93, 93. https://doi.org/10.3847/1538-4357/ab94bd

Harikane, Y., Ouchi, M., Oguri, M., Ono, Y., Nakajima, K., Isobe, Y., Umeda, H., Mawatari, K., & Zhang, Y. (2023). A Comprehensive Study of Galaxies at z $\sim$ 9-16 Found in the Early JWST Data: Ultraviolet Luminosity Functions and Cosmic Star Formation History at the Pre-reionization Epoch. ApJS, *265*(1), Article 5, 5. https://doi.org/10.3847/1538-4365/acaaa9

Haslbauer, M., Kroupa, P., Zonoozi, A. H., & Haghi, H. (2022). Has JWST Already Falsified Dark-matter-driven Galaxy Formation? ApJ, *939*(2), Article L31, L31. https://doi.org/10.3847/2041-8213/ac9a50

Henyey, L. G., & Greenstein, J. L. (1941). Diffuse radiation in the Galaxy. ApJ, *93*, 70–83. https://doi.org/10.1086/144246

Hinshaw, G., Larson, D., Komatsu, E., Spergel, D. N., Bennett, C. L., Dunkley, J., Nolta, M. R., Halpern, M., Hill, R. S., Odegard, N., Page, L., Smith, K. M., Weiland, J. L., Gold, B., Jarosik, N., Kogut, A., Limon, M., Meyer, S. S., Tucker, G. S., ... Wright, E. L. (2013). Nine-year Wilkinson Microwave Anisotropy Probe (WMAP) Observations: Cosmological Parameter Results. ApJS, *208*(2), Article 19, 19. https://doi.org/10.1088/0067-0049/208/2/19

Hutter, A., Dayal, P., Partl, A. M., & Müller, V. (2014). The visibility of Lyman α emitters: constraining reionization, ionizing photon escape fractions and dust. MNRAS, *441*(4), 2861–2877. https://doi.org/10.1093/mnras/stu791

Izotov, Y. I., Worseck, G., Schaerer, D., Guseva, N. G., Chisholm, J., Thuan, T. X., Fricke, K. J., & Verhamme, A. (2021). Lyman continuum leakage from low-mass galaxies with $M_\star < 10^8$ $M_\odot$. MNRAS, *503*(2), 1734–1752. https://doi.org/10.1093/mnras/stab612

Izotov, Y. I., Worseck, G., Schaerer, D., Guseva, N. G., Thuan, T. X., Fricke, A., Verhamme, & Orlitová, I. (2018). Low-redshift Lyman continuum leaking galaxies with high [O III]/[O II] ratios. MNRAS, *478*(4), 4851–4865. https://doi.org/10.1093/mnras/sty1378

Kannan, R., Springel, V., Hernquist, L., Pakmor, R., Delgado, A. M., Hadzhiyska, B., Hernández-Aguayo, C., Barrera, M., Ferlito, F., Bose, S., White, S., Frenk, C., Smith, A., & Garaldi, E. (2022). The MillenniumTNG Project: The galaxy population at $z \geq 8$. *arXiv e-prints*, Article arXiv:2210.10066, arXiv:2210.10066. https://doi.org/10.48550/arXiv.2210.10066

Katz, H., Garel, T., Rosdahl, J., Mauerhofer, V., Kimm, T., Blaizot, J., Michel-Dansac, L., Devriendt, J., Slyz, A., & Haehnelt, M. (2022a). Mg II in the JWST era: a probe of Lyman continuum escape? MNRAS, *515*(3), 4265–4286. https://doi.org/10.1093/mnras/stac1437

Katz, H., Kimm, T., Ellis, R. S., Devriendt, J., & Slyz, A. (2022b). The Challenges of Identifying Population III Stars in the Early Universe. *arXiv e-prints*, Article arXiv:2207.04751, arXiv:2207.04751. https://doi.org/10.48550/arXiv.2207.04751

Katz, H., Liu, S., Kimm, T., Rey, M. P., Andersson, E. P., Cameron, A. J., Rodriguez-Montero, F., Agertz, O., Devriendt, J., & Slyz, A. (2022c). PRISM: A Non-Equilibrium, Multiphase Interstellar Medium Model for Radiation Hydrodynamics Simulations of Galaxies. *arXiv e-prints*, Article arXiv:2211.04626, arXiv:2211.04626. https://doi.org/10.48550/arXiv.2211.04626

Kauffmann, G., & White, S. D. M. (1993). The merging history of dark matter haloes in a hierarchical universe. MNRAS, *261*, 921–928. https://doi.org/10.1093/mnras/261.4.921

Keating, L. C., Weinberger, L. H., Kulkarni, G., Haehnelt, M. G., Chardin, J., & Aubert, D. (2020). Long troughs in the Lyman-α forest below redshift 6 due to islands of neutral hydrogen. MNRAS, *491*(2), 1736–1745. https://doi.org/10.1093/mnras/stz3083

Keller, B. W., Munshi, F., Trebitsch, M., & Tremmel, M. (2023). Can Cosmological Simulations Reproduce the Spectroscopically Confirmed Galaxies Seen at z $\geq$ 10? ApJ, *943*(2), Article L28, L28. https://doi.org/10.3847/2041-8213/acb148

Laursen, P., Sommer-Larsen, J., & Andersen, A. C. (2009). Lyα Radiative Transfer with Dust: Escape Fractions from Simulated High-Redshift Galaxies. ApJ, *704*(2), 1640–1656. https://doi.org/10.1088/0004-637X/704/2/1640

Leśniewska, A., & Michałowski, M. J. (2019). Dust production scenarios in galaxies at z ∼6-8.3. A&A, *624*, Article L13, L13. https://doi.org/10.1051/0004-6361/201935149

Li, A., & Draine, B. T. (2001). Infrared Emission from Interstellar Dust. II. The Diffuse Interstellar Medium. ApJ, *554*(2), 778–802. https://doi.org/10.1086/323147

Liu, B., & Bromm, V. (2020). When did Population III star formation end? MNRAS, *497*(3), 2839–2854. https://doi.org/10.1093/mnras/staa2143

Lotz, J. M., Koekemoer, A., Coe, D., Grogin, N., Capak, P., Mack, J., Anderson, J., Avila, R., Barker, E. A., Borncamp, D., Brammer, G., Durbin, M., Gunning, H., Hilbert, B., Jenkner, H., Khandrika, H., Levay, Z., Lucas, R. A., MacKenty, J., ... Mountain, M. (2017). The Frontier Fields: Survey Design and Initial Results. ApJ, *837*(1), Article 97, 97. https://doi.org/10.3847/1538-4357/837/1/97

Ma, X., Quataert, E., Wetzel, A., Hopkins, P. F., Faucher-Giguère, C.-A., & Kereš, D. (2020). No missing photons for reionization: moderate ionizing photon escape fractions from the FIRE-2 simulations. MNRAS, *498*(2), 2001–2017. https://doi.org/10.1093/mnras/staa2404

Madau, P., & Haardt, F. (2015). Cosmic Reionization after Planck: Could Quasars Do It All? ApJ, *813*(1), Article L8, L8. https://doi.org/10.1088/2041-8205/813/1/L8

Maiolino, R., Uebler, H., Perna, M., Scholtz, J., D'Eugenio, F., Witten, C., Laporte, N., Witstok, J., Carniani, S., Tacchella, S., Baker, W., Arribas, S., Nakajima, K., Eisenstein, D., Bunker, A., Charlot, S., Cresci, G., Curti, M., Curtis-Lake, E., ... Willmer, C. (2023). JWST-JADES. Possible Population III signatures at z=10.6 in the halo of GN-z11. *arXiv e-prints*, Article arXiv:2306.00953, arXiv:2306.00953. https://doi.org/10.48550/arXiv.2306.00953

Marassi, S., Schneider, R., Limongi, M., Chieffi, A., Graziani, L., & Bianchi, S. (2019). Supernova dust yields: the role of metallicity, rotation, and fallback. MNRAS, *484*(2), 2587–2604. https://doi.org/10.1093/mnras/sty3323

Marinacci, F., Vogelsberger, M., Pakmor, R., Torrey, P., Springel, V., Hernquist, L., Nelson, D., Weinberger, R., Pillepich, A., Naiman, J., & Genel, S. (2018). First results from the IllustrisTNG simulations: radio haloes and magnetic fields. MNRAS, *480*(4), 5113–5139. https://doi.org/10.1093/mnras/sty2206

Markov, V., Gallerani, S., Pallottini, A., Sommovigo, L., Carniani, S., Ferrara, A., Parlanti, E., & Di Mascia, F. (2023). Dust attenuation law in JWST galaxies at z = 7-8. *arXiv e-prints*, Article arXiv:2304.11178, arXiv:2304.11178. https://doi.org/10.48550/arXiv.2304.11178

Mauerhofer, V., Verhamme, A., Blaizot, J., Garel, T., Kimm, T., Michel-Dansac, L., & Rosdahl, J. (2021). UV absorption lines and their potential for tracing the Lyman continuum escape fraction. A&A, *646*, Article A80, A80. https://doi.org/10.1051/0004-6361/202039449

Mauerhofer, V. (2021). *Metallic uv absorption lines as diagnostics of the escape of ionising photons from simulated galaxies* (Doctoral dissertation). Université de Lyon; Université de Genève.

Mauerhofer, V., & Dayal, P. (2023). The dust enrichment and detectability of early galaxies in the JWST and ALMA era. *arXiv e-prints*, Article arXiv:2305.01681, arXiv:2305.01681. https://doi.org/10.48550/arXiv.2305.01681

McCaffrey, J., Hardin, S., Wise, J., & Regan, J. (2023). No Tension: JWST Galaxies at $z > 10$ Consistent with Cosmological Simulations. *arXiv e-prints*, Article arXiv:2304.13755, arXiv:2304.13755. https://doi.org/10.48550/arXiv.2304.13755

McKee, C. (1989). Dust Destruction in the Interstellar Medium. In L. J. Allamandola & A. G. G. M. Tielens (Eds.), *Interstellar dust* (p. 431).

Meiksin, A., & Madau, P. (1993). On the Photoionization of the Intergalactic Medium by Quasars at High Redshift. ApJ, *412*, 34. https://doi.org/10.1086/172898

Meurer, G. R., Heckman, T. M., & Calzetti, D. (1999). Dust Absorption and the Ultraviolet Luminosity Density at z ~3 as Calibrated by Local Starburst Galaxies. ApJ, *521*(1), 64–80. https://doi.org/10.1086/307523

Michałowski, M. J. (2015). Dust production 680-850 million years after the Big Bang. A&A, *577*, Article A80, A80. https://doi.org/10.1051/0004-6361/201525644

Michel-Dansac, L., Blaizot, J., Garel, T., Verhamme, A., Kimm, T., & Trebitsch, M. (2020). RASCAS: RAdiation SCattering in Astrophysical Simulations. A&A, *635*, Article A154, A154. https://doi.org/10.1051/0004-6361/201834961

Naidu, R. P., Oesch, P. A., Setton, D. J., Matthee, J., Conroy, C., Johnson, B. D., Weaver, J. R., Bouwens, R. J., Brammer, G. B., Dayal, P., Illingworth, G. D., Barrufet, L., Belli, S., Bezanson, R., Bose, S., Heintz, K. E., Leja, J., Leonova, E., Marques-Chaves, R., ... Whitaker, K. E. (2022a). Schrodinger's Galaxy Candidate: Puzzlingly Luminous at $z \approx 17$, or Dusty/Quenched at $z \approx 5$? *arXiv e-prints*, Article arXiv:2208.02794, arXiv:2208.02794. https://doi.org/10.48550/arXiv.2208.02794

Naidu, R. P., Oesch, P. A., van Dokkum, P., Nelson, E. J., Suess, K. A., Brammer, G., Whitaker, K. E., Illingworth, G., Bouwens, R., Tacchella, S., Matthee, J., Allen, N., Bezanson, R., Conroy, C., Labbe, I., Leja, J., Leonova, E., Magee, D., Price, S. H., ... Weibel, A. (2022b). Two Remarkably Luminous Galaxy Candidates at z ≈ 10-12 Revealed by JWST. ApJ, *940*(1), Article L14, L14. https://doi.org/10.3847/2041-8213/ac9b22

Oesch, P. A., Brammer, G., van Dokkum, P. G., Illingworth, G. D., Bouwens, R. J., Labbé, I., Franx, M., Momcheva, I., Ashby, M. L. N., Fazio, G. G., Gonzalez, V., Holden, B., Magee, D., Skelton, R. E., Smit, R., Spitler, L. R., Trenti, M., & Willner, S. P. (2016). A Remarkably Luminous Galaxy at z=11.1 Measured with Hubble Space Telescope Grism Spectroscopy. ApJ, *819*(2), Article 129, 129. https://doi.org/10.3847/0004-637X/819/2/129

Ono, Y., Ouchi, M., Harikane, Y., Toshikawa, J., Rauch, M., Yuma, S., Sawicki, M., Shibuya, T., Shimasaku, K., Oguri, M., Willott, C., Akhlaghi, M., Akiyama, M., Coupon, J., Kashikawa, N., Komiyama, Y., Konno, A., Lin, L., Matsuoka, Y., ... Wang, S.-Y. (2018). Great Optically Luminous Dropout Research Using Subaru HSC (GOLDRUSH). I. UV luminosity functions at z ∼ 4-7 derived with

the half-million dropouts on the 100 deg^2 sky. PASJ, *70*, Article S10, S10. https://doi.org/10.1093/pasj/psx103

Osterbrock, D. E., & Ferland, G. J. (2006). *Astrophysics of gaseous nebulae and active galactic nuclei*.

Overzier, R. A., Heckman, T. M., Wang, J., Armus, L., Buat, V., Howell, J., Meurer, G., Seibert, M., Siana, B., Basu-Zych, A., Charlot, S., Gonçalves, T. S., Martin, D. C., Neill, J. D., Rich, R. M., Salim, S., & Schiminovich, D. (2011). Dust Attenuation in UV-selected Starbursts at High Redshift and Their Local Counterparts: Implications for the Cosmic Star Formation Rate Density. ApJ, *726*(1), Article L7, L7. https://doi.org/10.1088/2041-8205/726/1/L7

Pacucci, F., Dayal, P., Harikane, Y., Inoue, A. K., & Loeb, A. (2022). Are the newly-discovered z 13 drop-out sources starburst galaxies or quasars? MNRAS, *514*(1), L6–L10. https://doi.org/10.1093/mnrasl/slac035

Pei, Y. C. (1992). Interstellar Dust from the Milky Way to the Magellanic Clouds. ApJ, *395*, 130. https://doi.org/10.1086/171637

Perivolaropoulos, L., & Skara, F. (2022). Challenges for ΛCDM: An update. New A Rev., *95*, Article 101659, 101659. https://doi.org/10.1016/j.newar.2022.101659

Planck Collaboration, Aghanim, N., Akrami, Y., Ashdown, M., Aumont, J., Baccigalupi, C., Ballardini, M., Banday, A. J., Barreiro, R. B., Bartolo, N., Basak, S., Battye, R., Benabed, K., Bernard, J. .-., Bersanelli, M., Bielewicz, P., Bock, J. J., Bond, J. R., Borrill, J., ... Zonca, A. (2020a). Planck 2018 results. VI. Cosmological parameters. A&A, *641*, Article A6, A6. https://doi.org/10.1051/0004-6361/201833910

Planck Collaboration, Aghanim, N., Akrami, Y., Ashdown, M., Aumont, J., Baccigalupi, C., Ballardini, M., Banday, A. J., Barreiro, R. B., Bartolo, N., Basak, S., Benabed, K., Bernard, J. .-., Bersanelli, M., Bielewicz, P., Bock, J. J., Bond, J. R., Borrill, J., Bouchet, F. R., ... Zonca, A. (2020b). Planck 2018 results. V. CMB power spectra and likelihoods. A&A, *641*, Article A5, A5. https://doi.org/10.1051/0004-6361/201936386

Popping, G., Somerville, R. S., & Galametz, M. (2017). The dust content of galaxies from z = 0 to z = 9. MNRAS, *471*(3), 3152–3185. https://doi.org/10.1093/mnras/stx1545

Postman, M., Coe, D., Benítez, N., Bradley, L., Broadhurst, T., Donahue, M., Ford, H., Graur, O., Graves, G., Jouvel, S., Koekemoer, A., Lemze, D., Medezinski, E., Molino, A., Moustakas, L., Ogaz, S., Riess, A., Rodney, S., Rosati, P., ... Van der Wel, A. (2012). The Cluster Lensing and Supernova Survey with Hubble: An Overview. ApJS, *199*(2), Article 25, 25. https://doi.org/10.1088/0067-0049/199/2/25

Prole, L. R., Schauer, A. T. P., Clark, P. C., Glover, S. C. O., Priestley, F. D., & Klessen, R. S. (2023). From dark matter halos to pre-stellar cores: high resolution follow-up of cosmological Lyman-Werner simulations. MNRAS, *520*(2), 2081–2093. https://doi.org/10.1093/mnras/stad188

Reddy, N. A., Oesch, P. A., Bouwens, R. J., Montes, M., Illingworth, G. D., Steidel, C. C., van Dokkum, P. G., Atek, H., Carollo, M. C., Cibinel, A., Holden, B., Labbé, I., Magee, D., Morselli, L., Nelson, E. J., & Wilkins, S. (2018). The HDUV Survey: A Revised Assessment of the Relationship between UV Slope and Dust Attenuation for High-redshift Galaxies. ApJ, *853*(1), Article 56, 56. https://doi.org/10.3847/1538-4357/aaa3e7

Reddy, N. A., Steidel, C. C., Pettini, M., Bogosavljević, M., & Shapley, A. E. (2016). The Connection Between Reddening, Gas Covering Fraction, and the Escape of Ionizing Radiation at High Redshift. ApJ, *828*(2), Article 108, 108. https://doi.org/10.3847/0004-637X/828/2/108

Reddy, N. A., Topping, M. W., Shapley, A. E., Steidel, C. C., Sanders, R. L., Du, X., Coil, A. L., Mobasher, B., Price, S. H., & Shivaei, I. (2022). The Effects of Stellar Population and Gas Covering Fraction on the Emergent Lyα Emission of High-redshift Galaxies. ApJ, *926*(1), Article 31, 31. https://doi.org/10.3847/1538-4357/ac3b4c

Rémy-Ruyer, A., Madden, S. C., Galliano, F., Galametz, M., Takeuchi, T. T., Asano, R. S., Zhukovska, S., Lebouteiller, V., Cormier, D., Jones, A., Bocchio, M., Baes, M., Bendo, G. J., Boquien, M., Boselli, A., DeLooze, I., Doublier-Pritchard, V., Hughes, T., Karczewski, O. Ł., & Spinoglio, L. (2014). Gas-to-dust mass ratios in local galaxies over a 2 dex metallicity range. A&A, *563*, Article A31, A31. https://doi.org/10.1051/0004-6361/201322803

Reuter, C., Vieira, J. D., Spilker, J. S., Weiss, A., Aravena, M., Archipley, M., Béthermin, M., Chapman, S. C., De Breuck, C., Dong, C., Everett, W. B., Fu, J., Greve, T. R., Hayward, C. C., Hill, R., Hezaveh, Y., Jarugula, S., Litke, K., Malkan, M., ... Strandet, M. L. (2020). The Complete Redshift Distribution of Dusty Star-forming Galaxies from the SPT-SZ Survey. ApJ, *902*(1), Article 78, 78. https://doi.org/10.3847/1538-4357/abb599

Rosdahl, J., Blaizot, J., Aubert, D., Stranex, T., & Teyssier, R. (2013). RAMSES-RT: radiation hydrodynamics in the cosmological context. MNRAS, *436*(3), 2188–2231. https://doi.org/10.1093/mnras/stt1722

Rosdahl, J., & Teyssier, R. (2015). A scheme for radiation pressure and photon diffusion with the M1 closure in RAMSES-RT. MNRAS, *449*(4), 4380–4403. https://doi.org/10.1093/mnras/stv567

Rosdahl, J., Blaizot, J., Katz, H., Kimm, T., Garel, T., Haehnelt, M., Keating, L. C., Martin-Alvarez, S., Michel-Dansac, L., & Ocvirk, P. (2022). LyC escape from SPHINX galaxies in the Epoch of Reionization. MNRAS, *515*(2), 2386–2414. https://doi.org/10.1093/mnras/stac1942

Rutkowski, M. J., Scarlata, C., Henry, A., Hayes, M., Mehta, V., Hathi, N., Cohen, S., Windhorst, R., Koekemoer, A. M., Teplitz, H. I., Haardt, F., & Siana, B. (2017). The Lyman Continuum Escape Fraction of Emission Line-selected z $\sim$ 2.5 Galaxies Is Less Than 15%. ApJ, *841*(2), Article L27, L27. https://doi.org/10.3847/2041-8213/aa733b

Salucci, P. (2001). The constant-density region of the dark haloes of spiral galaxies. MNRAS, *320*(1), L1–L5. https://doi.org/10.1046/j.1365-8711.2001.04076.x

Schaerer, D., Ginolfi, M., Béthermin, M., Fudamoto, Y., Oesch, P. A., Le Fèvre, O., Faisst, A., Capak, P., Cassata, P., Silverman, J. D., Yan, L., Jones, G. C., Amorin, R., Bardelli, S., Boquien, M., Cimatti, A., Dessauges-Zavadsky, M., Giavalisco, M., Hathi, N. P., … Zucca, E. (2020). The ALPINE-ALMA [C II] survey. Little to no evolution in the [C II]-SFR relation over the last 13 Gyr. A&A, *643*, Article A3, A3. https://doi.org/10.1051/0004-6361/202037617

Schechter, P. (1976). An analytic expression for the luminosity function for galaxies. ApJ, *203*, 297–306. https://doi.org/10.1086/154079

Schenker, M. A., Ellis, R. S., Konidaris, N. P., & Stark, D. P. (2014). Line-emitting Galaxies beyond a Redshift of 7: An Improved Method for Estimating the Evolving Neutrality of the Intergalactic Medium. ApJ, *795*(1), Article 20, 20. https://doi.org/10.1088/0004-637X/795/1/20

Shapiro, P. R., & Giroux, M. L. (1987). Cosmological H II Regions and the Photoionization of the Intergalactic Medium. ApJ, *321*, L107. https://doi.org/10.1086/185015

Shapley, A. E., Sanders, R. L., Reddy, N. A., Topping, M. W., & Brammer, G. B. (2023). JWST/NIRSpec Balmer-line Measurements of Star Formation and Dust Attenuation at z˜3-6. *arXiv e-prints*, Article arXiv:2301.03241, arXiv:2301.03241. https://doi.org/10.48550/arXiv.2301.03241

Shen, X., Vogelsberger, M., Nelson, D., Pillepich, A., Tacchella, S., Marinacci, F., Torrey, P., Hernquist, L., & Springel, V. (2020). High-redshift JWST predictions from IllustrisTNG: II. Galaxy line and continuum spectral indices and dust attenuation curves. MNRAS, *495*(4), 4747–4768. https://doi.org/10.1093/mnras/staa1423

Singh, S., Jishnu, N. T., Subrahmanyan, R., Udaya Shankar, N., Girish, B. S., Raghunathan, A., Somashekar, R., Srivani, K. S., & Sathyanarayana Rao, M. (2022). On the detection of a cosmic dawn signal in the radio background. *Nature Astronomy*, *6*, 607–617. https://doi.org/10.1038/s41550-022-01610-5

Sommovigo, L., Ferrara, A., Pallottini, A., Carniani, S., Gallerani, S., & Decataldo, D. (2020). Warm dust in high-z galaxies: origin and implications. MNRAS, *497*(1), 956–968. https://doi.org/10.1093/mnras/staa1959

Sommovigo, L., Ferrara, A., Pallottini, A., Dayal, P., Bouwens, R. J., Smit, R., da Cunha, E., De Looze, I., Bowler, R. A. A., Hodge, J., Inami, H., Oesch, P., Endsley, R., Gonzalez, V., Schouws, S., Stark, D., Stefanon, M., Aravena, M., Graziani, L., … Topping, M. (2022). The ALMA REBELS Survey: cosmic dust temperature evolution out to z $\sim$ 7. MNRAS, *513*(3), 3122–3135. https://doi.org/10.1093/mnras/stac302

Stacy, A., Bromm, V., & Lee, A. T. (2016). Building up the Population III initial mass function from cosmological initial conditions. MNRAS, *462*(2), 1307–1328. https://doi.org/10.1093/mnras/stw1728

Stanway, E. R., & Eldridge, J. J. (2018). Re-evaluating old stellar populations. MNRAS, *479*(1), 75–93. https://doi.org/10.1093/mnras/sty1353

Stark, D. P., Ellis, R. S., Chiu, K., Ouchi, M., & Bunker, A. (2010). Keck spectroscopy of faint $3 < z < 7$ Lyman break galaxies - I. New constraints on cosmic reionization from the luminosity and redshift-dependent fraction of Lyman α emission. MNRAS, *408*(3), 1628–1648. https://doi.org/10.1111/j.1365-2966.2010.17227.x

Steidel, C. C., Bogosavljević, M., Shapley, A. E., Reddy, N. A., Rudie, G. C., Pettini, M., Trainor, R. F., & Strom, A. L. (2018). The Keck Lyman Continuum Spectroscopic Survey (KLCS): The Emergent Ionizing Spectrum of Galaxies at $z \sim 3$. ApJ, *869*(2), Article 123, 123. https://doi.org/10.3847/1538-4357/aaed28

Steidel, C. C., Pettini, M., & Adelberger, K. L. (2001). Lyman-Continuum Emission from Galaxies at Z ~= 3.4. ApJ, *546*(2), 665–671. https://doi.org/10.1086/318323

Strömgren, B. (1939). The Physical State of Interstellar Hydrogen. ApJ, *89*, 526. https://doi.org/10.1086/144074

Taylor, J. E. (2011). Dark Matter Halos from the Inside Out. *Advances in Astronomy*, *2011*, Article 604898, 604898. https://doi.org/10.1155/2011/604898

Teyssier, R. (2002). Cosmological hydrodynamics with adaptive mesh refinement. A new high resolution code called RAMSES. A&A, *385*, 337–364. https://doi.org/10.1051/0004-6361:20011817

Trayford, J. W., Camps, P., Theuns, T., Baes, M., Bower, R. G., Crain, R. A., Gunawardhana, M. L. P., Schaller, M., Schaye, J., & Frenk, C. S. (2017). Optical colours and spectral indices of $z = 0.1$ eagle galaxies with the 3D dust radiative transfer code skirt. MNRAS, *470*(1), 771–799. https://doi.org/10.1093/mnras/stx1051

Trebitsch, M., Dubois, Y., Volonteri, M., Pfister, H., Cadiou, C., Katz, H., Rosdahl, J., Kimm, T., Pichon, C., Beckmann, R. S., Devriendt, J., & Slyz, A. (2021). The OBELISK simulation: Galaxies contribute more than AGN to H I reionization of protoclusters. A&A, *653*, Article A154, A154. https://doi.org/10.1051/0004-6361/202037698

Triani, D. P., Sinha, M., Croton, D. J., Pacifici, C., & Dwek, E. (2020). The origin of dust in galaxies across cosmic time. MNRAS, *493*(2), 2490–2505. https://doi.org/10.1093/mnras/staa446

Trussler, J. A. A., Conselice, C. J., Adams, N. J., Maiolino, R., Nakajima, K., Zackrisson, E., & Ferreira, L. (2022). On the observability and identification of Population III galaxies with JWST. *arXiv e-prints*, Article arXiv:2211.02038, arXiv:2211.02038. https://doi.org/10.48550/arXiv.2211.02038

Turk, M. J., Smith, B. D., Oishi, J. S., Skory, S., Skillman, S. W., Abel, T., & Norman, M. L. (2011). yt: A Multi-code Analysis Toolkit for Astrophysical Simulation Data. ApJS, *192*(1), Article 9, 9. https://doi.org/10.1088/0067-0049/192/1/9

Verner, D. A., Ferland, G. J., Korista, K. T., & Yakovlev, D. G. (1996). Atomic Data for Astrophysics. II. New Analytic FITS for Photoionization Cross Sections of Atoms and Ions. ApJ, *465*, 487. https://doi.org/10.1086/177435

Weingartner, J. C., & Draine, B. T. (2001). Dust Grain-Size Distributions and Extinction in the Milky Way, Large Magellanic Cloud, and Small Magellanic Cloud. ApJ, *548*(1), 296–309. https://doi.org/10.1086/318651

Wise, J. H. (2019). An Introductory Review on Cosmic Reionization. *arXiv e-prints*, Article arXiv:1907.06653, arXiv:1907.06653. https://doi.org/10.48550/arXiv.1907.06653

Witstok, J., Jones, G. C., Maiolino, R., Smit, R., & Schneider, R. (2023a). An empirical study of dust properties at the earliest epochs. MNRAS. https://doi.org/10.1093/mnras/stad1470

Witstok, J., Shivaei, I., Smit, R., Maiolino, R., Carniani, S., Curtis-Lake, E., Ferruit, P., Arribas, S., Bunker, A. J., Cameron, A. J., Charlot, S., Chevallard, J., Curti, M., de Graaff, A., D'Eugenio, F., Giardino, G., Looser, T. J., Rawle, T., Rodríguez del Pino, B., ... Willmer, C. N. A. (2023b). Carbonaceous dust grains within galaxies seen in the first billion years of cosmic time. *arXiv e-prints*, Article arXiv:2302.05468, arXiv:2302.05468. https://doi.org/10.48550/arXiv.2302.05468

Xi, H., Staveley-Smith, L., For, B.-Q., Freudling, W., Zwaan, M., Hoppmann, L., Liang, F.-H., & Peng, B. (2021). The Arecibo Ultra-Deep Survey. MNRAS, *501*(3), 4550–4564. https://doi.org/10.1093/mnras/staa3931

Yeh, J. Y. .-., Smith, A., Kannan, R., Garaldi, E., Vogelsberger, M., Borrow, J., Pakmor, R., Springel, V., & Hernquist, L. (2023). The THESAN project: ionizing escape fractions of reionization-era galaxies. MNRAS, *520*(2), 2757–2780. https://doi.org/10.1093/mnras/stad210

Zubko, V., Dwek, E., & Arendt, R. G. (2004). Interstellar Dust Models Consistent with Extinction, Emission, and Abundance Constraints. ApJS, *152*(2), 211–249. https://doi.org/10.1086/382351